Interlaminar Mode III Fracture ECT Method – Testing and Analysis

by

Grant Browning

A Thesis Submitted to the Faculty of

the College of Engineering and Computer Science

in Partial Fulfillment of the Requirements for the Degree of

Master of Science

Florida Atlantic University

Boca Raton, Florida

May 2009

Interlaminar Mode III Fracture ECT Method – Testing and Analysis

By

Grant Browning

This thesis was prepared under the direction of the candidate's thesis advisor, Dr. Leif A. Carlsson, Department of Mechanical Engineering, and has been approved by the members of his supervisory committee. It was submitted to the faculty of the College of Engineering and Computer Science and was accepted in partial fulfillment of the requirements for the degree of Master of Science.

SUPERVISORY COMMITTEE:

Leif A. Carlsson, Ph.D.
Thesis Advisor

Oren Masory, Ph.D.

Gary Salivar, Ph.D.

Oren Masory, Ph.D.
Chair, Department of Mechanical Engineering

Karl K. Stevens, Ph.D., P.E.
Dean, College of Engineering and Computer Science

Barry T. Rosson, Ph.D.
Dean, Graduate College

April 28, 2009
Date

Acknowledgements

First and foremost the author would like to extend his gratitude to Dr. Leif Carlsson, the director and premiere advisor to the research and development of this study. His constant, experienced, wise, and knowledgeable mentoring through constructive criticism, advice, and by example has kept me honest and continues to force my growth as an engineer and a person.

This research is part of a program that was partially funded by Bell Helicopter Textron and the Center for Rotorcraft Innovation (CRI), and partially funded by the National Rotorcraft Technology Center (NRTC), U.S. Army Aviation and Missile Research, Development and Engineering Center (AMRDEC) under Technology Investment Agreement W911W6-06-2-0002, entitled National Rotorcraft Technology Center Research Program. The author of the thesis would like to acknowledge that this research and development was accomplished with the support and guidance of the NRTC and CRI/Bell Helicopter through Dr. Xiaoming Li as the program lead.

The critical technical support from James Ratcliffe in the field of Mode III and Christian Berggreen in FEA modeling were significant.

I would also sincerely like to thank my parents, Robert and Grace, for their understanding and unwavering belief in me to overcome life's struggles and my Grandfathers George Blome and Robert Browning who inspired me to go into the mechanical engineering field.

Abstract

Author:	Grant Browning
Title:	Interlaminar Fracture Mode III ECT Method – Testing and Analysis
Institution:	Florida Atlantic University
Thesis Advisor:	Dr. Leif A. Carlsson
Degree:	Master of Science
Year:	2009

In an effort to obtain an improved mode III fracture toughness test suitable for a testing standard, mechanics analysis, experimental testing, and finite element analysis (FEA) have been conducted. Of particular concern are the merits of one-point and two-point edge crack torsion (ECT) test methods, the influence of specimen geometry that overhangs beyond load/support points, and the influence of crack length on the compliance and energy release rate. Shear stress distributions at the crack front are determined to examine the uniformity of mode III loading and mode II influence. The shear stress distributions in the one-point and two-point tests are virtually identical, indicating that either of the two tests could be used interchangeably. Based on the uniformity of the mode III shear stress distribution along the crack front, it was found that the ECT specimen should have minimum overhang. Longer crack lengths tend to

produce nonuniform shear stress distributions. A modified two-point ECT test fixture was developed to allow testing of specimens with a range of dimensions. This development enabled experimental verification of the results from the FEA overhang series. The specimens with a minimum overhang produced consistant mode III toughness data. The most reliable way to reduce data is through the original compliance calibration method. A modified ECT specimen was developed with a staggered crack front to produce uniform mode III crack growth. Finite element analysis of the modified ECT specimen shows a uniform mode III stress distribution along the crack front with little mode II interaction.

Table of Contents

List of Figures

List of Tables

1 Introduction

1.1 History of Composites

Conventional structural materials can be split into the three broad groups of metals, ceramics, and polymers. Composites are produced by combining materials from one or more of these categories. Though composites are thought of as being a new idea, with the large scale implementation of composites such as carbon fiber on the forefront of technology, composites have been utilized over several centuries. Composites are also widely found in nature. For example, wood, which remains a widely used structural material today, is a naturally occurring composite. Man-made composites date back to straw-reinforced clay bricks used by the Egyptians noted in biblical references. Achilles's shield as described in the *Illiad* is an example of a composite laminate. In the 19th century iron rods were used as reinforcement for masonry, which led to what is still used extensively today, steel-reinforced concrete. The first fiberglass boat was fabricated in 1942. Filament winding was developed in 1946 followed by composite applications for missiles in the 1950's. The first boron and carbon fibers were introduced in the early 1960's. Metal matrix composites surfaced in 1970 and the development of Kevlar in 1973. Composites are now well established in high performance applications such as aerospace and motorsports because of their weight savings and stiffness. Current high end racing cars use carbon fiber composite materials not only in the chassis but also for such components as brake rotors, springs, and body work. Many military applications

use composites not only for light weight but also to utilize stealth technology first seen in the Lockheed Martin stealth fighter (1).

1.2 Characteristics of Composites

A structural composite is a material system consisting of two or more phases on a macroscopic scale. Most composites are composed of one type of fiber and a matrix. The fiber is significantly stronger and stiffer than the matrix. This fiber is often referred to as the reinforcement. The purpose of a composite is to produce a material that is superior to either of the phases independently. The superiority of composites does not only come through strength but there are other advantages such as lighter weight. In fact in most cases the strength of a composite falls below that of structural metals. A unidirectional fiber reinforced composite will have highly directional material properties. That is to say the direction of the fibers will be much stronger and stiffer than perpendicular to the fibers. This form of material typically uses a thermoplastic or thermoset matrix material and is produced in sheets of fibers similar in appearance to a sheet of fabric. In addition to unidirectional composites, woven composites are quite common where half of the fibers are oriented along the 0° axis and half along the 90° axis. These layers are stacked producing thickness in the composite. This stacking allows each layer to have its own direction or orientation. The set of ply orientations in the stack is called the lay-up. Lay-ups can be chosen to produce composites with unique directional strength characteristics. To achieve more balanced properties, unidirectional plies are stacked into certain lay-up patterns utilizing directions such as 0°, 90°, and ±45°.

1.3 Failure Modes

When a composite is loaded in longitudinal tension, the fiber is commonly the first to fail and therefore decides the failure of the composite, see Figure 1.1.

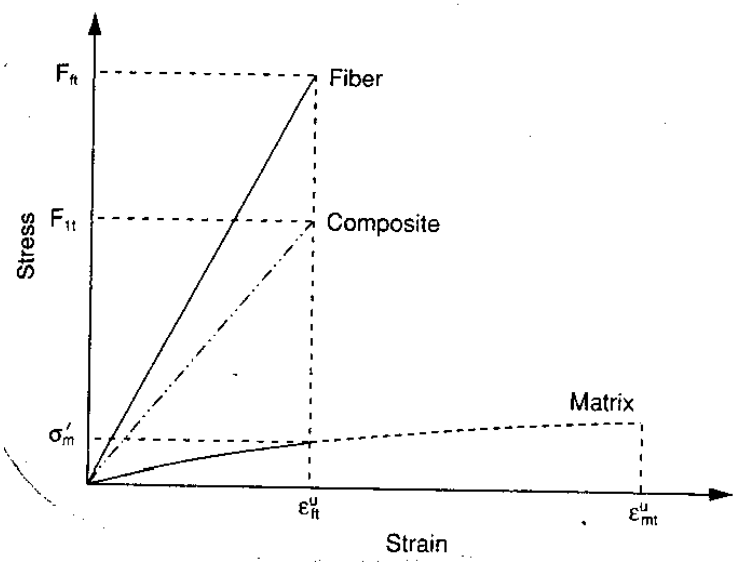

Figure 1.1: Longitudinal stress-strain curves for composite and constituents for the case of fiber-dominated strength (1).

If all the fibers fail at the same strain, the matrix is unable to carry the load and the composite fails. Actual specimens, however, contain fibers of a variety of strengths. Isolated fiber breaks occur at the weak points in the fibers and concentrated stresses develop around the fiber break. Fiber/matrix interface shear stresses will help to transfer stress into the broken fiber ligaments and around the break through the matrix. In most cases the individual fiber breakage is localized and arrested by the surrounding fibers. Loading initially causes single fiber breaks and with increased load, the number of single breaks increases. If several breaks occur in a small volume, the stress concentrations start to interact with each other and cause adjacent fiber breaks leading to total failure. This

failure sequence is depicted in Figure 1.2, where the white spots indicate isolated fiber failures.

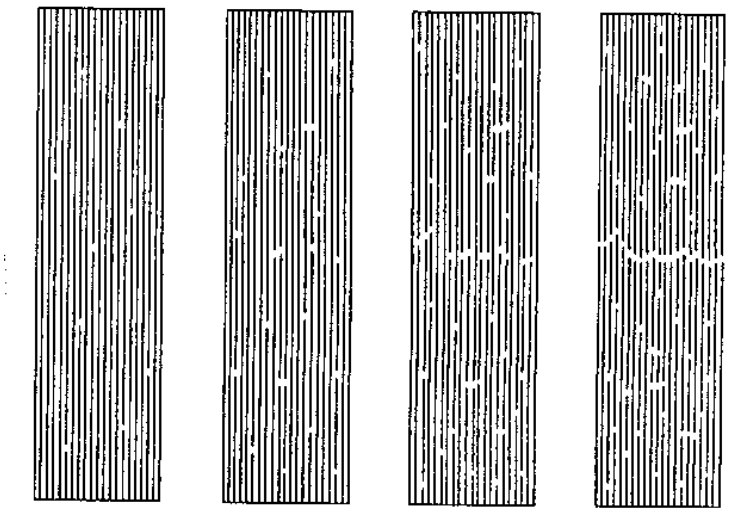

Figure 1.2: Failure sequence in a unidirectional composite with fiber-dominated strength under longitudinal tensile loading (1).

Fiber reinforced composites are sensitive to the direction of loading because of their highly anisotropic properties. Reinforcing this anisotropy is the fact that a specimen may be weaker normal to the fibers than a solid matrix specimen. This is due to the stress concentrations and low interface adhesion between fiber and the matrix. The interface bond between the fiber and matrix is commonly weaker than the solid matrix material.

Composites loaded in compression are susceptible to a failure mode called micro buckling. This failure refers to a short wavelength buckling of individual fibers or groups of fibers inside the composite, ultimately leading to localization of the failure process and failure of the fibers in a kink zone, Figure 1.3.

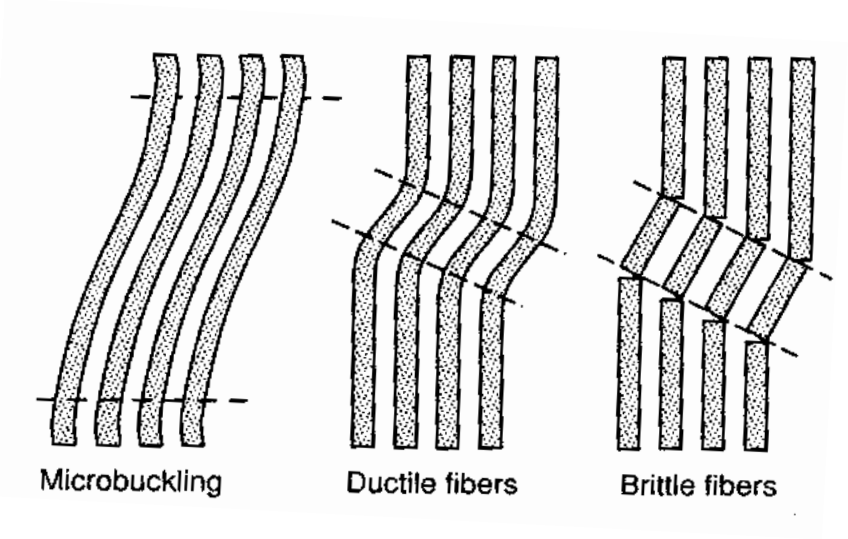

Figure 1.3: Microbuckling leading to formation of kink zones with excessive deformation or fracture planes for ductile or brittle fibers, respectively (1).

Laminated composites are also sensitive to shear loading since load must be transferred through the matrix material and fiber/matrix interface. In-plane or out-of-plane shear loading of the composite may lead to a matrix failure or fiber/matrix interface failure.

Another failure mode, unique to laminated composites, comes in the form of interlaminar delamination, where interlaminar stresses cause the lamina to separate from each other, see Figure 1.4.

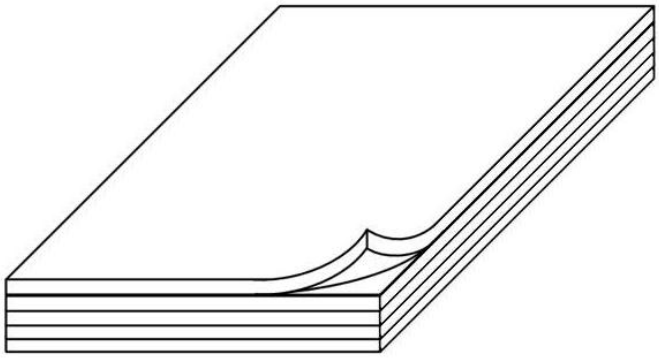

Figure 1.4: Delamination in a composite lay-up.

Interlaminar separation or delamination is a fracture between the fiber layers of a composite laminate. This failure occurs in the thin resin layers between the fiber-reinforced plies of a composite laminate and has long been recognized as being a major life-limiting failure mode. The layers are bonded to each other only by the matrix which provides a low energy fracture path (2). Delamination is caused by interlaminar stresses. Figure 1.5 illustrates some common sources of delamination.

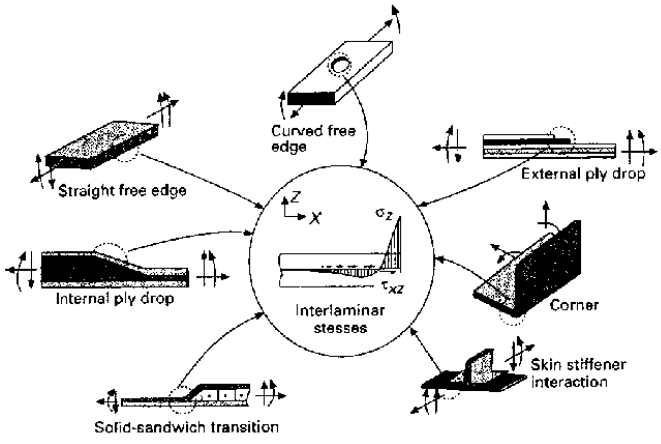

Figure 1.5: Sources of delaminations at geometric and material discontinuities (3).

It should be pointed out that several concepts to reduce the tendency for delamination have been proposed, such as through thickness reinforcement by secondary fibers or z-pins (4), which are pins through the thickness of the composite, but such reinforcements will reduce the in-plane properties of the composite, and are difficult to implement.

1.4 Fracture Mechanics

Delaminations in composite laminates are commonly represented as sharp discontinuities and analyzed using fracture mechanics concepts. Fracture mechanics is an analysis method for cracked or flawed specimens. Fracture mechanics has become an invaluable tool that may be directly applied to practical design. This approach quantifies a driving force for crack propagation that may be compared to the ability of a material to resist crack growth, called fracture toughness to determine whether or not the crack will propagate. Commonly the driving force of crack growth is characterized with a single term called stress intensity factor based on the load applied and geometry alone. A complete characterization of delamination fracture of laminated composites requires consideration of all three fracture modes, i.e., modes I, II, and III illustrated in Figure 1.6. Mode I loading refers to opening of the crack surfaces, while mode II loading consists of sliding displacements of the crack surfaces perpendicular to the crack front. Mode III loading refers to sliding deformations of the crack surfaces parallel to the crack front.

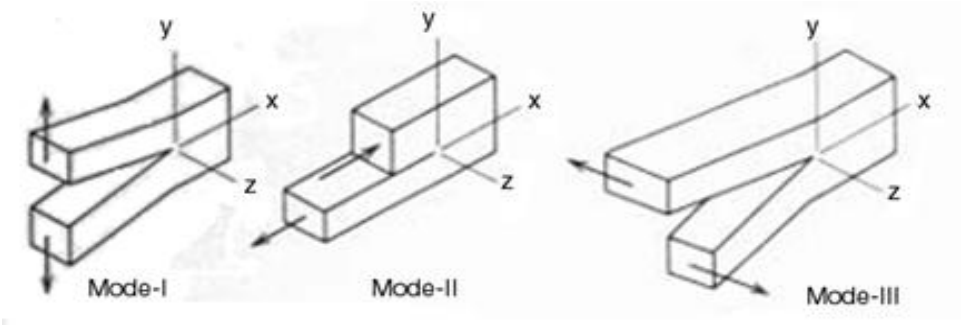

Figure 1.6: Illustration of the three basic modes of crack loading.

For a mode I crack, the intensity of the singular stress field at the crack tip is measured by the stress intensity factor, K_I. The fracture toughness, K_{IC}, is the critical value of K_I, which is calculated at a critical load required to fracture the specimen. Fracture toughness, K_{IC}, is then equal to the driving force, K_I, at the instant of unstable crack extension.

Another approach to characterize crack growth is to use an energy approach based on the strain energy release rate, G. G quantifies the amount of strain energy available to grow a crack per unit area of crack growth. G is given by

$$G = \frac{d}{dA}(W - U) \tag{1.1}$$

where A is the crack area, $U=P\delta/2$ is the stored elastic strain energy, where P is load and δ displacement, $W = \int P d\delta$ is the work done by external forces. For a specimen of uniform width, b, the area, $A=ab$, where a is the crack length, G can be represented by

$$G = \frac{1}{b}\left(P\frac{d\delta}{da} - \frac{dU}{da}\right) = \frac{1}{b}\left(P\frac{d\delta}{da} - \frac{1}{2}\frac{dP\delta}{da}\right) \tag{1.2}$$

To achieve a relation between an experimentally accessible parameter and G, the compliance, $C=\delta/P$, (inverse of stiffness) is introduced to Eq. (1.3)

$$G = \frac{1}{b}\left(P\frac{dCP}{da} - \frac{dCP^2}{da}\right) = \frac{P^2}{2b}\left(\frac{dC}{da}\right) \quad (1.3)$$

This expression is a common basis of energy release rate calculations. Methods developed to determine strain energy release rates through FEA, beam or plate analysis, and experimental methods employ this relation.

Using a crack closure technique, the stress intensity factors, K_I, K_{II}, and K_{III}, can be related to the energy release rate, G, separated into three modes. In this fashion K_I, K_{II}, and K_{III} can be connected to G_I, G_{II}, and G_{III} respectively, where $G = G_I + G_{II} + G_{III}$. This mode separation is based on Irwin's idea that when a crack extends by a small amount, Δa, the energy absorbed in the crack extension process is equal to the energy required to create the new surface and can be calculated by the work required to close the crack to its initial length (5).

$$G_I = \lim_{\Delta a \to 0} \frac{1}{\Delta a} \int_0^{\Delta a} \sigma_y(\Delta a - r, o)\bar{v}(r, \pi)dr \quad (1.4a)$$

$$G_{II} = \lim_{\Delta a \to 0} \frac{1}{\Delta a} \int_0^{\Delta a} \tau_{xy}(\Delta a - r, o)\bar{u}(r, \pi)dr \quad (1.4b)$$

$$G_{III} = \lim_{\Delta a \to 0} \frac{1}{\Delta a} \int_0^{\Delta a} \tau_{yz}(\Delta a - r, o)\bar{w}(r, \pi)dr \quad (1.4c)$$

where r is the radial distance from the crack tip and u, v, and w are the relative opening and sliding displacements in the x, y, and z coordinate directions respectively. If the crack propagation remains in a symmetry plane the components of the energy release rate become (2).

$$G_I = K_I^2 \left(\frac{S_{11}S_{22}}{2}\right)^{\frac{1}{2}} \left[\left(\frac{S_{22}}{S_{11}}\right)^{\frac{1}{2}} + \frac{2S_{12}+S_{66}}{2S_{11}}\right]^{\frac{1}{2}} \quad (1.5a)$$

$$G_{II} = K_{II}^2 \left(\frac{S_{11}}{\sqrt{2}}\right)^{\frac{1}{2}} \left[\left(\frac{S_{22}}{S_{11}}\right)^{\frac{1}{2}} + \frac{2S_{12}+S_{66}}{2S_{11}}\right]^{\frac{1}{2}} \quad (1.5b)$$

$$G_{III} = \frac{K_{III}^2}{2(C_{44}C_{55})^{1/2}} \quad (1.5c)$$

where C_{44} and C_{55} are out-of-plane shear stiffnesses, G_{13} and G_{23}, and S values are components of the composite's compliance matrix.

For problems where an exact solution cannot be obtained a numerical solution using finite element analysis may be approached. Finite element analysis is an analytical tool for the modeling of complex geometries and materials. The area or volume of the structure is divided into several discrete elements defined by nodes at the boundaries of the elements. Material properties and physical governing equations are assigned to each of these elements, boundary conditions are defined, and unknown physical values at the nodes are solved for numerically. The numerical solutions to the equations governing the response of each element represent an approximation of the behavior of the problem (6). A more refined mesh will improve the accuracy of the solution.

Energy release rate components can be computed using numerical finite element analysis methods (virtual crack closure method). Following Eqs. (1.1, 1.2, and 1.3) (2) a crack length increase, Δa, is introduced to the FEA model. The nodes on the cracked surfaces just before the extended crack front are loaded in a manner to close the crack. By determining the force and the distance required to close the crack, the energy release rate can be determined from a numerical solution of the integral Eqs. (1.6a, b, and c). This technique may be applied in three dimensions to yield the energy release components,

$$G_I = \frac{F_v \Delta v}{2w\Delta a} \quad (1.6a)$$

$$G_{II} = \frac{F_u \Delta u}{2w\Delta a} \quad (1.6b)$$

$$G_{III} = \frac{F_w \Delta w}{2w\Delta a} \quad (1.6c)$$

1.4.1 Delamination Test Specimens

Most of the attention in delamination analysis has been focused on mode I fracture. An ASTM standard test method for mode I delamination, ASTM D 5528 (7), utilizes the double cantilever beam (DCB), see Figure 1.7.

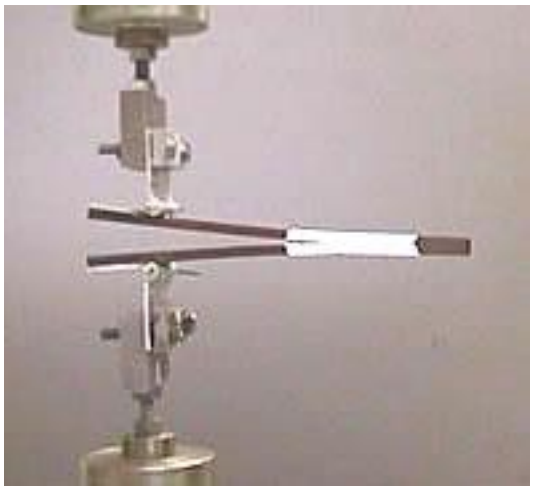

Figure 1.7: Mode I DCB specimen and fixture.

The DCB test is used to determine opening mode (mode I) interlaminar fracture toughness, G_{Ic}, for fiber/matrix composites. The specimen is not precracked because this will cause fiber bridging and increase the resistance to crack growth. The starter crack is produced by inserting a very thin (<13μm) Teflon film at the mid plane. The DCB specimen is loaded through hinge loading tabs, see Figure 1.7. The edges of the

specimen are coated with a thin, white, brittle paint to aid visually locating the crack tip. The specimen is slowly loaded while the crack length, load and deflection are recorded at certain intervals. The crack growth is monitored until the crack has grown 20mm. G_{IC} is then determined for all of the recorded crack lengths using the following equation,

$$G_{IC} = \frac{nP_c\delta_c}{2wa} \tag{1.7}$$

where n is the slope found from the double-logarithmic graph of the stiffness (inverse compliance), P_c/δ_c vs. crack length, a (8).

For determination of the mode II delamination resistance, the end-notched flexure (ENF) specimen, Figure 1.8, is typically used. This test was first introduced to wood (9), and later to composites (10). The ENF test is currently considered for ASTM standardization.

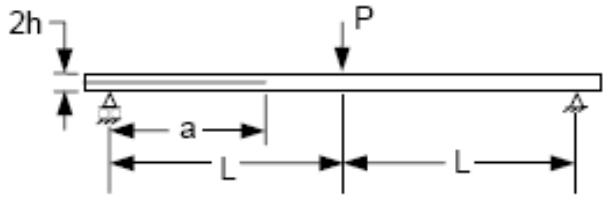

Figure 1.8: Mode II ENF testing geometry.

The ENF test is done by simply loading the ENF specimen in three-point bending until crack propagation occurs at a critical load, P_c. The specimen should fail by crack propagation in the mid plane stemming from the starter crack. G_{IIc} can then be determined using the beam theory (BT) with the following expression,

$$G_{IIc}^{BT} = \frac{9a^2 P_c^2 C}{2w(2L^3 + 3a^3)} \tag{1.8}$$

If compliance calibration (CC) is demanded, the compliance of the ENF specimen is measured over a range of crack lengths. The crack length can be changed simply by sliding the specimen along the fixture. For final fracture testing, the ENF specimen is positioned on the three-point bending fixture to achieve a crack length that will promote unstable crack growth, and the specimen is loaded to failure. A crack length-to-half span ratio of $a/L < 0.7$ will yield unstable crack growth. To achieve a linear plot, the compliance ratio C/C_0 is plotted as a function of $(a/L)^3$, where C_0 is the compliance at zero crack length. The mode II fracture toughness can then be determined using,

$$G_{IIc}^{CC} = \frac{3mP_c^2 a^2 C_0}{2wL^3} \tag{1.9}$$

where m is the slope of the compliance calibration line (8).

1.5 Mode III Delamination Test Specimens

Mode III delamination has not been studied extensively, mostly because of experimental difficulties in achieving a state of pure mode III crack tip loading in a composite specimen (11). Mode III delamination is important from a design standpoint (12). Composite panels are often used in practice and often stiffened with stringers (reinforcement strip fastened to a skin). FE analysis has shown that plates under shear are subjected to substantial mode III loading at the stringer/plate interface (13).

One early proposed mode III delamination test method uses a split double cantilever beam (SCB) specimen with aluminum reinforcement bars bonded to the

unidirectional laminate faces (14), see Figure 1.9. The specimen is loaded in the direction parallel to the crack plane and normal to the beam axis, in agreement with the mode III definition shown Figure 1.6. The load is applied to adhesively bonded metal loading plates, Figure 1.9.

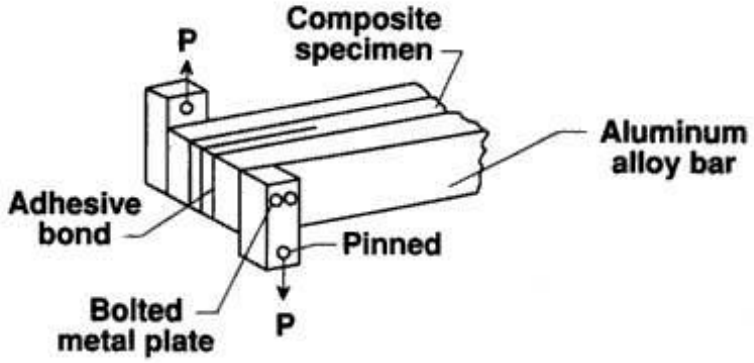

Figure 1.9: Split cantilever beam specimen (SCB).

This method produced fracture of brittle composites, but tougher material combinations suffered from debonding of the loading plates, Martin (15). Finite element analysis (15) shows that the SCB specimen produces a significantly higher G_{II} than G_{III} along the ends of the crack front. Martin proposed a modified loading procedure and the use of a thick split cantilever beam, Figure 1.10. Making the laminates sufficiently thick will increase the torsional stiffness of the legs of the split beam and eliminate the need to bond aluminum bars to the specimen. Load is introduced directly to the legs of the thick split cantilever beam specimen using a loading nose system, Figure 1.10. Still, G_{III} displayed variability along the crack front and significant G_{II} mixity (interaction) occurred.

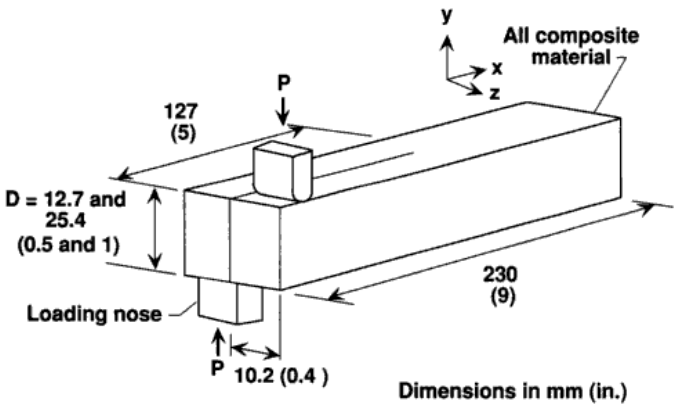

Figure 1.10: Modified split cantilever beam specimen.

Another mode III specimen was proposed by Becht and Gillespie (16; 17). This test uses a modification of the ASTM rail shear specimen (18) with a delamination defined by a non-stick film at the designated interface. The test specimen is loaded under in-plane shear until the delamination grows, see Figure 1.11.

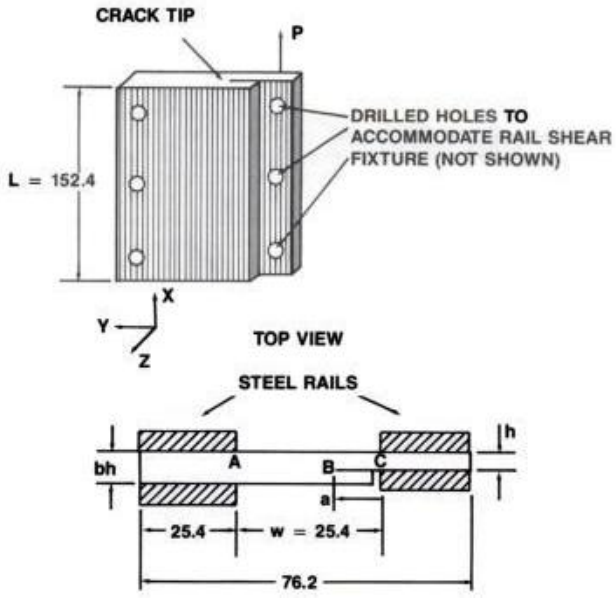

Figure 1.11: Single crack CRS specimen (all dimensions in mm)

The crack rail shear (CRS) specimen uses a lay-up of $[90_2/\pm45]_{sp}$, where *s* represents a symmetric lay-up and *p* is an integer that may be varied based on the magnitude of delamination toughness, G_c. G_c for a single crack specimen can be determined from a strength of materials analysis (2),

$$G_c = \frac{P^2(G_{AB}b - G_{BC})}{2L^2hG_{AB}G_{BC}b} \tag{1.10}$$

where G_{AB} and G_{BC} are the shear moduli of sections *AB* and *BC* of the CRS specimen. P is the load applied to the specimen, and the dimensions used in the equation are defined in Figure 1.11. Notice that *b* is a dimensionless coefficient such that *bh* equals the total thickness. The CRS configuration is very stiff, and makes application of the experimental compliance calibration method inaccurate.

A major development towards a mode III test procedure was the introduction of the edge-cracked torsion (ECT) test by Lee in 1993 (19). Figure 1.12 shows the ECT test fixture and specimen. The test specimen is a rectangular composite plate containing an edge delamination at the mid-plane. The crack plane lies between the symmetric halves of the composite in the 90°/90° ply interface, where the xyz coordinate system is shown in Figure 1.12. Hence, with the delamination between two 90° plies, growth is supposed to occur in the fiber direction, similar to the DCB and ENF specimens discussed earlier.

Lee (19) used ECT specimens with lay-ups of $[90/\overline{\pm45}_n/\overline{\pm45}_n/90]_s$ with n=3 (28 plies) and n =4 (36 plies). The purpose of the ±45° plies in this lay-up is to increase the twist stiffness of the ECT specimen.

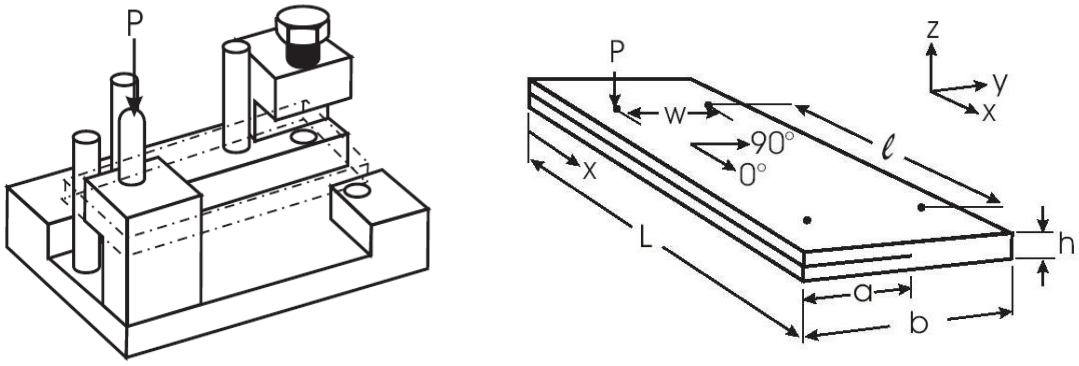

Figure 1.12: Original (one-point) ECT test fixture and detail of the test specimen.

The test fixture is designed so that three corners of the plate are supported by pins with rounded ends, while one corner is loaded with a rounded pin in a direction normal to the plane of the panel. The loading produces a torque that twists the panel and loads the crack front in mode III. Detailed finite element analysis by Li et al. (20) (21) has shown that a state of approximately pure mode III loading is achieved in the ECT specimen. The plate torsion test is sometimes also called "anti-clastic plate bending method" (22) since pure torsion loading of an orthotropic square plate produces a twisting shape of the plate that may be viewed as a anticlastic double curvature bending shape (saddle shape) at $\pm 45°$ directions as shown in Figure 1.13.

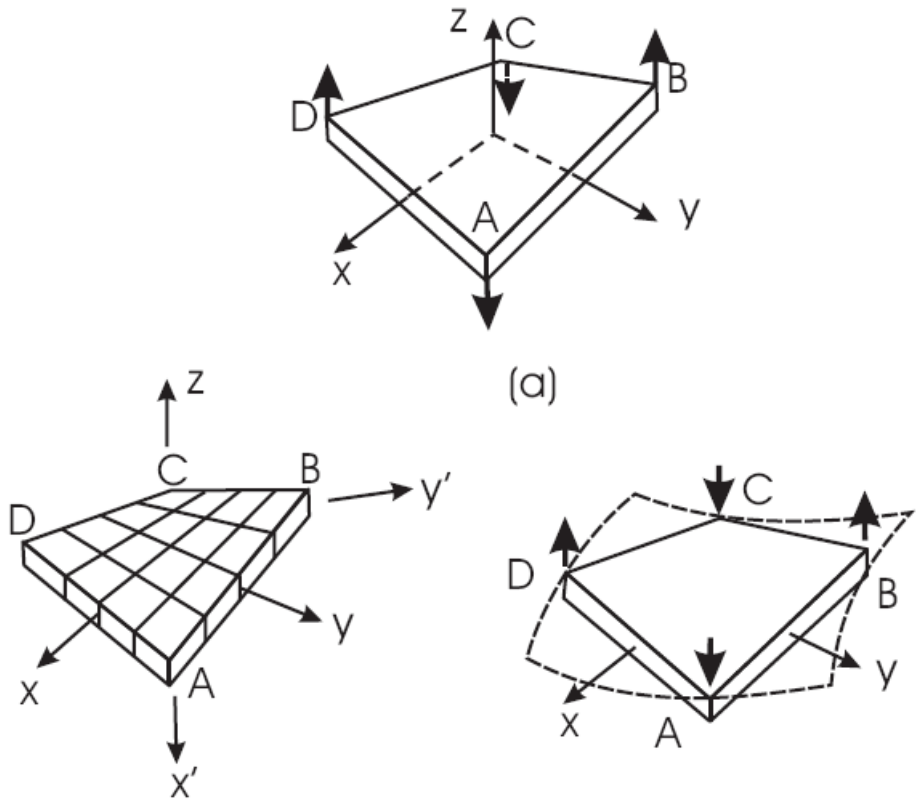

Figure 1.13: Anti-clastic curvature shape of a twisted square plate.

A round-robin ECT test program was organized by the ASTM D30 committee in the late 1990's (23). The purpose of the test program was to examine the viability of the one-point ECT test method for delamination characterization of a toughened carbon/epoxy composite. Large scatter in the measured fracture toughness, G_{IIIc} , and nonlinear response were reported by the participants as well as serious skews in the crack front growth. After this exercise the loading fixture was modified so as to introduce a symmetrical load introduction at two opposite corners of the plate as shown in Figure 1.14. This fixture is referred to as the two-point ECT test fixture.

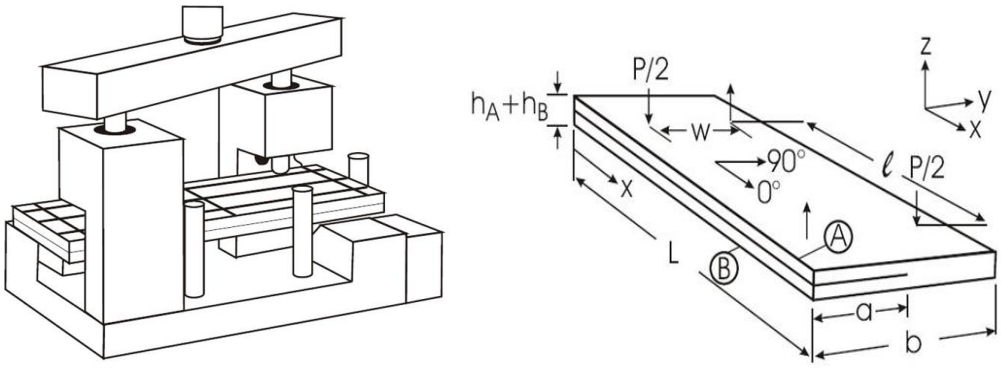

Figure 1.14: Two-point ECT fixture for mode III delamination testing.

The corners of the ECT specimen are loaded using steel pins with rounded ends guided by linear bearings. Load is transferred from the test machine into the pins using a loading beam that is simply supported at the center to produce equal share of the compressive load, P. In addition to the modification of the test fixture, the lay-up was modified to include zero-degree plies: $[0/0/\mp 45_s/\mp 45_s/0/90]_s$.

A second round-robin test program was organized in 1999 based on glass/epoxy and carbon/epoxy composites (24). Testing and analysis conducted within this program revealed that the crack in glass/epoxy specimens sometimes propagated along the 90°/0° ply interface instead of the intended 90°/90° mid-plane. Furthermore, finite element analysis revealed a significant mode II energy release rate component, G_{II}, near the loading pins (24). To remedy these deficiencies, the specimen length, L (Figure 1.14b) was increased from 82.5mm to 108 mm (24) with the effect of distributing the mode II component over a larger overhang area and lowering its peak value. The original one-point and modified two-point ECT specimen geometries can be seen in Figure 1.15.

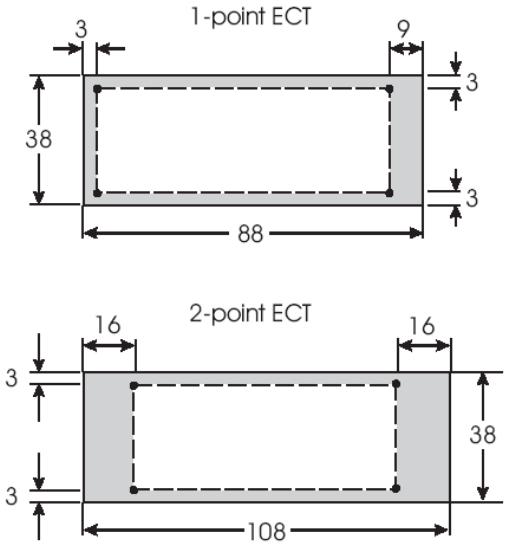

Figure 1.15: Plate dimensions and loading of one-point and two-point ECT panels. The dots represent loading and support points, and the shaded area the overhang regions. All dimensions are in mm.

Figure 1.15 shows the plate and loading configurations for the one-point and two-point ECT tests. The box created by the four load/support points has the dimensions 32x76 (mm) for both configurations. It is noted that the overhang area in the one-point configuration is asymmetrical while the loading area for the two-point is symmetric.

The modified test fixture and ECT specimen was thoroughly examined in an experimental and analytical study conducted by Ratcliffe (25). Several glass/epoxy and carbon/epoxy specimens were tested over a range of delamination lengths, and detailed 3D finite element analysis was conducted.

Ratcliffe used the virtual-crack-closure-technique, see Section 1.4, in an ABAQUS finite element model of the ECT specimen to determine the mode II and mode

III components of the energy release rate, G_{II} and G_{III}, along the delamination front of the ECT specimen.

The results have shown that G_{III} peaks along the center of the crack front and decreases towards the edges of the specimen (26). The distributions of G_{II} and G_{III} change with crack length. For short crack lengths (a/b=0.2) the distribution of G_{III} is quite uniform. For long crack lengths (a/b=.6), G_{III} is nonuniformly distributed with a peak at the center. The mode II component, G_{II}, peaks at the load introduction and support locations of the specimen and tapers off to approximately zero in the center of the specimen and at the edges. These effects are shown in Figure 1.16.

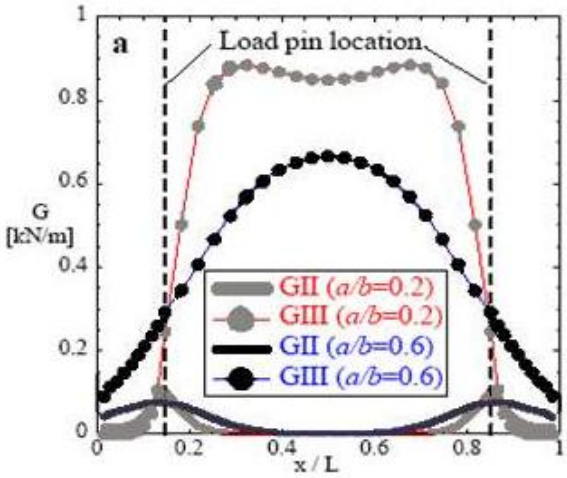

Figure 1.16: Strain energy release rate distribution across the delamination front for a carbon/epoxy ECT specimen. (25)

The current specimen and test procedure have a few unresolved issues. One just pointed out is the presence of G_{II} along the crack front. Another issue is nonuniform crack growth. Crack growth tends to initiate at the center of the ECT specimen where

G_{III} is maximum. This has been detected by injecting X-ray sensitive ink into the fractured crack and then viewing an X-radiograph of the ECT specimen (25). It is likely that the variation of G_{III} and presence of G_{II} along the crack front are contributing to the nonuniform crack growth. It has also been found that the mode III fracture toughness, G_{IIIc}, increases with crack length. This is a major problem because a material property, such as G_{IIIc}, should not change with geometry. Ply splitting and a jumping of the delamination to the interface between the 0° and 90° plies has also been reported (25).

1.6 Research Objectives

Based on the review of the various mode III delamination tests presented in Section 1.5 it is clear that the ECT test is the most promising, but several problems remain to be resolved before this test can be considered for ASTM standardization. This thesis will experimentally and analytically examine ways to improve the ECT test.

The project includes a comprehensive experimental characterization of the in-plane mechanical properties of the glass/epoxy and carbon/epoxy composites considered. ENF testing is conducted in order to determine the mode II fracture toughness and the influence of precracking on G_{IIc}. This study produces a reference for the subsequent mode III toughness (G_{IIIc}) and isolates the influence of precracking on the delamination toughness. Precracking of the ECT specimen is not possible.

The one-point and two-point ECT fixtures are compared in a test program on glass/epoxy and carbon/epoxy laminates with a $[0/0/\pm 45_2/\pm 45_2/0/90]_s$ lay-up. Each test method is examined based on consistency of G_{IIIc} over a range of crack lengths,

relevance of data reduction methodology, and repeatability of measured toughness (G_{IIIc}). Testing of overhang (specimen geometry outside of the load/support points) effects on the compliance and fracture toughness was conducted on carbon/epoxy laminates using a specially designed two-point ECT fixture where the specimen dimensions can be changed.

Finite element simulations are conducted on isotropic and orthotropic uncracked ECT specimens to examine the influence of indentation on the compliance. Another important objective is to identify the effects of overhang on the compliance and distributions of interlaminar shear stresses along the crack front of ECT specimens. Efforts to improve data reduction are investigated using alternative methods of compliance calibration.

A modified ECT specimen is proposed, employing a staggered crack front (SECT specimen) as defined by the insert geometry. The SECT specimen utilizes two crack fronts; one near the edge regions with low shear stresses, and one at the center region where mode III crack growth is expected. This should force crack growth to occur only in the center section. The SECT specimen is analyzed using finite elements with the purpose of designing the insert for achieving a uniform mode III loading along the primary crack front.

2 Experimental Testing

In this chapter basic mechanical property characterization of the carbon/epoxy and glass/epoxy composites employed in this study will be conducted experimentally. Such data are required for the analysis subsequently presented in Chapter 3. Tests of carbon/epoxy and glass/epoxy ECT specimens with dimensions according to the ASTM pre-standard document will be done followed by testing of specially sized carbon/epoxy ECT specimens designed to examine the effects of overhang. For this purpose, a new two-point ECT fixture that permits testing of ECT specimens with different dimensions was designed and built.

2.1 Basic Material Properties Characterization

The two composite materials of interest are carbon/epoxy and glass/epoxy obtained from Bell Helicopter. All test specimens were made from these two composites. In order to properly model the specimens using analytical methods and FEA simulations, a series of tests was used to obtain an accurate measure of the basic material properties. The basic material properties were determined from tensile tests on laminated test specimens (8).

2.1.1 Fiber Volume Fraction

Fiber volume fraction of the glass/epoxy and carbon/epoxy was measured using the photomicroscopical method outlined by Adams et al. (8). Small samples were cut perpendicular to the fiber axis from the unidirectional composites. The samples were molded in bakelite sample holders, then sanded and polished down to a 0.3 micron

polishing compound. After this polishing procedure the glass and carbon fibers can be clearly recognized in an optical reflection microscope, see Figure 2.1.

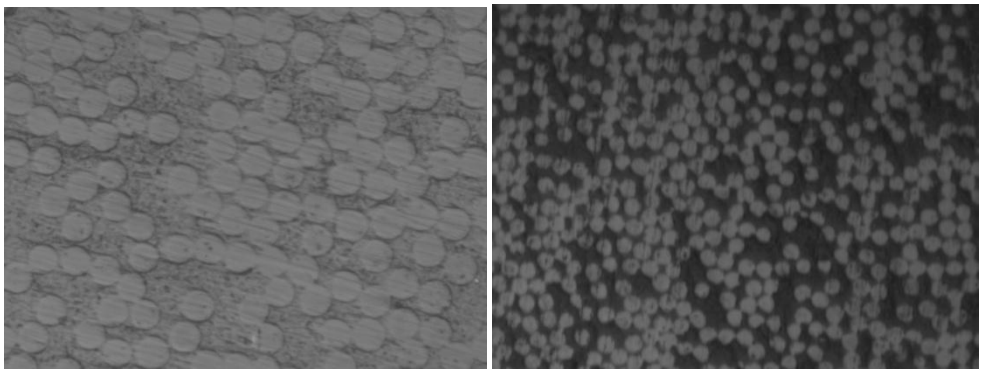

Figure 2.1: Polished views of 0° composite cross-sections.
a) glass/epoxy. b) carbon/epoxy.

For determination of the fiber volume fraction, a square section is chosen and its area determined. The average diameter of the fibers is then measured and the average fiber cross-sectional area is calculated. The number of fibers in the section is added up and total area taken up by fiber cross-sections calculated. The volume fraction, V_f, is calculated by dividing the fiber area by the total area in the section. The fiber volume fractions were .53 and .54 for glass/epoxy and carbon/epoxy, respectively.

Determining void content is difficult as voids are not distributed nearly as uniformly as the fibers. Voids tend to be in groups and given that the area viewed in the micro-scope is very small, either no voids are present or a large portion of the visual area is covered by voids. The micrographs shown in Figure 2.1 reveal some voids but they represent a minor percentage of the total cross-sectional area, indicating that good quality composites were received.

2.1.2 Tensile Testing

Testing was done on a Tinius Olsen Universal Testing Machine with a load capacity of 130 kN. The means for data collection from this machine were retrofitted with an extremely flexible and adaptable data acquisition system. Data acquisition is implemented through LABVIEW which is a DAQ program developed by National Instruments (27). The abilities of this system allow us to create a unique interface for data collection that can record multiple synchronized data, manipulate, and calculate properties from raw or filtered data and display results numerically as well as graphically in real time. The testing utilized readings from the load cell, an LVDT used to measure displacement, and strain gages. Other sensors can be implemented as needed. For simple material tensile testing the current graphical interface enables easy and repeatable data collection and reduction. The system allows for easy calibration and zeroing or offsetting for all signal inputs.

The basic mechanical properties of the glass/epoxy and the carbon/epoxy composites were determined from tensile testing following the guidelines of Adams et al. (8). 30 specimens were tested in total with 5 replicates of glass/epoxy and carbon/epoxy for the 0º, ±45º, and 90º lay-ups. All 0º specimens were end tabbed to prevent failure at the grips which otherwise may occur as an effect of the stress concentrations created from grip teeth digging in to the specimen. Failure in the grips is most apt in the 0° specimen due to their very high ultimate tensile strength.

Strain gages are needed to collect accurate strain data. Three specimens from each glass/epoxy and carbon/epoxy lay-up were equipped with strain gages. The 0º and

±45º specimens were prepared with 0º/90º strain gage rosettes. The 90º specimens were prepared with strain gages in the axial direction only.

Tensile tests were first done on 0º specimens. E_1 (modulus in the fiber direction), v_{12} (Poisson's ratio), and X^T_1 (tensile strength) were reduced from the load and strain data. These values were calculated using the following formulas where σ_1 is the average stress in the fiber direction, ε_1, and ε_2 are the strains along and transverse to the fiber direction (8). Stress is calculated by the load, *P*, divided by the area, *A*, with *A*, being the product of the thickness, *t*, and width, *w*, of the specimen. The strains were measured directly with strain gages.

$$E_1=\Delta\sigma_1/\Delta\varepsilon_1 \tag{2.1a}$$

$$v_{12}= -\varepsilon_2/\varepsilon_1 \tag{2.1b}$$

The elastic constants were determined from the linear response region. The failure strength is determined from,

$$X^T_1= \text{ultimate value of } \sigma_1 \tag{2.1c}$$

Figure 2.2 shows representative stress-strain curves for 0º carbon/epoxy and glass/epoxy specimens in tension.

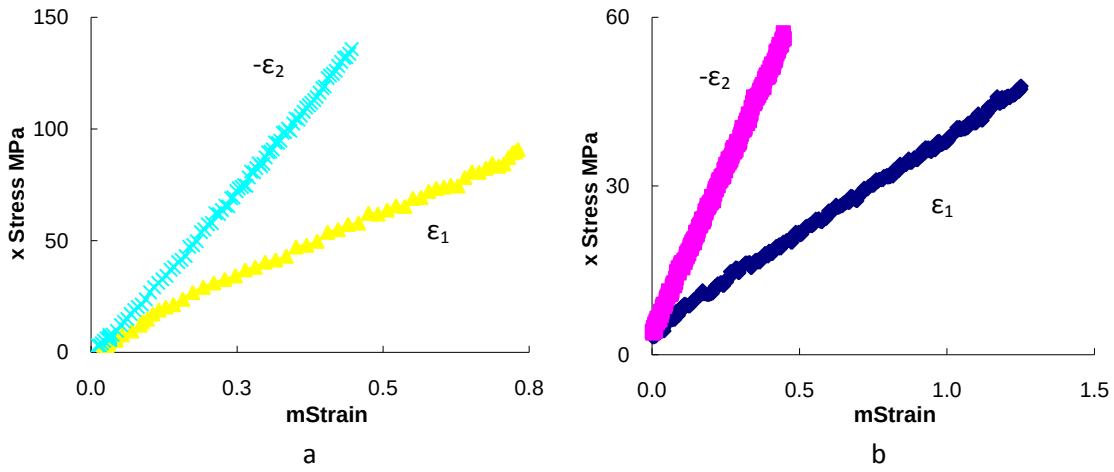

Figure 2.2: Stress-strain curves for 0º specimens.

a) carbon/epoxy. b) glass/epoxy.

The strain is recorded in the 0° and 90° direction. The results shown in Figure 2.2 covers the data recorded up until the strain gages exceed there operational strain envelope. The testing was continued until failure to determine ultimate tensile strengths but the strain values did not rise past the range shown in Figure 2.2. The curves are very linear in the displayed range which was sufficient in determining E_1 from Figure 2.2. The Poisson ratio, v_{12}, was determined from the strain-strain graphs shown in Figure 2.3.

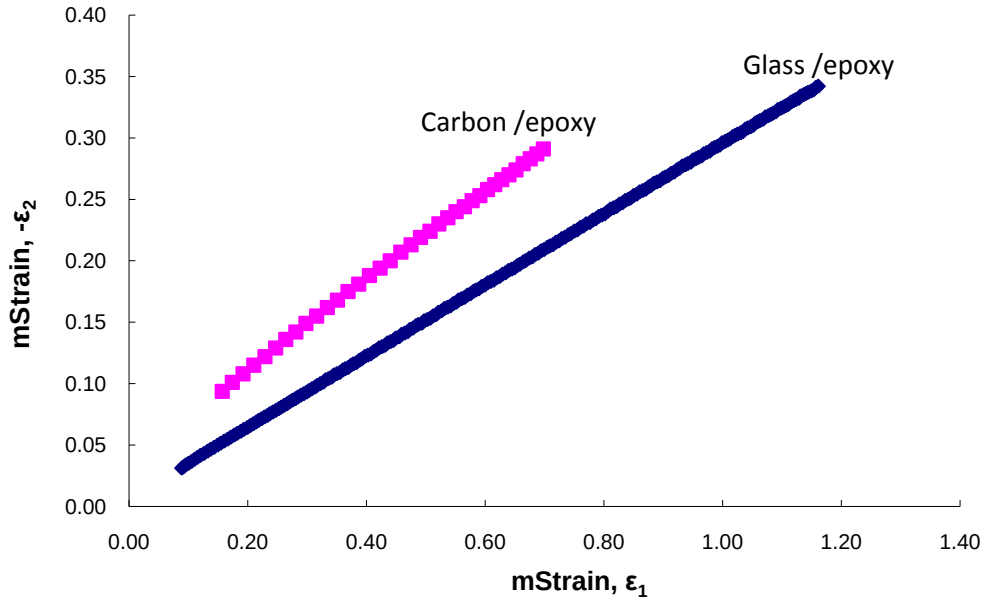

Figure 2.3: 90º strain versus 0º strain curves for 0° carbon/epoxy and glass epoxy specimens.

The transverse modulus, E_2, and tensile strength, X^T_2, are reduced from load-strain data recorded from 90º specimens using Equations (2.2).

$$E_2=\Delta\sigma_2/\Delta\varepsilon_2 \qquad (2.2a)$$

$$X^T_2 = \text{ultimate value of } \sigma_2 \qquad (2.2b)$$

where $\sigma_2=P/wt$. Stress-strain graphs for carbon/epoxy and glass/epoxy, enabling determination of E_2, can be seen in Figure 2.4. Figure 2.4 also shows that stress-strain curves with strain reduced from the cross head displacement and $(\Delta L / L_0)$, fall far below the actual curve. This inaccuracy is attributed to several factors. The cross head displacement includes the displacement of the machine and any fixturing used in testing such as the load cell, grips and the bar connecting the grip to the testing machine.

Another large contributor to the inaccuracy is the slip that occurs in the gripping fixture. Slip that occurs in grips may be substantial and contributes to the large apparent compliance readings for the specimens.

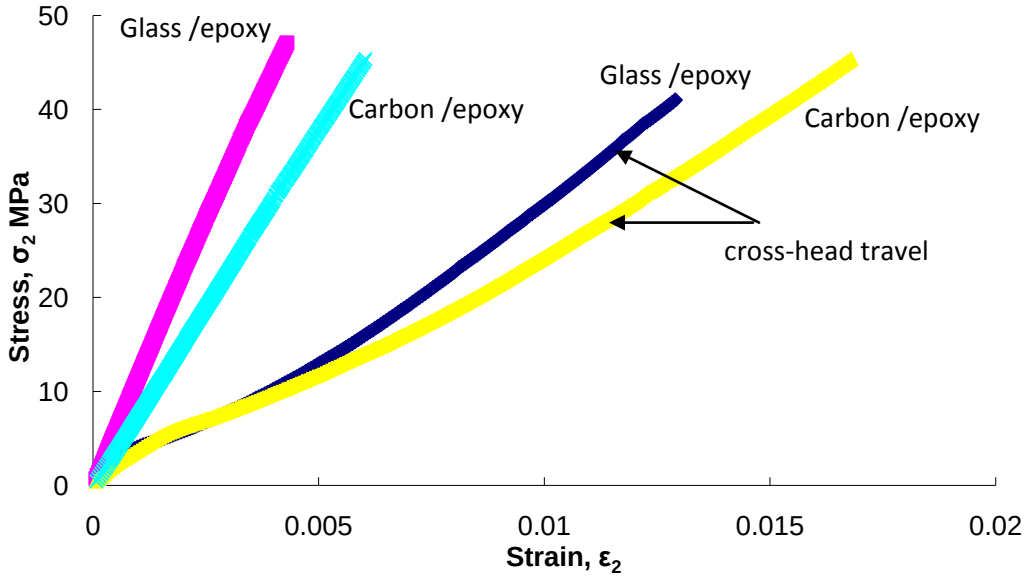

Figure 2.4: Stress-strain curves for carbon/epoxy and glass/epoxy $[90]_{26}$ specimens.

The final set of testing for the basic material properties was done on ±45º tensile specimens to determine the in-plane shear properties of the unidirectional lamina. The properties determined include in-plane shear modulus, G_{12}, ultimate shear stress, S_6, and strain, e_6. The shear stress, τ_{12}, is determined from the axial stress, $\sigma_x=P/wt$ (8),

$$\tau_{12}=\sigma_x/2 \qquad (2.3a)$$

and the shear strain, γ_{12}, is determined from the difference between the axial and transverse strains,

$$\gamma_{12}=\varepsilon_x-\varepsilon_y \qquad (2.3b)$$

The shear modulus, G_{12}, is the ratio between shear stress and shear strain (γ_{12}<<1).

$$G_{12} = \frac{\tau_{12}}{\gamma_{12}} \tag{2.3c}$$

where ε_x and ε_y are the axial and transverse strains, respectively. The shear strength, S_6, is defined as the shear stress, τ_{12}, at failure. This test method is ASTM standard D 3518, "In-Plane Shear Response of Polymer Matrix Composite Materials by Tensile Test of a ±45° Laminate". Shear stress – shear strain curves for carbon/epoxy and glass/epoxy are shown in Figure 2.5.

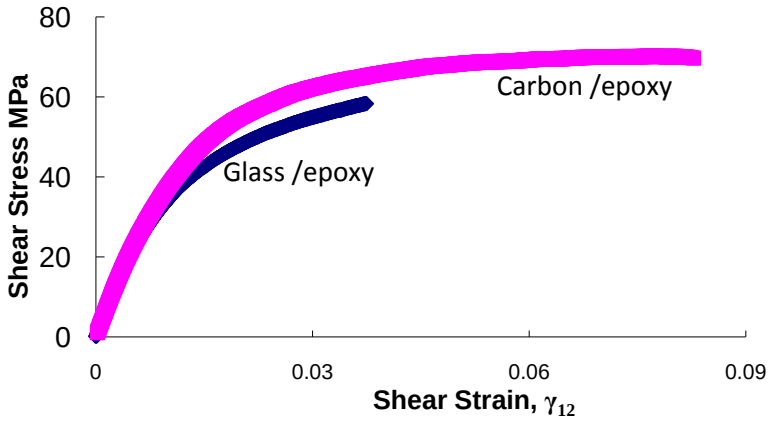

Figure 2.5: Shear stress-strain curves for carbon/epoxy and glass/epoxy.

Figure 2.5 shows the in-plane shear response of the carbon/epoxy and glass/epoxy composites. The in-plane shear modulus, G_{12}, is determined from the initial linear portion of the curve in Figure 2.5. The response curves after the initial linear region become highly nonlinear and beyond a shear strain of about .03 the shear stress is relatively constant. The basic material properties for glass/epoxy and carbon/epoxy determined from these tests are displayed in Table 2.1.

Table 2.1: Basic material properties for glass/epoxy and carbon/epoxy.

	Glass/Epoxy					Carbon/Epoxy				
	1	**2**	**3**	**AVG**	**STD**	**1**	**2**	**3**	**AVG**	**STD**
E_1 GPa	34.4		32.6	**33.5**	1.27	116	112	110	**113**	3.15
E_2 GPa	10.5	10.2	12.7	**11.1**	1.35	7.53	7.30	7.07	**7.30**	0.230
ν_{12}	0.289			**0.289**		0.361	0.354	0.353	**0.356**	0.00436
G_{12} GPa	4.63	4.64		**4.64**	0.00707	4.50	3.78		**4.14**	0.513
S_6 MPa	71.3	69.74		**70.5**	1.10	70.2	64.9		**67.6**	3.75
e_6 %	13.0			**0.130**		7.73	6.73		**7.23**	0.707
X^T_1 GPa	1.22			**1.22**		2.39			**2.39**	
e^T_1 %	3.54			**3.54**		2.06			**2.06**	
X^T_2 MPa	79.3	60.3	82.0	**73.9**	11.8	54.5	55.0	54.5	**54.7**	0.289
e^T_2 %	0.74	0.57	0.66	**0.66**	0.000836	0.72	0.76	0.78	**0.753**	0.0316
V_f	**0.53**					**0.54**				

'AVG' and 'STD' refer to average and standard deviations of the data.

Except for a few specimens where the strain gages malfunctioned or popped off, the data collected were repeatable and consistent. The mechanical properties in Table 2.1 may be compared to experimental data published by Daniel and Ishai (1) listed in Table 2.2.

Table 2.2: Basic material properties for glass/epoxy and carbon/epoxy.

	Glass/Epoxy	**S-Glass/Epoxy**		**Carbon/Epoxy**	**Carbon/Epoxy IM7/977-3**	
	Current	**Ref** (1)	**% difference**	**Current**	**Ref** (1)	**% difference**
E_1 GPa	**33.5**	**45**	-26	**113**	**190**	-40.8
E_2 GPa	**11.1**	**11.0**	1.3	**7.3**	**9.9**	-26.3
ν_{12}	**0.289**	**0.290**	-0.35	**0.356**	**0.35**	1.7
G_{12} GPa	**4.64**	**4.50**	3.0	**4.14**	**7.80**	-46.9
S_6 MPa	**70.5**	**70.0**	0.74	**67.6**	**75.0**	-9.9
e_6 %	**13.**			**7.23**		
X^T_1 GPa	**1.22**	**1.73**	-30	**2.39**	**3.25**	26.5
e^T_1 %	**3.54**	**2.90**	22	**2.06**	**1.60**	28.8
X^T_2 MPa	**73.9**	**49.0**	51	**54.7**	**62.0**	-11.8
e^T_2 %	**0.66**	**0.60**	9.3	**0.75**	**0.6**	25.4

The data collected agrees with those from Daniel data for the most part. Some properties differ substantially but it must be pointed out that the fiber volume fractions and matrix epoxies are different which would account for most deviations. Judging by

the lower modulus in the longitudinal direction of the current study specimens it can be assumed that the fiber volume fraction of the current specimens is less than the reference. The higher ultimate tensile strains of our specimens are also consistent with a lower fiber volume fraction.

2.2 Mode II ENF Fracture Testing

Mode II fracture testing has been conducted on unidirectional glass/epoxy and carbon/epoxy composites. Fracture testing was conducted on both non-precracked and precracked specimens using the end-notched flexure (ENF) test discussed earlier in Section 1.4. Non-precracked refers to fracture testing by propagating a delamination from the edge of the insert film. Data reduction for the mode II fracture toughness, G_{IIc}, employed experimental compliance calibration and classical beam theory. As discussed in Section 1.5, mode III testing tends to involve also mode II. Hence, it is important to determine the amount of G_{II} required to propagate a crack. Further, since both mode II and mode III loadings involve interlaminar shear fracture it is anticipated that G_{IIc} and G_{IIIc} will be similar.

The test methodology for the ENF specimen consists of: 1) compliance calibration of a non- precracked ENF specimen, 2) a technique to precrack the specimen to consistently produce a reasonably straight precrack, 3) measuring the precrack length, and 4) final fracture testing to determine the fracture toughness. The ENF test principle is shown in Figure 1.8. Figure 2.6 shows the specific dimensions of the ENF specimens tested here.

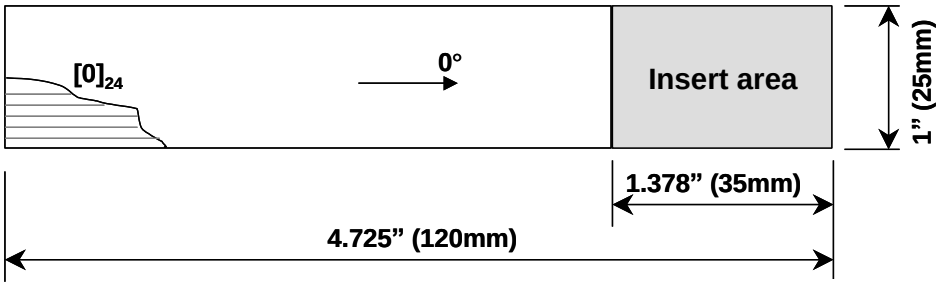

Figure 2.6: ENF test and specimen geometry.

The ENF specimens were tested on a standard 3-point flexure test rig. The crack length, *a*, is the distance from the left support to the end of the insert in the case of a non-precracked specimen. For a precracked specimen, *a*, is the distance from the support to the crack tip.

Compliance calibration was conducted on non-precracked specimens only. Compliance calibration was done by loading each specimen at several specific *a/L* ratios at a load safely below that for crack propagation. The compliance, $C=\delta/P$, can be determined from the linear portion of the load-displacement curve, where δ represents the displacement at the loaded point of the specimen, and *P* the load applied. The compliance can be plotted as a function of the *a/L* ratio as shown in Figure 2.7a. To achieve a linear relation, the compliance ratio C/C_0 is plotted as a function of $(a/L)^3$, see Figure 2.7b. C_0 represents the compliance at zero crack length.

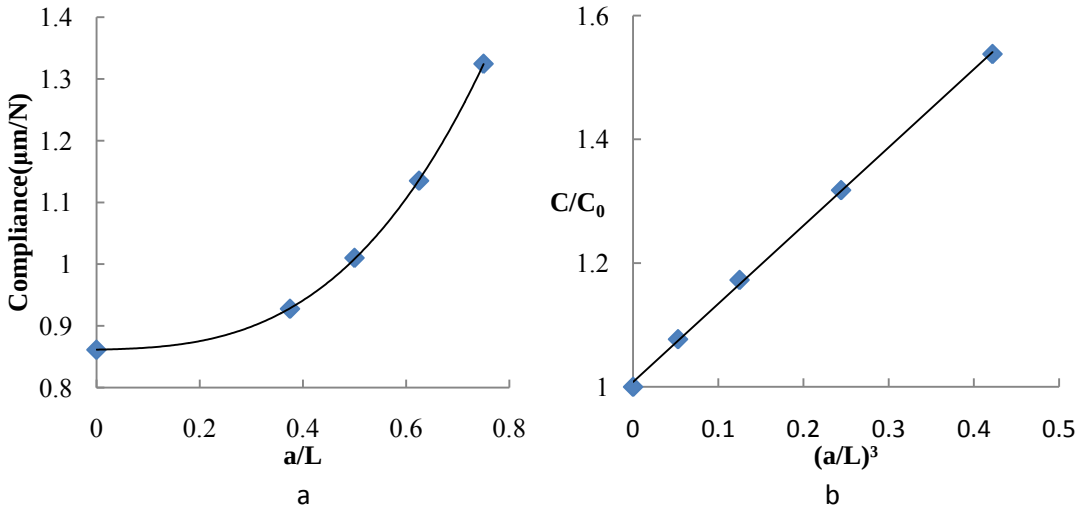

Figure 2.7: ENF compliance curves for glass/epoxy (specimen #13).
a) Compliance as a function of normalized crack length.
b) Normalized compliance as a function of crack length ratio cubed.

2.2.1 Test Procedure

Unidirectional 24 ply carbon/epoxy and glass/epoxy composites were tested. The carbon/epoxy and glass/epoxy specimens were 4.5 and 7.5mm thick. Each material had 20 replicate specimens prepared. The insert length was 35mm, measured from the edge of the specimen. The span length, 2L was 80mm and five crack lengths, a=0, 15, 20, 25, and 30mm, were selected for compliance calibration. Testing was conducted at a cross head rate of .0127 mm/sec.

The second step in the testing program is to extend the crack from the insert film to achieve a natural precrack. When the specimens are processed there is a slight build-up of epoxy resin at the end of the insert. This build-up may provide the specimens with a greater ability to resist delamination than that of a naturally cracked specimen. Therefore, it may be necessary to slightly extend the crack before determining G_{IIc}. There are several ways to create a precrack. One method of pre-cracking uses mode I opening

loads but the result is that the crack front may include a zone of bridged fibers and this may influence G_{IIc}. Another precracking method uses cyclic mode II loading to achieve natural precrack. This method has been studied the least and would be lengthy for us to apply. The third method uses a static mode II test to create a precrack. This is the method used in this report.

The most crucial part of the precracking procedure is the achievement of a straight crack front. Crack length deviations should not exceed 2.8mm, i.e., $a_{max} - a_{min} < 2.8mm$, as proposed by Davidson (28). The crack lengths a_{max} and a_{min} are the maximum and minimum crack lengths across the crack front. The only open variable that can be changed prior to precracking is the crack length, a, Figure 1.8. To produce an a/L ratio of 0.6 a crack length of a=24mm and a half span length, L=40mm, were selected. When a crack propagates slowly so that the extension of the crack can be controlled, the crack growth is considered stable. An a/L ratio > 0.7 will yield stable crack growth. Davidson (28) found, however, that stable crack growth does not consistently create a straight crack front. Actually unstable growth has been found to provide a much straighter crack front.

The current testing procedure (8) dictates a cross head rate between 0.0083 and 0.0167mm/s (8). The cross head rate used for precracking was 0.0127mm/sec. After precracking it is important to precisely determine the length of the crack. For the transparent glass/epoxy specimens, the precrack can be seen fairly easily without any aids. The carbon/epoxy crack tip is not easily detectable. By painting the specimen edges white, one can more easily observe the tip of the crack. Notice that detection of the position of the crack tip from visual observations of the specimen edges is impeded

by the closure of the mode II crack tip. Using a microscope to examine the edge of the specimen and slightly wedging the specimen open proved to be beneficial to accurate determinations of the crack length.

Final fracture testing of the specimen was conducted in the same manner as the precrack procedure. The only difference is that the crack length, a, is now measured from the precrack tip. The actual crack length was verified from the compliance recorded during the final fracture test using the previously conducted compliance calibration, see Figure 2.7.

2.2.2 Mode II Delamination Toughness

The mode II delamination toughness G_{IIc} is reduced in two ways. G_{IIc} is first determined using the beam theory expression derived by Russell and Street (10)

$$G_{IIc}^{BT} = \frac{9a^2 P_c^2 C}{2w(2L^3 + 3a^3)} \tag{2.4}$$

Here, the compliance, $C=\delta/P$, is determined from the slope of the linear portion of the fracture test. The critical load, P_c, is determined from the maximum load recorded prior to crack propagation and a is the crack length as depicted in Figure 1.8.

The second method for determining G_{IIc} uses the experimental compliance calibration method. Measured compliance values, C, normalized by the compliance at zero crack length, C_0, are graphed vs. (a/L), see Figure 2.7b.

$$\frac{C}{C_0} = 1 + m\left(\frac{a}{L}\right)^3 \tag{2.5}$$

The slope of the compliance calibration plot (C/C_0) vs. $(a/L)^3$ is referred to as m. The crack length measured in the final fracture test should be verified by matching the measured compliance to that of the experimental compliance calibration plot. When the crack length is consistent the following equation is used to determine G_{IIc},

$$G_{IIc}^{CC} = \frac{3mP_c^2 a^2 C_0}{2wL^3} \tag{2.6}$$

The two methods result in two G_{IIc} values G_{IIc}^{BT} and G_{IIc}^{CC}. Those values should be consistent. If the toughness values differ, this may indicate a crack front that is not straight or some other imperfection in the geometry, material, or test procedure.

2.2.3 ENF Test Results

Load-displacement data for the carbon/epoxy and glass/epoxy specimens were recorded. Figure 2.8 shows load-displacement curves for carbon/epoxy (specimen #8) and glass/epoxy (specimen #13) tested at low loads (<700N) at several crack lengths to enable compliance calibration. After the initial nonlinear, stiffening behavior, the load-displacement curves become highly linear. Compliance for each crack length is found from the linear portion of the curves. That is, compliance is calculated from the inverse slope of the linear portion of the P-δ curve.

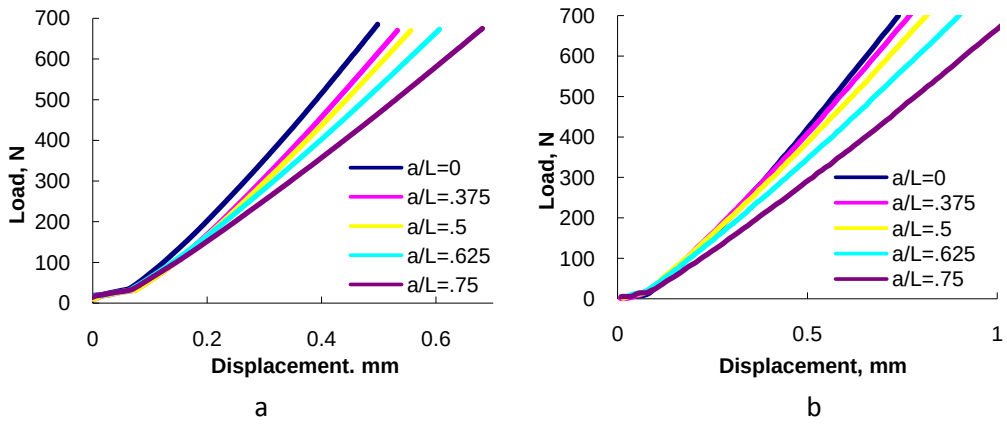

Figure 2.8: Load-displacement curves for ENF specimen.
a) carbon/epoxy specimen #8. b) glass/epoxy specimen # 13.

Figure 2.9 shows load-displacement records for fracture tests of non-precracked and precracked carbon/epoxy and glass/epoxy ENF specimens. The non-precracked carbon/epoxy specimen failed at a higher critical load than the precracked carbon/epoxy specimen, Figure 2.9a. This effect is widely known and is attributed to bluntness of the artificial precrack created by the insert film. For glass/epoxy, however, Figure 2.9b, the response curves for the particular precracked and non-precracked specimens are similar.

Data reduction for G_{IIc} assumes that the precrack tip is straight and uniform. Five specimens of each material were wedged open after precracking to allow inspection of the precrack front, It was observed that the fronts were straight in all cases, well within the $\Delta a < 2.8$mm limit stipulated by Davidson (28).

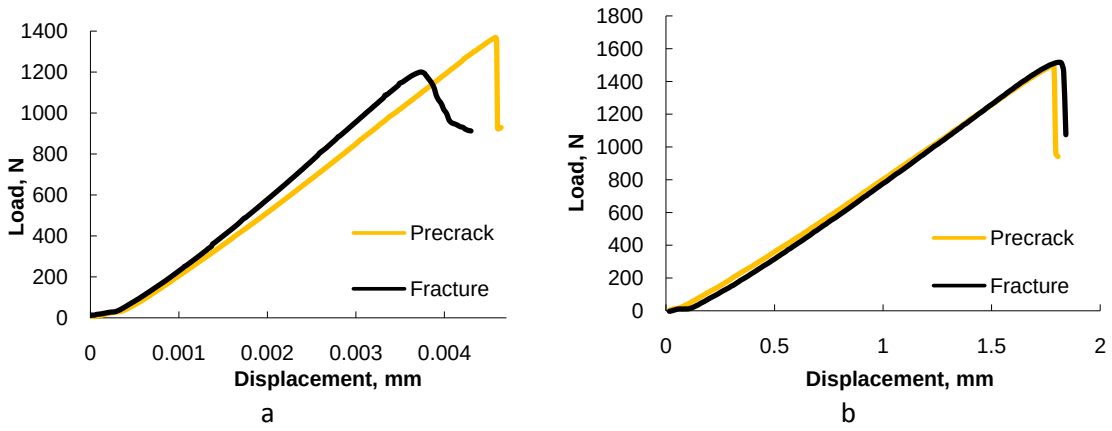

Figure 2.9: Load-displacement curves for ENF specimens during precracking and fracture testing. (a/L=0.6) a) carbon/epoxy specimen #8. b) glass/epoxy specimen # 13.

After the completion of compliance calibration and precrack/fracture testing it is possible to determine G_{IIc}. Table 2.3 summarizes geometrical dimensions, crack extensions as well as G_{IIc} data for the glass/epoxy specimens. Two crack extensions are listed in Table 2.3, viz., "precrack" and "fracture". The precrack extension refers to the extent of crack growth that occurred during the precracking procedure. Notice that both the precracking and fracture testing were conducted at a nominal crack length-to-span ratio, a/L=0.6. Hence, an L=40mm span length corresponds to a crack length a=24mm. The crack extension was about 15-20mm for most specimens indicating arrest near the central load nose. The crack extension column labeled "fracture" refers to the accumulated amount of crack growth observed from the end of the insert film during the precracking and fracture tests. The amount of additional crack extension occurring during the fracture test was approximately the same as during precracking, consistent with a/L=.6 and crack extension to the center.

Considering the fracture toughness data, it is observed that the beam theory and compliance calibration (Equations (2.4) and (2.5)) produce quite similar values indicating an appropriate testing procedure. The beam theory method provides more consistent toughness values based on the scatter (standard deviation), but the difference is quite small. On average the non-precracked fracture toughness is about 12% higher than the precracked.

Table 2.3: Glass/epoxy ENF specimen dimensions, crack extensions, and G_{IIc} data.

Specimen #	b (mm)	2h (mm)	Crack extension,mm		GIIc, kJ/m²			
			Precrack	Fracture	Non-Precracked		Precracked	
					BT	CC	BT	CC
1	25.5	5.45	15.0	31.5	1.265	1.069	1.094	0.903
2	25.5	5.50	18.5	33.6	1.116	0.957	1.073	0.961
3	25.5	5.58	15.6	31.0	1.156	1.037	1.131	1.002
4	25.5	5.68	16.0	29.7	1.143	0.945	1.120	0.925
5	25.4	5.66	15.2	27.5	1.109	0.897	1.091	0.868
6	25.4	5.80	19.0	22.5	1.026	0.801	0.957	0.790
7	25.4	5.76	19.0	25.4	0.953	0.824	0.588	0.510
8	25.5	5.63	17.5	35.0	1.292	1.256	0.962	0.934
9	25.4	5.56	20.0	38.0	1.316	1.300	1.251	1.265
10	25.5	5.42	18.0	34.5	1.335	1.263	1.212	1.229
11	25.5	5.43						
12	25.4	5.52	17.5	34.0	1.310	1.342	1.289	1.378
13	25.4	5.60	16.0	30.0	1.340	1.223	1.323	1.261
14	25.4	5.66	16.7	33.7	1.487	1.343	1.332	1.178
15	25.5	5.69	17.0	30.5	1.431	1.318	1.185	1.134
16	25.5	5.72	17.3	31.8	1.583	1.601	1.423	1.478
17	25.4	5.73	17.0	30.5	1.652	1.644	1.332	1.342
18	25.4	5.71	16.1	29.0	1.601	1.460	1.265	1.149
19	25.4	5.56	16.1	28.3	1.568	1.284	1.335	1.090
20	25.5	5.45	14.9	24.1	1.349	1.383	0.964	0.957
Avg.					1.317	1.400	1.154	1.071
Std.Dev.					0.201	0.247	0.196	0.234

Geometrical dimensions, crack extensions, and G_{IIc} data for the carbon/epoxy specimens are summarized in Table 2.4. The crack extensions during precracking and fracture testing are similar to those for glass/epoxy, Table 2.3, and both beam theory and compliance calibration produced similar toughness values. As for glass/epoxy, Table 2.3,

the beam theory method results in less standard deviation. Also similar to the glass/epoxy composite, the non-precracked specimen produced higher toughness values, about 9 % on average.

Table 2.4: Carbon/epoxy ENF specimen dimensions, crack extensions, and G_{IIc} data.

Specimen #	b (mm)	2h (mm)	Crack Extension, mm		GIIc, kJ/m²			
			Precrack	Fracture	Non-Precracked		Precracked	
					BT	CC	BT	CC
1	25.4	4.30					0.602	0.002
2	25.5	4.41	16.0				0.559	0.004
3	25.4	4.46	15.3	29.9			0.609	0.619
4	25.4	4.47	16.0	23.0			0.698	0.601
5	25.3	4.49	11.4	26.0			0.495	0.397
6	25.4	4.49	15.6	28.0			0.567	0.570
7	25.4	4.46	20.7	31.0			0.655	0.601
8	25.4	4.38	12.5	19.5			0.649	0.572
9	25.4	4.43	11.5	20.6			0.580	0.519
10	25.5	4.47	17.0	20.6			0.654	0.631
11	25.4	4.37	16.5	25.5			0.604	0.606
12	25.5	4.38	16.4	31.5			0.579	0.537
13	25.5	4.35	17.1	25.2			0.576	0.568
14	25.4	4.43	18.0	27.0			0.586	0.583
15	25.4	4.49	17.0	24.0			0.579	0.562
16	25.4	4.48	15.5	27.4	0.678	0.643	0.662	0.621
17	25.5	4.51	17.3	26.5	0.691	0.642	0.613	0.556
18	25.5	4.49	17.3	26.0	0.694	0.653	0.603	0.567
19	25.4	4.41	18.5	30.5	0.725	0.711	0.607	0.597
20	25.4	4.35	19.4	28.2	0.781	0.792	0.771	0.772
Avg.					0.714	0.688	0.612	0.524
Std.Dev.					0.0414	0.0648	0.0580	0.190

The G_{IIc} results in Tables 2.3 and 2.4 show that the toughness of carbon/epoxy is significantly less at an average of 0.635 kJ/m^2 compared to glass/epoxy with an average toughness of 1.24 kJ/m^2. This difference cannot be attributed to the matrix since it is the same in both composites. Inspection of the fracture surfaces in a scanning electron microscope revealed that the glass/epoxy fractured in the matrix, at some distance from the fiber surfaces, while the carbon/epoxy composite fractured predominantly at the

fiber/matrix interface, see Figure 2.10. Further, the glass/epoxy composite displayed more extensive deformation of the matrix in the form of "hackles", see Figure 2.10b.

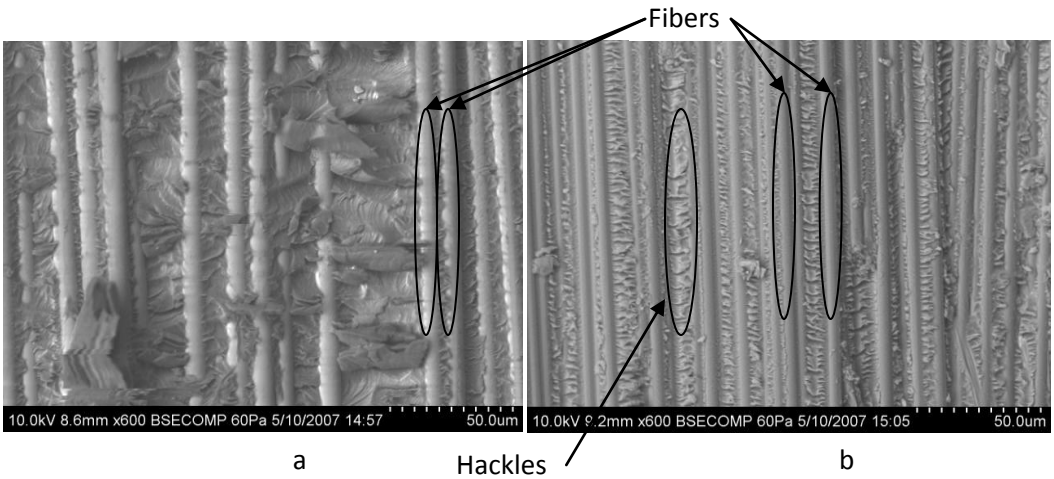

Figure 2.10: Fracture surfaces of ENF test specimens. a) glass/epoxy b) carbon/epoxy

The mode II fracture toughness data determined herein may be compared to previously measured G_{IIc} data for glass/epoxy and carbon/epoxy. The comparison should be viewed as a reference rather than quantitatively since in some cases the specific fibers and matrix materials are different. Baizeau et al. (29) examined an E-glass/epoxy composite, while Li et al. (19) examined carbon/epoxy. Hansen and Martin (30) measured G_{IIc} for the same glass and carbon fibers and same epoxy matrix as considered here using the 4ENF test.

Table 2.5 presents a summary of the toughness data discussed, and G_{IIIc} data. The volume fractions of the composites studied herein are quite low (.53 and .54 for glass/epoxy and carbon/epoxy, respectively). Generally, a low fiber volume fraction will increase the delamination toughness, so this factor cannot explain the lower toughness values determined here. The fracture surface, shown in Figure 2.10b, displays quite a

large amount of bare carbon fibers, indicating interface failure. The difference in toughness may possibly be related to different sizing of the fibers, changing the failure from the matrix to the interface.

Table 2.5: Mode II average delamination toughness values for glass/epoxy and carbon/epoxy.

Composite	V_f	G_{IIc} kJ/m^2
E-glass/epoxy[(29)]	.53	1.79±.21
Carbon/epoxy[(21)]	.60	1.06±.10
S-glass/epoxy[(30), (25)]	.60	1.76±.03
Carbon/epoxy[(30), (25)]	.60	1.33±.30
S-glass/epoxy*	.53	1.15±.22
Carbon/epoxy*	.54	.612±.06

*) current study. G_{IIc} (max) determined using beam theory and precracked specimen.

2.3 ECT Testing Using One-Point and Two-Point Test Fixtures

The one-point and two-point mode III ECT test fixtures shown in Figures 1.10 and 1.12 were used. The test data determined from the one-point and two-point ECT tests will be reduced using various data reduction methods explained below.

The compliance of the one-point ECT specimen was derived from plate theory by Lee (19),

$$C = \frac{w^2 l}{4(b-(1-2s)a)(D_{66})_I} \tag{2.7}$$

where, the dimensions *w, l, a*, and *b* are defined in Figure 1.12, and the parameter s is defined by,

$$s = \frac{(D_{66})_{II}}{(D_{66})_I} \tag{2.8}$$

where $(D_{66})_I$ and $(D_{66})_{II}$ are the twisting stiffnesses of the complete laminate and the half laminate. This ratio is s=1/8 for a homogeneous plate, but differs from 1/8 for a laminated panel.

For an uncracked one-point ECT specimen (a=0), the plate theory compliance becomes

$$C = \frac{w^2 l}{4b(D_{66})_I} \tag{2.9}$$

The energy release rate, G, for the one-point ECT specimen is determined from the definition of G, Eq. (1.4), by differentiation of the compliance expression (2.7) with respect to crack area $A=La$.

$$G = \frac{P^2 C(1-2s)}{2lb\left(1-(1-2s)^{a}/_{b}\right)} \tag{2.10}$$

For the two-point ECT specimen the compliance expression, Eq. (2.7), is modified to,

$$C = \frac{w^2 l}{16(b-(1-2s)a)(D_{66})_I} \tag{2.11}$$

where the factor of 16 in the denominator occurs because the total applied load P is shared between two corners and the deflection under the load in the two-point test is one-fourth of that in the one-point configuration. Hence, the compliance of the two-point ECT specimen is 4 times less than that of the one-point. The compliance of an uncracked two-point ECT specimen is,

$$C = \frac{w^2 l}{16b(D_{66})_I} \tag{2.12}$$

The strain energy release rate for the two-point test is obtained from the definition of G (Eq. (1.4)) which yields

$$G = \frac{P^2}{2l}\frac{d}{da}\left(\frac{w^2 l}{16(b-(1-2s)a)(D_{66})_I}\right) =$$

$$\frac{P^2}{2l}\left(\frac{w^2 l(1-2s)}{16(b-(1-2s)a)(D_{66})_I(b-(1-2s)a)}\right) =$$

$$\frac{P^2}{2l}\left(\frac{C(1-2s)}{(b-(1-2s)a)}\right) \qquad (2.13)$$

Hence, G for the two-point ECT configuration is identical to that of the one-point ECT configuration, Eq. (2.10).

The ECT test procedure (31) stipulates fracture testing of a series of ECT specimens with a range of crack lengths *(a/b)* and recording of the load vs. displacement response *(P-δ)*. From the *P-δ* graphs it is possible to determine the compliance, *C=δ/P*. The compliance expressions, Eqs. (2.7) and (2.11) indicate an inverse relationship between compliance and crack length, *a*. To achieve a linear plot the compliance is inverted and a graph of stiffness, *1/C,* vs. *a/b* is then constructed, see the schematic shown Figure 2.11.

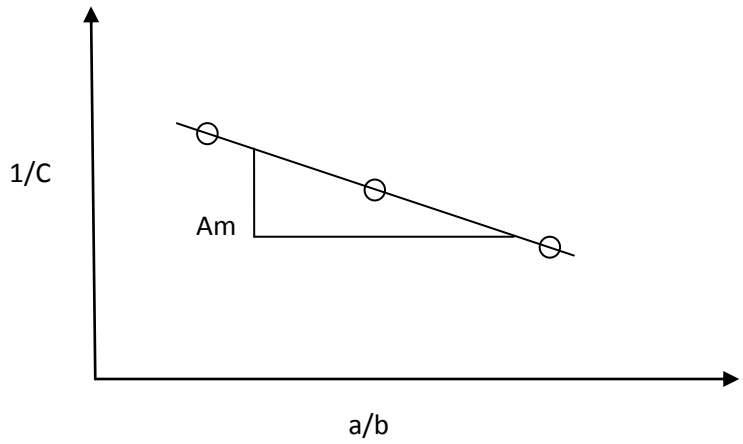

Figure 2.11: ECT compliance calibration curve.

This graph may be described by

$$\frac{1}{C} = A\left(1 - m\frac{a}{b}\right) \tag{2.14}$$

where *Am* is the slope of the line (*1/C*) vs. (*a/b*), and *A* is the stiffness at zero crack length *(a=0)(uncracked ECT specimen).* The ASTM draft standard document (31) stipulates five crack lengths for the determination of the normalized slope, m, using linear regression. Once *m* has been established, the energy release rate is determined using Eq. (2.10) after replacing *(1-2s)* with the compliance calibration term *m*

$$G = \frac{mCP^2}{2b\left(1 - m\frac{a}{b}\right)} \tag{2.15}$$

2.3.1 Modification of ECT CPT Data Reduction Methods

It should be pointed out that the CPT analysis is strictly valid only for panels with no *x-overhang*. Similarly, the crack length, *a*, includes the *y*-overhang at the cracked edge. The plate theory Equations (2.15) and (2.11) for ECT specimen compliance take into account overhang in the *y* direction only, and use of the total specimen width, *b,* which includes *y-overhang* extending beyond the loaded width, *w*, see Figure 2.12. These equations thus account for *y-overhang* assuming a linear decrease of compliance with increase of *y-overhang*. The increase of plate stiffness due to overhang, however, does not, as will be shown, scale linearly with overhang length as inherently assumed in the derivations of Eqs. (2.7) and (2.11).

Emphasis on the loading area rather than the external plate dimensions in the data reduction may possibly improve the accuracy of the determination of G. Hence, modified data reduction procedures were examined. The original methods of data reduction for are based on the plate dimensions *l* and *b* and the crack length, *a*, as defined in Figure 2.12. While the dimension *l* represents the loaded length of the panel, the dimension *b* includes *y-overhang* of the panel that extends beyond the primary loading rectangle defined by *l* and *w* in Figure 2.12.

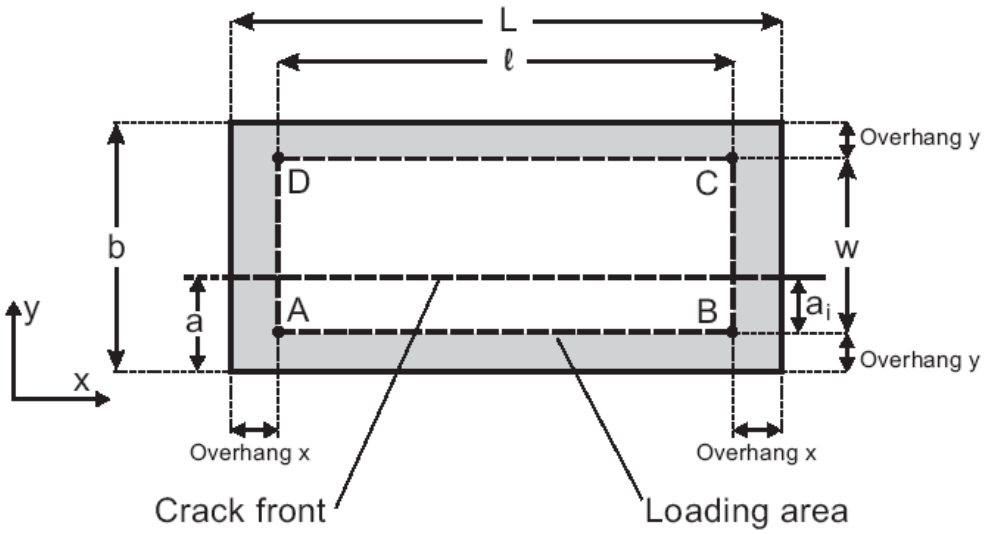

Figure 2.12: ECT specimen dimensions.

The original method is modified by changing b to w and a to a_i, where a_i is the length of the crack with reference to the loading line AB in Figure 2.12. The one-point CPT compliance equation Eq. (2.7) when modified becomes the following,

$$C = \frac{w^2 l}{4(l-(1-2s)a_i)(D_{66})_I} \tag{2.16a}$$

The modified CPT energy release equation Eq. (2.10) becomes

$$G = \frac{P^2 C(1-2s)}{2lw\left(1-(1-2s)\left({}^{a_i}/_{w}\right)\right)} \tag{2.16b}$$

The modified compliance calibration and energy release rate equations are obtained from Eqs. (2.14) and (2.15) for the one and two-point test methods,

$$\frac{1}{C} = A\left[1 - m\left(a_i / w\right)\right] \tag{2.17}$$

$$G = \frac{mCP^2}{2lw\left[1 - m(a_i / w)\right]} \tag{2.18}$$

Another method for determining G is direct application of the classical experimental compliance calibration (CECC) method where the compliance as a function of crack area is fitted with a polynomial. Figure 2.13 shows examples of fitted compliance curves for a series of carbon/epoxy specimens loaded in a two-point ECT fixture. The crack area in this case was calculated from the specimen length, L, and the length of the crack inside the loading area, a_i; $A=La_i$. The compliance data can be fitted with a second or third order polynomial,

$$C = c_0 + c_1 A \quad + c_2 A^2 \tag{2.19a}$$

$$C = c_0 + c_1 A \quad + cA^2 + cA^3 \tag{2.19b}$$

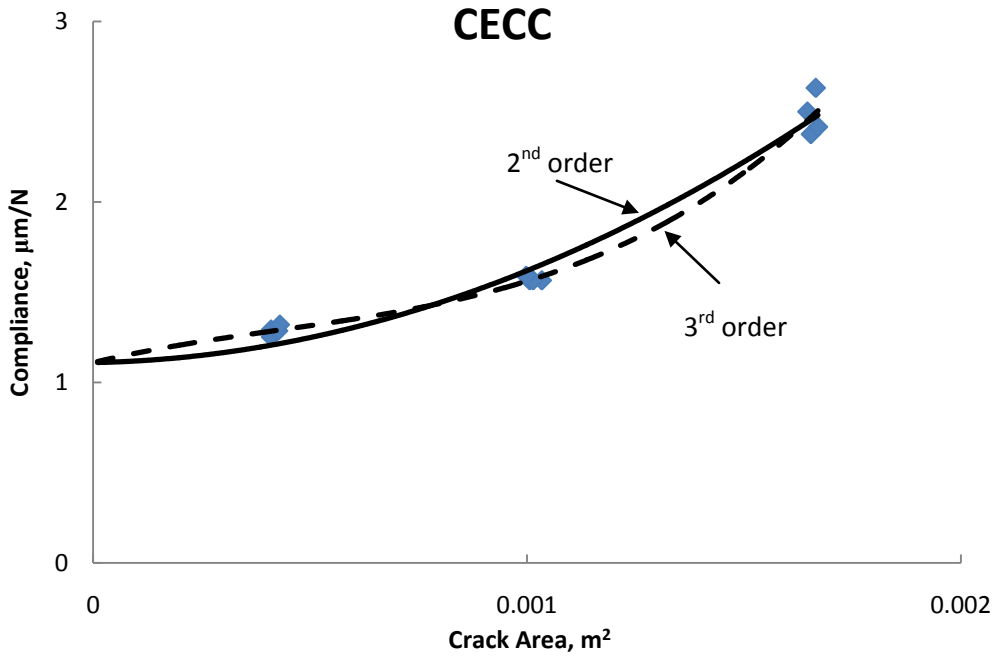

Figure 2.13: Experimental compliance calibration (two-point carbon/epoxy).

The 2nd and 3rd order polynomials produce similar fits over the range of crack areas considered. The 3rd order polynomial fits the data a little closer than the 2nd order, but tends to curve down in a fashion uncharacteristic of the ECT specimen as small crack areas are approached. The 2nd order fit produces a more realistic curve but may curve upwards as small crack areas are approached. Improved accuracy of the polynomial fit demands compliance data at zero crack area. This can be determined by experimentally testing uncracked specimens. Another option is to use Lee's compliance calibration method by plotting *1/C* vs. a_i/w as shown in Figure 2.11. The straight line can then be extrapolated to zero crack length to yield *C=C(0).*

Once the proper fit to the compliance data has been obtained, the definition of energy release rate, Eq. (1.4), is applied to Eqs. (2.19) to obtain

$$G = \frac{P^2}{2}(c_1 + 2c_2 A) \quad (2.20a)$$

$$G = \frac{P^2}{2}(c_1 + 2c_2 A + 3c_3 A^2) \quad (2.20b)$$

Test Procedure

The one and two-point ECT test fixtures, Figures 1.10 and 1.12, employ a series of studs to align the ECT specimen in the fixture for proper loading. The fixture of choice was first placed on the base of the testing frame. For the one-point fixture the loading and clamping pins were retracted and loosened, respectively, to allow the specimen to be placed in the fixture. When inserting the ECT specimen into the two-point ECT fixture, the two loading pins were retracted to a degree that allowed for the specimen to slip underneath. Once the ECT specimen was inserted in the fixture, the specimen was firmly butted up against the three centering studs. Then the clamping pin was tightened if the one-point specimen is used. The pin should only be tightened enough to touch and hold the specimen in place. The fixture was then moved just out of the way of the cross head and the cross head lowered below the contact point of the fixture. The cross head was raised to enable the fixture to slide under the contact plate on the cross head. Following this the fixture was centered relative to the contact point. The contact plate of the machine was slowly lowered no faster than .085 mm/sec until a load of about 40N was reached. Then the specimen was slowly unloaded to zero load and the cross head was stopped. A LVDT was then attached to the machine and zeroed. In this case the LVDT measures the displacement of the cross head.

The tested ECT specimens utilized the same carbon/epoxy and glass/epoxy characterized experimentally in Section 2.1. The carbon/epoxy lay-up was: $(90/0/(\pm 45/\mp 45)_2/0/90)_s$. This 24 ply lay-up yields approximately a 4.5mm thick carbon/epoxy specimen. The glass/epoxy lay-up was: $(90/0/(\pm 45/\mp 45)_3/0/90)_s$. The 32 ply glass/epoxy ECT specimens were approximately 7mm thick. Four crack lengths were used for each of four ECT specimen sets, *a*=0, 8, 15, and 23mm. Figure 1.15 shows the one and two-point specimen dimensions and geometry. The white rectangular regions indicate the loading areas which are the same for both specimen. The shaded areas represent the overhang regions, and those are larger on the short sides of the two-point ECT specimen. The one-point ECT specimen is 89 mm long whereas the length of the two-point specimen is 108 mm. All *y-overhangs* were 3mm while the one-point specimen employs unsymmetrical 3mm and 9mm *x-overhangs* and the two-point uses symmetric 16mm *x-overhangs*, see Figure 1.15.

Fracture testing was conducted at a crosshead rate of .042 mm/sec. The data recording system sampled load and displacement about 5 times a second. The loading continued till fracture occurred and then both the cross head and the data acquisition system were stopped. Fracture was not always audible but could be noted from a large drop in the load or a gradual unloading when the crack propagated. The specimen was then unloaded and removed from the fixture.

2.3.2 ECT Test Results

The load-displacement (P-δ) curves of all specimens were recorded. Figures 2.14 and 2.15 show examples of P-δ curves for carbon/epoxy and glass/epoxy ECT specimens with 8mm crack lengths (a=8mm) tested in the two-point fixture. From each P-δ curve stiffness and the critical load at failure were determined. The load, P_{NL}, at onset of nonlinear behavior of the load-displacement curve was also evaluated (determined by eye).

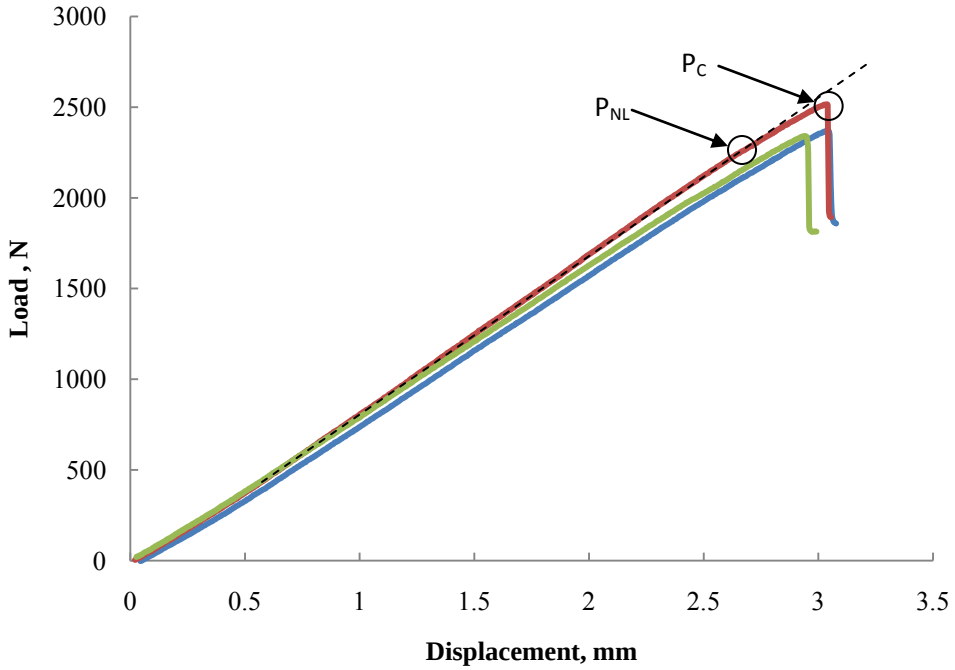

Figure 2.14: P-δ curves for three carbon/epoxy two-point ECT specimens with a crack length a=8mm.

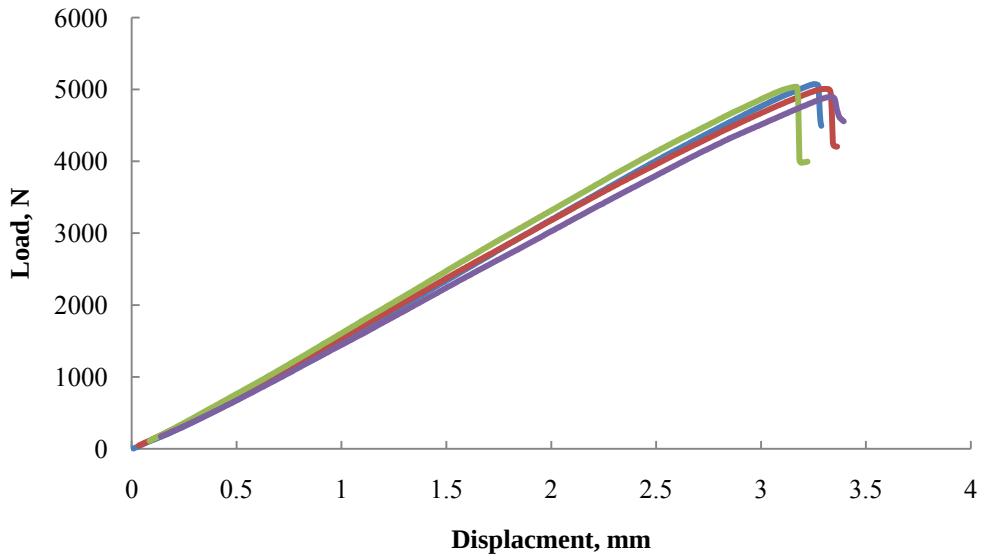

Figure 2.15: *P*-δ curves for four glass/epoxy two-point ECT specimens with a crack length a=8mm.

Both the carbon/epoxy and glass/epoxy response curves are repeatable and consistent. Fracture loads for the glass/epoxy ECT specimens, Figure 2.15, are about twice those for the carbon/epoxy ECT specimen depicted in Figure 2.14. A typical curve has a linear response through 90 or 95% of the load application then becomes slightly nonlinear for the remaining portion until the point of fracture, which is instantaneous and distinct. This desirable response happens regularly at shorter crack lengths. Longer crack lengths lead to more stable crack growths and larger nonlinear portions of the curve. This makes the point of fracture less distinct and determination of the critical load more uncertain.

Once the testing was completed the raw data was analyzed and necessary parameters for determining fracture toughness and describing the specimens reaction to load were undertaken. Important parameters include compliance, stiffness, critical load, and nonlinear load. Nonlinear load was the load at which the *P*-δ curve deterred from

linear, P_{NL}. Results are listed for the four testing series of the carbon/epoxy and glass/epoxy composites in Tables 2.6 – 2.9.

Table 2.6: Test data from carbon/epoxy one-point ECT specimens.

specimen	a (mm)	a/b	Compliance (μm/N)	1/C (N/μm)	Max Load (kN)	NL Load (kN)
1-1	0	0	3.58	0.070	2.233	2.233
1-2	0	0	3.32	0.075	2.311	2.311
1-3	0	0	3.3	0.076	1.995	1.995
1-4	7.62	0.2	5.536	0.045	1.010	1.005
1-5	7.62	0.2	5.384	0.046	1.031	1.000
1-6	7.62	0.2	5.984	0.042	.948	.947
1-7	15.2	0.4	8.008	0.031	.747	.747
1-8	15.2	0.4	8.104	0.031	.725	.680
1-9	15.2	0.4	7.54	0.033	.755	.685
1-10	22.9	0.6	11.764	0.021	.568	.550
1-11	22.9	0.6	10.752	0.023	.605	.600
1-12	22.9	0.6	11.172	0.022	.595	.575

Table 2.7: Test data from carbon/epoxy two-point ECT specimens.

specimen	a (mm)	a/b	Compliance (μm/N)	1/C (N/μm)	Max Load (kN)	NL Load (kN)
2-1	0	0	0.974	1.027	4.59	4.59
2-2	0	0	0.953	1.049	4.00	4.00
2-3	0	0	0.976	1.025	4.00	4.00
2-4	7.6	0.2	1.211	0.826	2.37	2.00
2-5	7.6	0.2	1.147	0.872	2.52	2.25
2-6	7.6	0.2	1.208	0.828	2.34	2.00
2-7	15.2	0.4	1.527	0.655	1.95	1.70
2-8	15.2	0.4	1.522	0.657	1.93	1.78
2-9	15.2	0.4	1.548	0.646	1.95	1.73
2-10	22.9	0.6	2.128	0.470	1.56	1.31
2-11	22.9	0.6	2.208	0.453	1.45	1.31
2-12	22.9	0.6	2.119	0.472	1.59	1.22

Table 2.8: Test data from glass/epoxy one-point ECT specimens.

specimen	a (mm)	a/b	Compliance (μm/N)	1/C (N/μm)	Max Load (kN)	NL Load (kN)
3-1	0	0	1.876	0.533	4.62	4.62
3-2	0	0	1.712	0.584	5.18	5.18
3-3	0	0	1.748	0.572		
3-4	7.6	0.2	2.192	0.456	2.76	2.48
3-5	7.6	0.2	2.16	0.463	2.67	2.60
3-6	7.6	0.2	2.316	0.432	2.83	2.65
3-7	15.2	0.4	2.712	0.369	2.32	2.06
3-8	15.2	0.4	2.596	0.385	2.12	1.90
3-9	15.2	0.4	2.84	0.352	1.92	1.70
3-10	22.9	0.6	3.788	0.264	1.59	1.33
3-11	22.9	0.6	3.676	0.272	1.63	1.35
3-12	22.9	0.6	3.548	0.282	1.69	1.40

Table 2.9: Test data from glass/epoxy two-point ECT specimens.

specimen	a (mm)	a/b	Compliance (μm/N)	1/C (N/μm)	Max Load (kN)	NL Load (kN)
4-1	0.0	0	0.543	1.842	8.80	8.80
4-2	0.0	0	0.547	1.827	8.35	8.35
4-3	0.0	0	0.543	1.843	8.85	8.85
4-4	0.0	0	0.552	1.810	8.82	8.82
4-5	7.6	0.2	0.593	1.687	5.07	4.40
4-6	7.6	0.2	0.609	1.642	5.01	4.00
4-7	7.6	0.2	0.584	1.712	5.04	4.00
4-8	7.6	0.2	0.633	1.581	4.89	4.20
4-9	15.2	0.4	0.766	1.305	4.03	3.50
4-10	15.2	0.4	0.767	1.303	4.07	3.50
4-11	15.2	0.4	0.771	1.297	4.04	3.25
4-12	15.2	0.4	0.793	1.261	4.06	3.33
4-13	22.9	0.6	0.964	1.037	3.49	3.00
4-14	22.9	0.6	1.005	0.995	3.55	3.00
4-15	22.9	0.6	0.974	1.027	3.57	3.03
4-16	22.86	0.6	1.020	0.980	3.42	2.75

In all cases the compliance of the specimen increased and the critical load decreased as the crack length was increased. The glass/epoxy specimens are stiffer than the carbon/epoxy because of the additional layers in the glass/epoxy lay-up as the glass fiber is not as stiff as the carbon fiber and the matrix is identical. Data are consistent and repeatable. Most specimens identically prepared show very consistent critical load data. Nonlinear data show more scatter but the point of nonlinearity is not distinctly clear and there is also human error involved with the determination of the nonlinear point. The magnitude of nonlinear load, P_{NL}, as a percentage of critical load, P_c, for the one-point glass/epoxy decreases with increasing crack length. For a crack length increase from 8 to 23mm, the P_{NL} percentage decreased from 94 to 83%. For the glass/epoxy two-point test, however, changes in crack length did not significantly influence the nonlinear load

percentage which was about 83%. The carbon/epoxy specimen tested in the one and two-point fixtures showed very similar trends. There were cases of ply splitting in the one-point carbon/epoxy and glass/epoxy specimens. Ply splitting is difficult to determine for ECT specimens loaded just to the onset of failure, because the crack growth can be very small. Wedging a specimen apart after testing, if not done to a small degree, will likely, in itself cause ply splitting. The one-point carbon/epoxy and glass/epoxy specimens with the shortest crack length a=8mm showed signs of ply splitting. The two-point ECT specimens did not show indication of ply splitting for any crack length examined.

2.3.3 Mode III Fracture Toughness

Mode III fracture toughness, G_{IIIc}, was determined using various data reduction methods. The first, referred to as compliance calibration (CC) method, utilizes Eqs. (2.14), (2.15), (2.17), and (2.18). The second method is a direct application of the classical plate theory (CPT) method Eq. (2.10) and (2.16b) and the third is the classical experimental compliance calibration (CECC) method, Eq. (2.20a).

According to the original compliance calibration method, the stiffnesses (1/C) for each test specimen is plotted vs. normalized crack length, a/b as indicated in Figure 2.16.

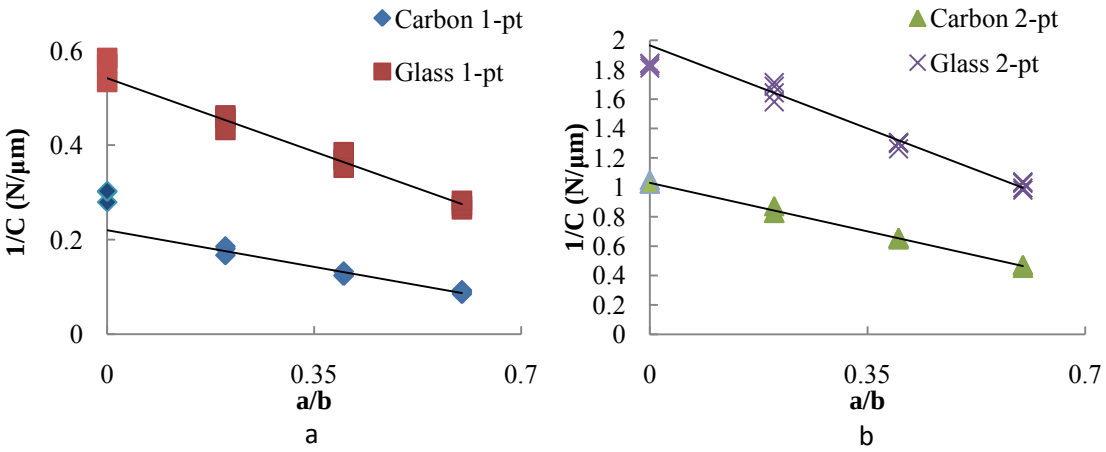

Figure 2.16: Stiffness of carbon/epoxy and glass/epoxy ECT specimens vs. crack length (original data reduction methods). a) one-point b) two-point.

As is to be expected the stiffness (*1/C*) of the tested specimens diminishes as the precrack length is increased. The glass/epoxy specimens are stiffer than the carbon/epoxy. This is because the glass/epoxy specimens are thicker (36 plies vs. 24 plies). As discussed earlier the two-point ECT configuration is four times stiffer than the one-point configuration.

The modified method shows stiffness plotted vs. the modified crack length ratio, a_i/w. Plots constructed according to the modified method are shown in Figure 2.17.

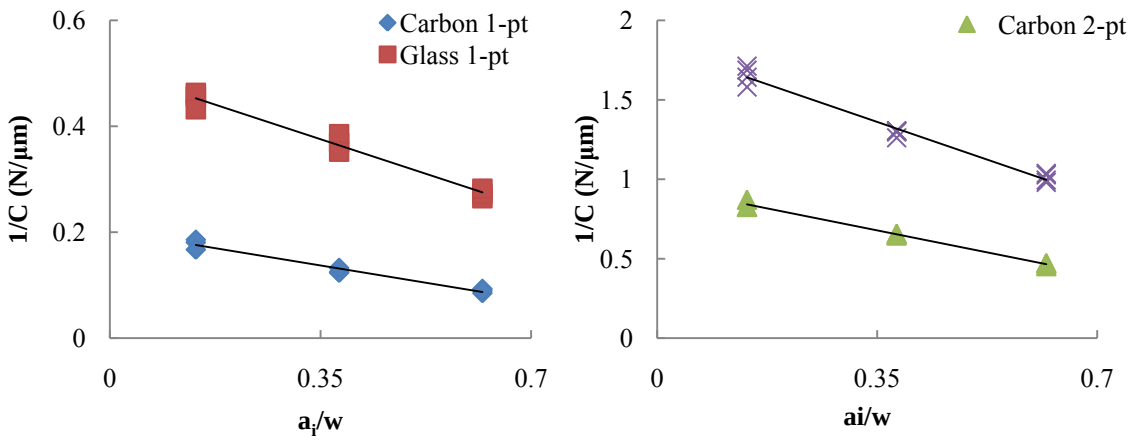

Figure 2.17: Stiffness of carbon/epoxy and glass/epoxy ECT specimens vs. Modified crack length (modified data reduction methods). a) one-point b) two-point.

From the stiffness plots in Figure 2.16 and 2.17, the *A* and *m* values needed for G_{IIIc} determination, Eqs. (2.15) and (2.18), were determined. Results are displayed in Table 2.10.

Table 2.10: Compliance calibration slopes and intercepts.

	Standard		Modified	
	A	m	A	m
Carbon 1-pt	0.88	1.008	0.809	0.921
Carbon 2-pt	1.003	0.915	0.955	0.829
Glass 1-pt	2.166	0.82	2.024	0.737
Glass 2-pt	1.965	0.822	1.835	0.739

The fracture toughness, G_{IIIc}, was determined based on the data in Tables 2.8 – 2.9 using the standard and modified versions of the CPT, CC, and CECC data reduction methods, Eqs. ((2.10), (2.15), (2.16), (2.17), and(2.20a)) Fracture toughness results based on maximum load are listed in Tables 2.11 – 2.14.

Table 2.11: G_{IIIc} for carbon/epoxy one-point ECT specimens.

specimen	a/b	ai/w	Max G_{III}^{CC} kJ/m^2	Max G_{III}^{CPT} kJ/m^2	Mod Max G_{III}^{CC} kJ/m^2	Mod Max G_{III}^{CPT} kJ/m^2	G_{IIIc} CECC kJ/m^2
1-4	0.2	0.143	1.230	0.989	1.230	1.113	1.279
1-5	0.2	0.143	1.248	1.004	1.249	1.130	1.334
1-6	0.2	0.143	1.171	0.942	1.172	1.060	1.126
1-7	0.4	0.381	1.301	0.982	1.302	1.142	1.150
1-8	0.4	0.381	1.243	0.938	1.243	1.090	1.085
1-9	0.4	0.381	1.254	0.947	1.255	1.100	1.177
1-10	0.6	0.619	1.669	1.120	1.670	1.378	0.926
1-11	0.6	0.619	1.730	1.161	1.732	1.429	1.050
1-12	0.6	0.619	1.740	1.168	1.741	1.437	1.017

Table 2.12: G_{IIIc} for carbon/epoxy two-point ECT specimen.

specimen	a/b	ai/w	Max G_{III}^{CC} kJ/m^2	Max G_{III}^{CPT} kJ/m^2	Mod Max G_{III}^{CC} kJ/m^2	Mod Max G_{III}^{CPT} kJ/m^2	G_{IIIc} CECC kJ/m^2
2-4	0.2	0.143	1.316	1.193	1.316	1.343	0.704
2-5	0.2	0.143	1.404	1.273	1.405	1.433	0.794
2-6	0.2	0.143	1.280	1.160	1.280	1.306	0.687
2-7	0.4	0.381	1.441	1.273	1.442	1.480	1.108
2-8	0.4	0.381	1.407	1.242	1.407	1.444	1.085
2-9	0.4	0.381	1.463	1.292	1.463	1.502	1.109
2-10	0.6	0.619	1.818	1.533	1.819	1.886	1.121
2-11	0.6	0.619	1.622	1.367	1.622	1.683	0.964
2-12	0.6	0.619	1.879	1.584	1.880	1.950	1.164

Table 2.13: G_{IIIc} for glass/epoxy one-point ECT specimen.

specimen	a/b	ai/w	Max G_{III}^{CC} kJ/m^2	Max G_{III}^{CPT} kJ/m^2	Mod Max G_{III}^{CC} kJ/m^2	Mod Max G_{III}^{CPT} kJ/m^2	G_{IIIc} CECC kJ/m^2
3-4	0.2	0.143	2.828	2.722	2.828	3.074	1.478
3-5	0.2	0.143	2.620	2.521	2.619	2.848	1.390
3-6	0.2	0.143	3.139	3.021	3.138	3.412	1.554
3-7	0.4	0.381	3.077	2.935	3.077	3.418	2.875
3-8	0.4	0.381	2.449	2.335	2.448	2.720	2.387
3-9	0.4	0.381	2.196	2.094	2.195	2.439	1.957
3-10	0.6	0.619	2.654	2.494	2.653	3.057	2.194
3-11	0.6	0.619	2.715	2.551	2.714	3.128	2.312
3-12	0.6	0.619	2.814	2.643	2.813	3.241	2.484

Table 2.14: G_{IIIc} for glass/epoxy two-point ECT specimens.

specimen	a/b	ai/w	Max G_{III}^{CC} kJ/m^2	Max G_{III}^{CPT} kJ/m^2	Mod Max G_{III}^{CC} kJ/m^2	Mod Max G_{III}^{CPT} kJ/m^2	G_{IIIc} CECC kJ/m^2
4-5	0.2	0.143	2.584	2.481	2.585	2.803	2.286
4-6	0.2	0.143	2.593	2.490	2.594	2.813	2.233
4-7	0.2	0.143	2.517	2.417	2.518	2.730	2.260
4-8	0.2	0.143	2.569	2.467	2.570	2.787	2.130
4-9	0.4	0.381	2.626	2.498	2.628	2.909	1.903
4-10	0.4	0.381	2.687	2.555	2.688	2.976	1.944
4-11	0.4	0.381	2.664	2.533	2.665	2.950	1.918
4-12	0.4	0.381	2.768	2.632	2.769	3.066	1.938
4-13	0.6	0.619	3.287	3.077	3.289	3.773	1.774
4-14	0.6	0.619	3.551	3.324	3.553	4.075	1.838
4-15	0.6	0.619	3.465	3.244	3.467	3.977	1.852
4-16	0.6	0.619	3.338	3.127	3.342	3.834	1.703

Figure 2.17 shows graphs of G_{IIIc} vs. normalized crack length for carbon/epoxy determined using test data generated from the one and two-point fixtures and reduced using compliance calibration and CPT.

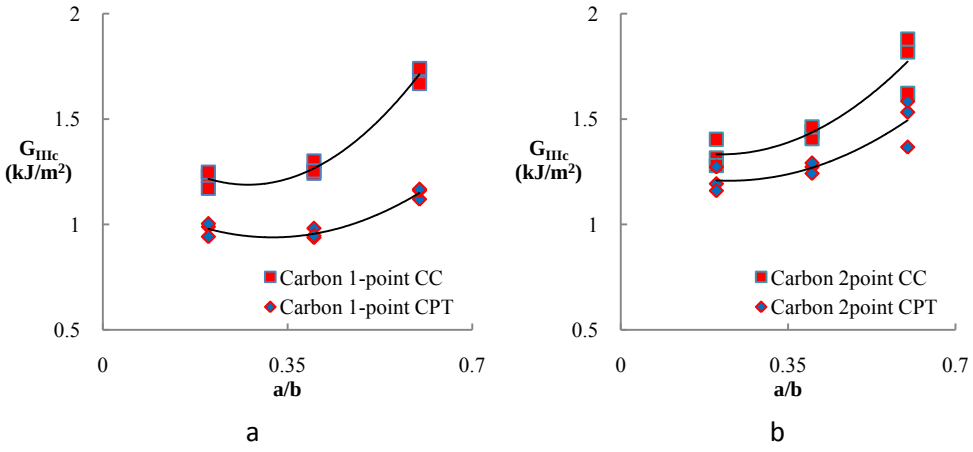

Figure 2.18: G_{IIIc} for carbon/epoxy one and two-point ECT specimens (standard methods). a) one-point b) two-point

There is not much scatter in the carbon/epoxy mode III fracture toughness data. The results for G_{IIIc} for a given material should ideally collapse to a single horizontal line,

since G_{IIIc} is considered a material property. The results in Figure 2.18 show, however, that G_{IIIc} increases with increasing crack length. The compliance calibration method produces higher G_{IIIc} values than the CPT method for both the one and two-point tests. G_{IIIc} curves for carbon/epoxy determined using the two-point method are more consistent, but slightly higher in magnitude than those determined using the one-point test.

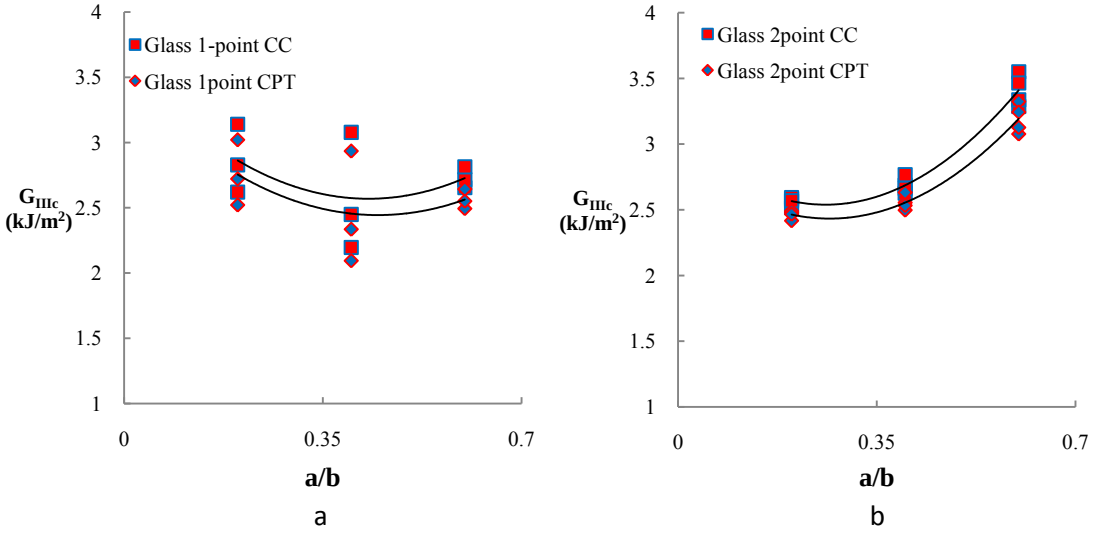

Figure 2.19: GIIIc for glass/epoxy ECT specimens (original method).
a) one-point b) two-point

G_{IIIc} results for glass/epoxy are shown in Figure 2.19. G_{IIIc} determined using the one-point test has a large amount of scatter at $a/b = 0.35$. This scatter could possibly be related to ply splitting. The two-point G_{IIIc} data, Figure 2.19b, shows much less scatter and clearer trends than the one-point data, Figure 2.19a. As will be discussed later, ply splitting in the two-point ECT specimen may be reduced by increasing the *x-overhang*. G_{IIIc} determined from the two-point test, however, show a very steep increase for the

longest crack length, see Figure 2.19b. As will be discussed later, this is likely to be attributed to the large overhang employed by two-point ECT specimen.

For comparison, G_{IIIc} data for carbon/epoxy and glass/epoxy two-point ECT specimens determined by Ratcliffe (25) are shown in Figure 2.20b. Radcliffe's data were reduced using the original compliance calibration data reduction method and a method denoted as the "LPT method", see (25).

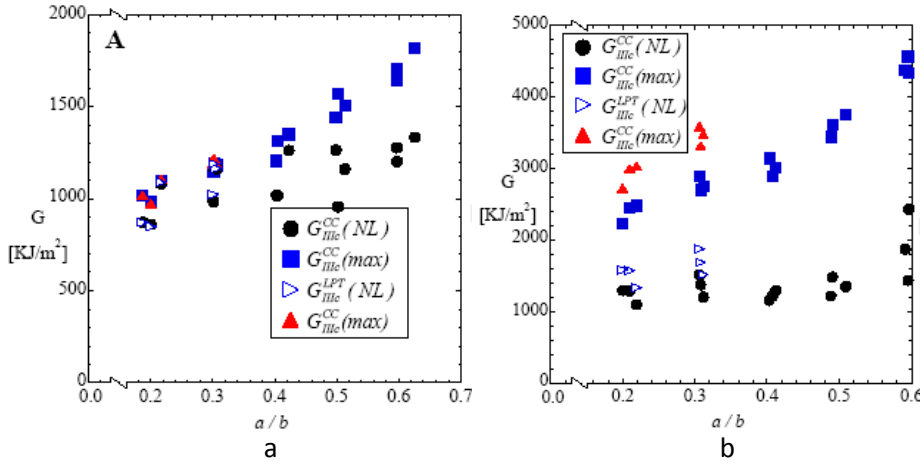

Figure 2.20: Mode III fracture toughness values determined by Ratcliffe (25). a) carbon/epoxy b) glass/epoxy (There is an error in the y-axis units. kJ/m^2 should be J/m^2)

Ratcliffe's carbon/epoxy G_{IIIc} (max) data are close to our two-point G_{IIIc} results shown in Figure 2.18b. Our glass/epoxy data in Figure 2.19b show more consistency over the range of crack lengths. However, our G_{IIIc} data increases more sharply with crack length, than those of Ratcliffe.

Application of the modified compliance calibration, CPT and CECC methods for the reduction of G_{IIIc}, for the carbon/epoxy ECT specimens yields the results shown in Figure 2.21.

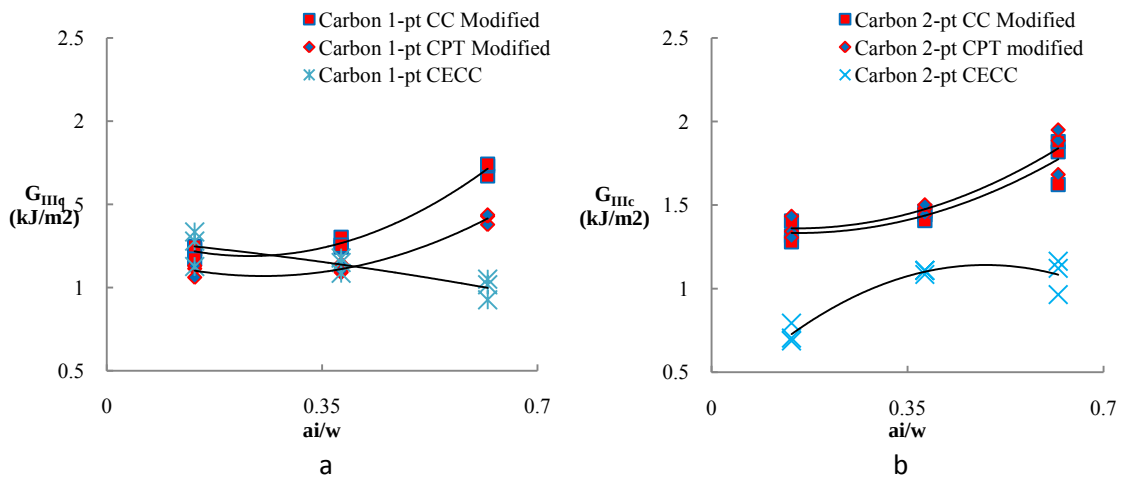

Figure 2.21: G_{IIIc} determined using the modified CPT and CC methods and the CECC method for carbon/epoxy. a) one-point b) two-point.

Although G_{IIIc} for the longest crack length is still high, the modified method produces G_{IIIc} data for carbon/epoxy that are much more consistent than the original data reduction method, see the results shown in

Figure 2.18. The CECC method, however, produces trends very different from the CC and CPT methods and leads to a decrease in G_{IIIc} at long crack lengths. The CECC method applied to the two-point carbon/epoxy data results in G_{IIIc} data far below those determined using the original and modified methods.

Mode III fracture toughness data for glass/epoxy are displayed in Figure 2.22. Determining G_{IIIc} using the modified compliance calibration method produces minor changes in the fracture toughness as compared to the original method. Application of the modified methods caused further separation of the CPT and CC results as compared to the original method, see Figure 2.19.

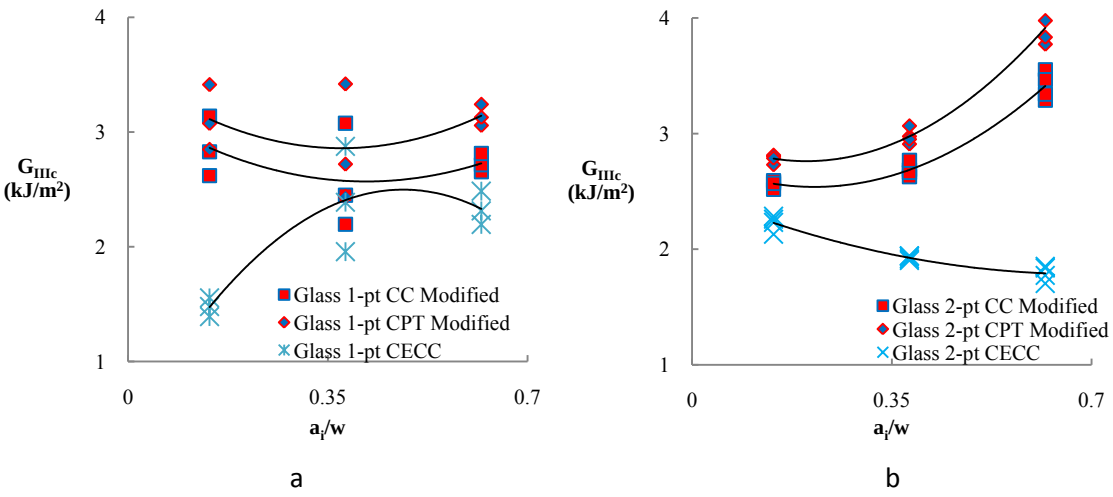

Figure 2.22: G_{IIIc}, determined by modified CPT and CC reductions and the CECC reduction method for glass/epoxy. a) one-point b) two-point

The CECC method does not yield consistent results. G_{IIIc} determined using the CECC is much less and the trends are very different from the other data reduction methods.

Based on the evaluation of the one-point and two-point ECT tests it appears as the two-point method produces more consistent results, but the elevation of G_{IIIc} at long crack lengths is not acceptable for the determination of a material property. This will be further discussed later in this chapter. The modified compliance calibration method is more fundamentally sound, but does not influence the G_{IIIc} results.

2.4 Influence of Overhang on ECT Test Results

In an effort to obtain an improved ECT mode III test procedure, a systematic experimental study of the influence of overhang has been conducted. Of particular concern were the influence of overhang on the compliance and energy release rate as well as the tendency for ply splitting. This experimental study also aims to identify the influence of overhang on stability of crack growth and ply-splitting. Another concern of

this analysis relates to the ability of plate theory to model the compliance and energy release rate of the ECT specimen. The series required the design and fabrication of a new twist test fixture. In Chapter 3 finite element modeling of the ECT specimens with different overhangs will be discussed.

2.4.1 Modified ECT fixture

The one-point and two-point ECT fixtures use supporting pins to aid in proper placement of the ECT specimen see Figures 1.10 and 1.12. These test configurations are designed for fixed specimen dimensions. ECT specimens with altered overhang thus cannot be tested because of the constraints of the current testing fixtures. A new testing fixture was made to allow for any sized ECT specimen to be tested.

The modified two-point fixture follows the same principle as the current two-point test shown in Figure 1.14. Similar to the previous two-point ECT test fixture, the modified fixture applies load to the ECT specimen through two pins and is therefore a two-point fixture. This fixture, however, incorporates two completely separate assemblies that never come in contact with each other, inspired by a recently developed sandwich twist fixture (32). The base of the fixture supports and stabilizes the two support pins, see Figure 2.22.

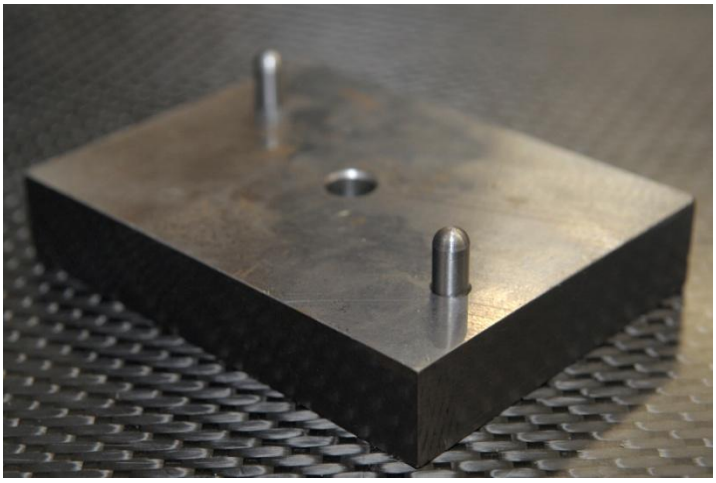

Figure 2.23: Base of modified two-point ECT fixture.

Notice that there are no centering/alignment pins because of the need for testing of specimens with differing overhang. A drawback is that the test specimen must be aligned and centered by eye. There is, however, a centering hole at the center of the base component. The centering hole enables alignment of the base with the testing machine and loading bar. A pin can be inserted in to the centering hole to center the base of the fixture at the center of the test machine. The second portion of the fixture is the loading bar shown in Figure 2.23. The loading bar partitions the applied load into the two rounded loading pins.

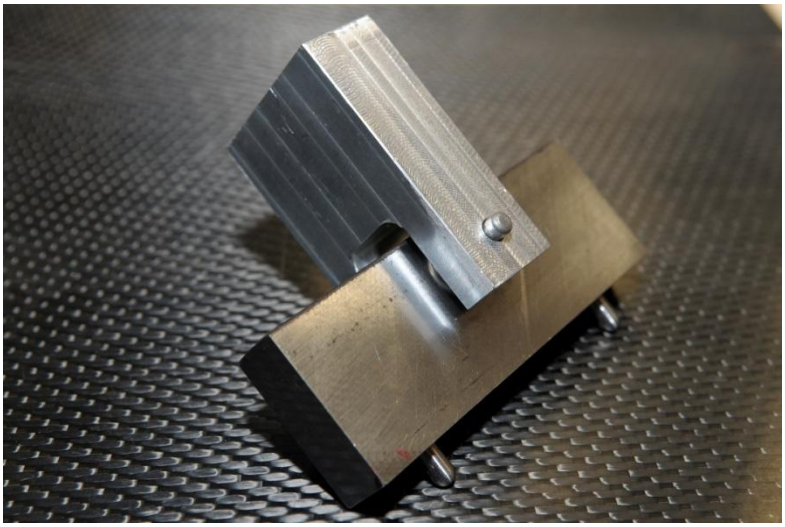

Figure 2.24: Loading bar for modified two-point ECT fixture.

The loading bar is allowed to pivot around its center, see Figure 2.24. A significant difference between the two-point fixture and the modified fixture is the lack of interaction between the base support and the loading pins in the modified fixture. The current one and two-point fixtures implement interaction between the base and loading pins to ensure proper positioning and alignment of the load/support points. This was avoided in the modified fixture to allow for unimpeded testing of ECT specimen with different overhang geometries. This fixture takes longer to set up because care must be taken to align the loading bar to the proper angle in order to produce the correct loading geometry. The complete two-point modified fixture mounted in the test machine is shown in Figure 2.25 and 2.26.

Figure 2.25: Modified two-point ECT testing fixture.

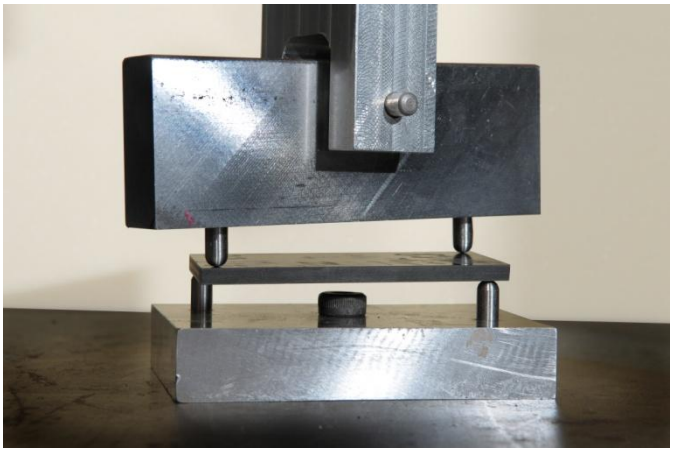

Figure 2.26: Modified two-point ECT fixture and specimen.

Note the centering pin is present and that the ECT specimen overhang is unconstrained.

2.4.2 Modified ECT Test Program and Results

A series of carbon/epoxy ECT specimens with various overhangs in the *x* and *y* directions as well as a range of crack lengths were tested. Table 2.15 is the test matrix for this testing series. The lay-up and thickness of the specimens are specified in Section 2.3, see also Figure 2.12.

Table 2.15: Experimental ECT overhang test program.

Case #	overhang *x* (mm)	overhang *y* (mm)	*a* (mm)	a_i *(mm)*	*L* (mm)	*b (mm)*
1	3	3	8	5	82	38
2	5	3	8	5	86	38
3	10	3	8	5	96	38
4	3	3	15	12	82	38
5	5	3	15	12	86	38
6	10	3	15	12	96	38
7	3	3	23	20	82	38
8	5	3	23	20	86	38
9	10	3	23	20	96	38
10	3	5	10	5	82	42
11	3	10	15	5	82	52
12	3	5	17	12	82	42
13	3	10	22	12	82	52
14	3	5	25	20	82	42
15	3	10	30	20	82	52

The overhang testing series investigates 15 cases, each with a unique combination *x/y* overhang and crack length. For each of these cases there are four replicate specimens. Examples of load - displacement curves for specimens with a constant (3x3) overhang at three crack lengths are shown in Figure 2.26.

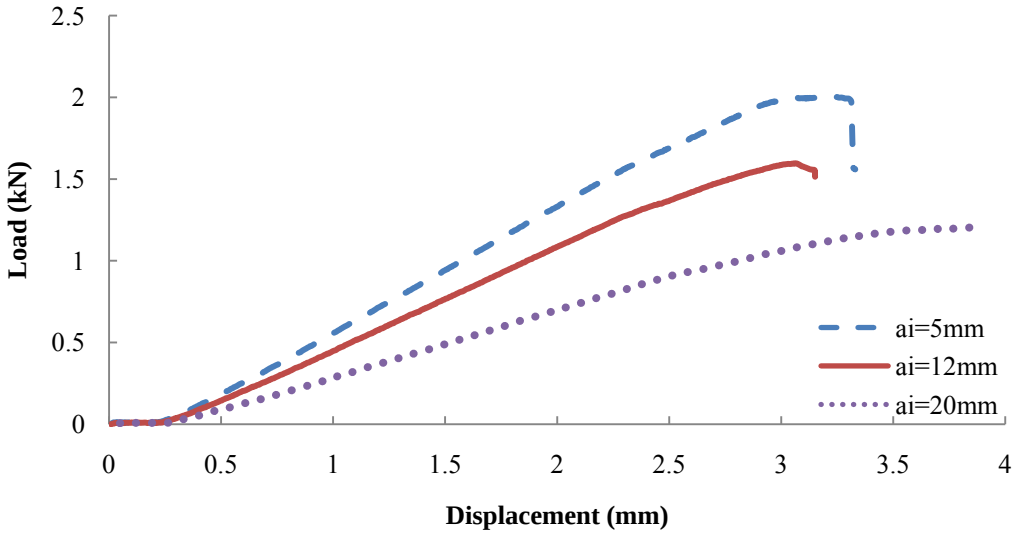

Figure 2.27: Overhang specimen 3x3 a_i=5, 12, and 20mm in the two-point modified ECT fixture.

The shortest crack length has the steepest curve and the highest fracture load, and displays a less stable crack growth with a sharp drop in load at fracture. There were also cases of ply splitting in the ECT specimens with the smallest overhang (3x3). Ply splitting was visually detected on the edges of the ECT specimen by crack propagation off the mid-plane. The ply splitting was detected in specimens with a_i= 5 and 12mm crack lengths with a 3x3mm overhang. The load – displacement results for the longest crack length displays an extended nonlinear portion prior to fracture which occurs in a stable manner without a distinct fracturing point. This effect becomes stronger when the *x-overhang* is increased, see Figure 2.28.

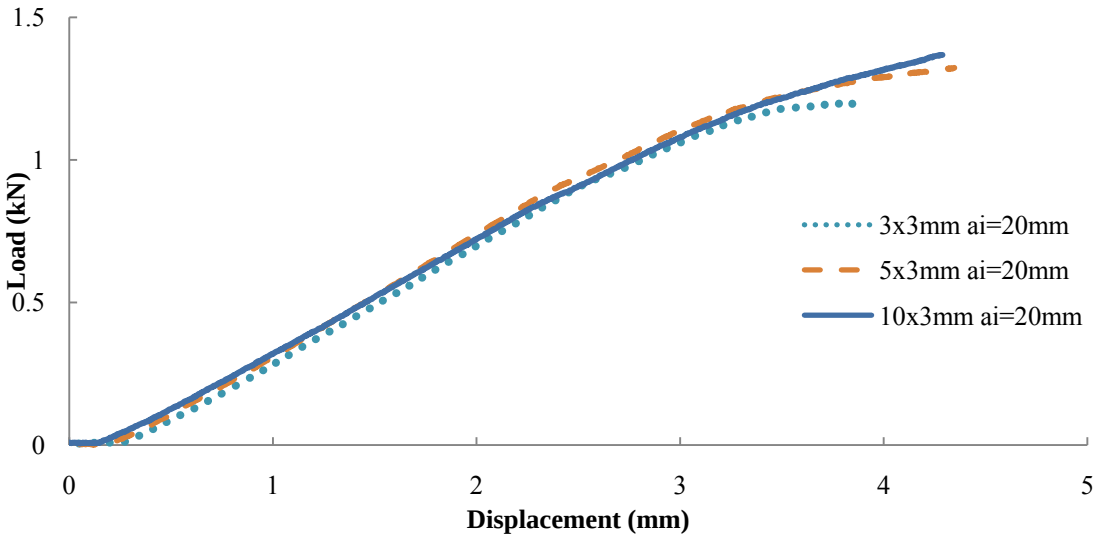

Figure 2.28: Load-displacement curves for various *x-overhangs*, a_i=20mm *oh*=3x3, 5x3, and 10x3.

The crack growth becomes so stable that there is no noticeable drop in load at fracture. The specimen with stable crack growth show a reduction of the slope of the load/displacement curve indicating slow crack propagation. In many cases the load/displacement curve begins to increase again after the drop and then the stiffness becomes larger than it was in the initial linear region. The highest load in the region of decreasing load/displacement slope is taken as the fracture load, P_c, in these cases.

Load-displacement curves for ECT specimen with various *y-overhangs* are shown in Figure 2.29.

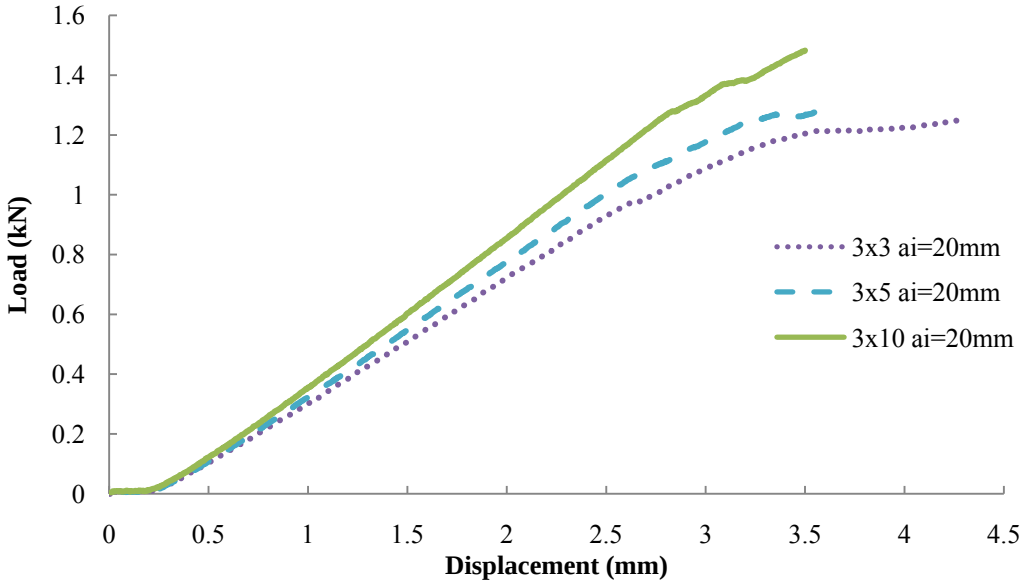

Figure 2.29: Load-displacement curves for carbon/epoxy ECT specimen with various *y-overhangs*, (3x3, 3x5, and 3x10) a_i=20mm.

Figure 2.29 shows that the compliance of the specimen is noticeably decreased when the *y-overhang* is increased. Similar to the trend caused by increased *x-overhang* (Figure 2.28), increased *y-overhang* (Figure 2.29) promotes more stable crack growth crack growth and less visual drops in load due to crack propagation.

Compliance (C) and mode III fracture toughness (G_{IIIc}) values reduced from the experimental overhang series are listed in Table 2.16. G_{IIIc} is reduced using the original and modified CC methods for both the load at which cracking was heard audibly and the critical load.

Table 2.16: Experimental ECT overhang specimen results.

Series	Oh-x (mm)	Oh-y (mm)	ai (mm)	a (mm)	MAX load (kN)	Audible Load (kN)	C. μm/N	G_{III}^{cc} org max kJ/m^2	G_{III}^{cc} org aud kJ/m^2	G_{III}^{cc} mod max kJ/m^2	G_{III}^{cc} mod aud kJ/m^2
1	3	3	05	8	1.900		1.29	0.959		0.961	0.000
2	3	3	12	15	1.607	1.271	1.57	1.074	0.674	1.077	0.674
3	3	3	20	23	1.200	0.897	2.48	1.340	0.774	1.352	0.778
4	5	3	5	8	2.027	1.582	1.24	1.063	0.638	1.055	0.634
5	5	3	12	15	1.667	1.205	1.60	1.159	0.612	1.146	0.606
6	5	3	20	23	1.310	0.877	2.35	1.593	0.718	1.546	0.696
7	10	3	5	8	2.028	1.470	1.21	1.086	0.572	1.092	0.573
8	10	3	12	15	1.632	1.216	1.58	1.197	0.668	1.202	0.670
9	10	3	20	23	1.348	0.846	2.46	1.978	0.775	1.985	0.780
10	3	5	5	10	2.013	1.538	1.27	0.988	0.584	0.993	0.586
11	3	5	12	17	1.519	1.433	1.54	0.857	0.754	0.863	0.758
12	3	5	20	25	1.291	1.026	2.25	1.245	0.796	1.262	0.803
13	3	10	5	15	2.335	1.975	1.11	1.163	0.831	1.198	0.856
14	3	10	12	22	1.967	1.615	1.41	0.681	0.905	0.702	0.936
15	3	10	20	30	1.665	1.259	2.00	1.948	1.117	2.040	1.174

A plot of compliance vs. the ratio of crack length, a_i, to loaded specimen width, *w*, is shown in Figure 2.27. The data sets are labeled by their overhang notation. The first number represents the symmetric overhang on both sides of the specimen along the *x-axis*, while the second number denotes the *y-overhang*, see Figure 2.12 for the definition of overhang and crack length.

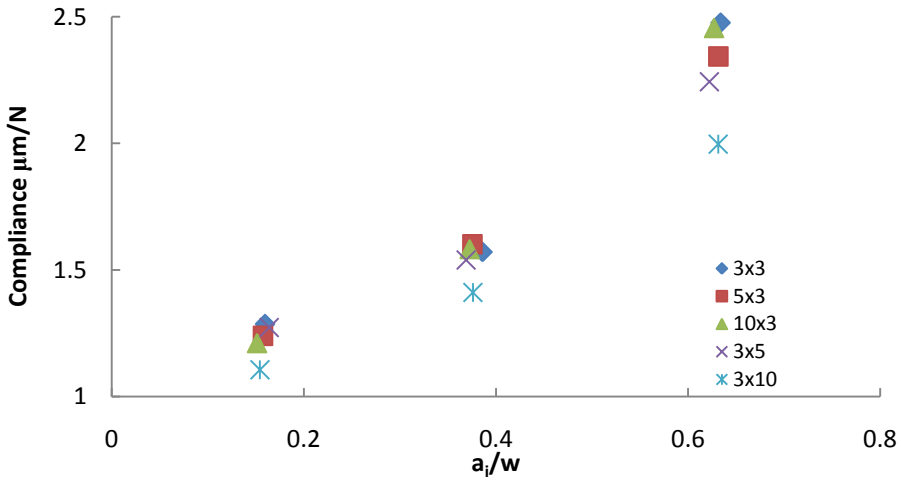

Figure 2.30: Compliance plot for carbon/epoxy ECT specimen based on averages of the experimental overhang series. The numbers represent *x* and *y-overhang* in mm.

Adding overhang tends to reduce the compliance, i.e., stiffen the ECT specimen. A specimen with a certain overhang in the *y* direction is clearly less compliant than a specimen with the same overhang in the *x* direction, compare for example the results for the 10x3 and 3x10 panels. This is attributed to the shorter length of the ECT specimen in the *y* direction, see Figure 2.12. Hence, a certain overhang added in the *y* direction represents a much larger percentage increase of the total area of the specimen than the same overhang added in the *x* direction.

The effect of *x-overhang* on compliance is displayed for the three crack lengths in Figure 2.31.

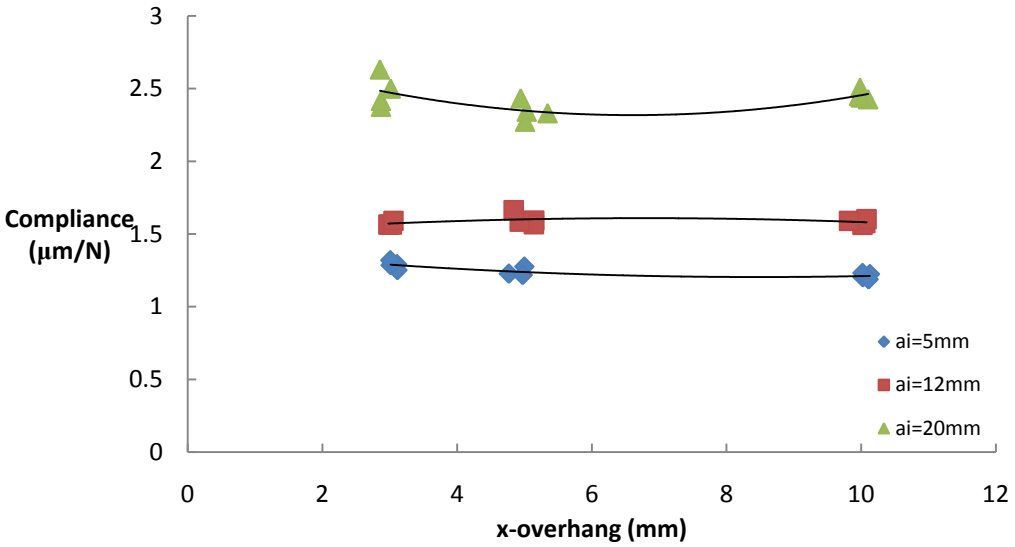

Figure 2.31: Compliance of carbon/epoxy ECT specimens as a function of *x-overhang*. (*y-overhang* = 3mm)

The *x-overhang* does not influence the compliance of the ECT specimen very much. The influence of *y-overhang* on compliance for panels with a constant *x-overhang* of 3mm is illustrated in Figure 2.32.

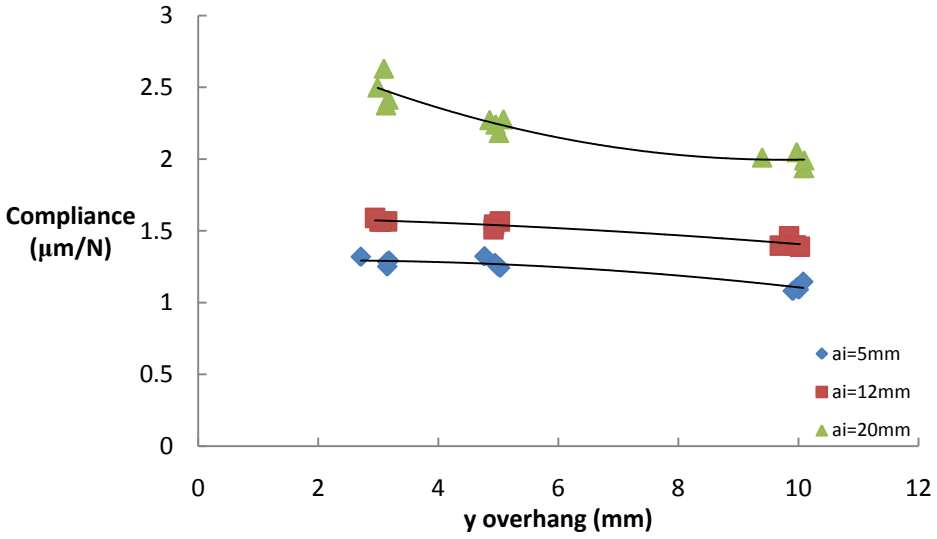

Figure 2.32: Compliance of carbon/epoxy ECT specimens as a function of *y-overhang*. (*x-overhang* = 3mm)

The results for three crack lengths (a_i=5, 12, and 20mm) shown in Figure 2.32 illustrate that the influence of *y-overhang* on compliance is most pronounced at longer crack lengths.

Fracture toughness, G_{IIIc} was reduced using the original and modified compliance calibration methods and presented in Table 2.16. G_{IIIc}, vs. crack length determined from the modified compliance calibration method is displayed in Figure 2.33.

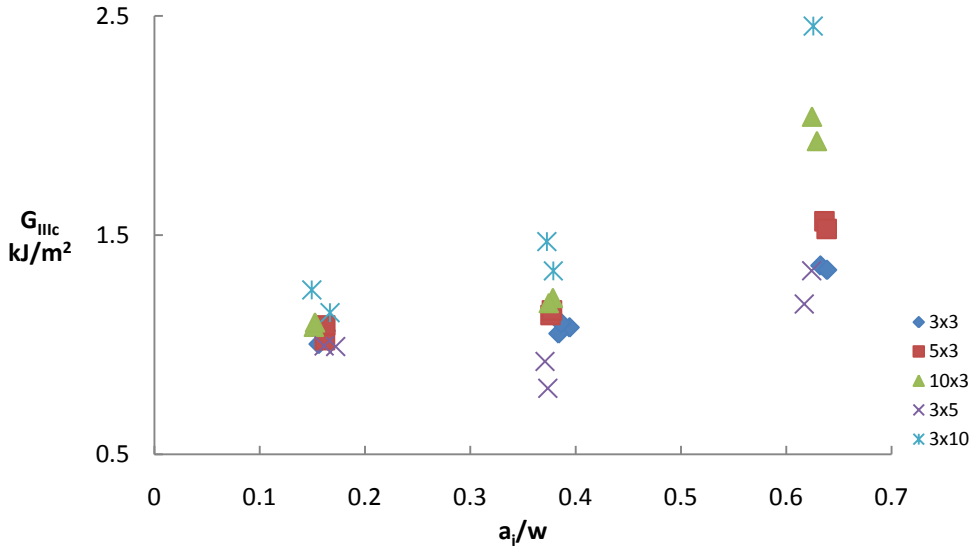

Figure 2.33: G_{IIIc} for carbon/epoxy ECT specimen overhang series. The numbers represent the *x-overhang* and *y-overhang* (mm).

The most consistent G_{IIIc} results are those for the minimum overhang, i.e. 3mm x 3mm. It is clear that in both cases the shortest crack length (a_i=5mm) delivers the most consistent results and the longest crack length (a_i=20mm) produces the least uniform results. As the overhang increases G_{IIIc} increases, similar to what was observed for the original ECT specimen geometries in Figure 2.18 and 2.21. Consequently, this set of test results indicate that the overhang should be kept at minimum, in this case 3x3 (mm).

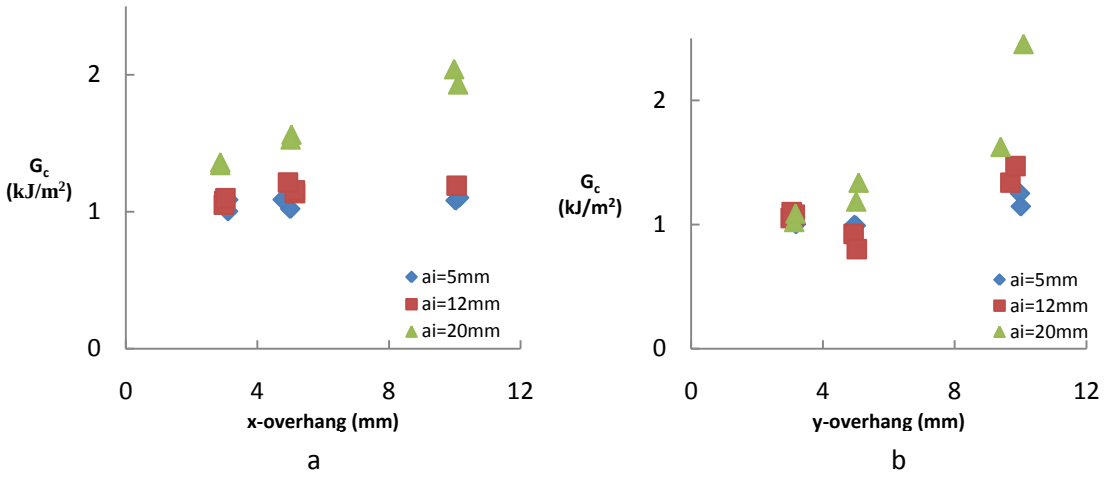

Figure 2.34: G_{IIIc} for carbon/epoxy ECT specimen as a function of overhang.
a) *y-overhang* = 3mm b) *x-overhang*=3mm

Figure 2.34 illustrates changes of G_{IIIc} with overhang when the crack length is constant. The most consistent results are obtained with the shortest *x* and *y-overhangs.*

Figure 2.35 displays G_{IIIc} vs. crack length for carbon/epoxy ECT specimens determined using the original two-point fixture (Section 2.3.3) and the modified ECT fixture at an overhang of 10x3 (mm). The specimens with an overhang of 10x3 (mm) produced similar G_{IIIc} values as the original two-point ECT specimens, see Section 2.3.3. The overhangs of these specimens are similar, see Figure 1.15.

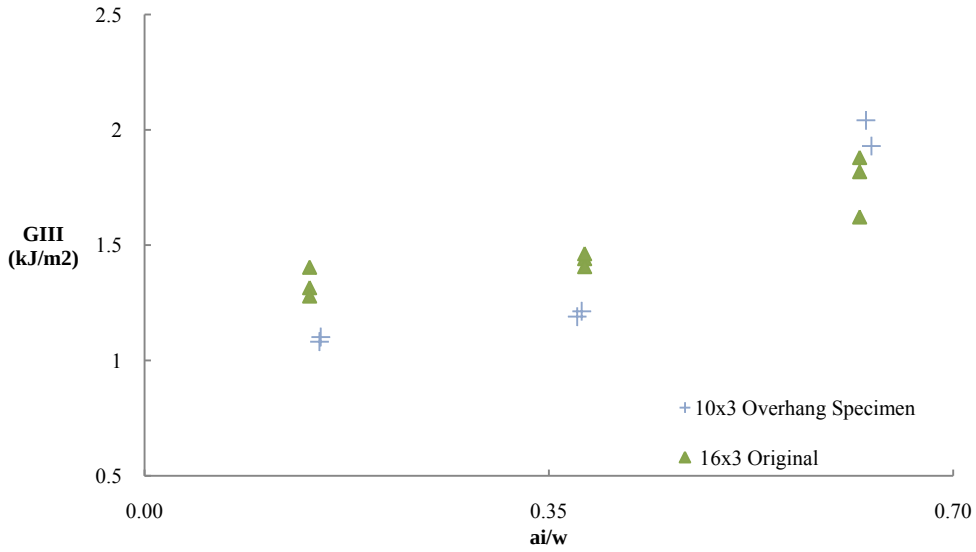

Figure 2.35: G_{IIIc} for carbon/epoxy determined using the original two-point (16x3) ECT two-point fixture and the modified10x3mm ECT overhang specimen and modified ECT fixture.

3 Analysis of the ECT Test Specimen

This chapter covers analysis done on the one and two-point ECT specimens. Classical plate theory analysis of uncracked ECT specimens is conducted to improve the basic understanding of the twist test. These analyses focus on the global compliance of the ECT test specimens. Following the plate theory analysis is a comprehensive finite element analysis (FEA). The FEA program begins modeling homogeneous uncracked plates progressing to modeling of ECT specimens consisting of many individual plies and a range of crack lengths and overhangs.

3.1 Classical Plate Theory Analysis of Plate in Pure Twist

Analysis of a plate under pure twist loading is performed. Classical plate theory (CPT), Timoshenko (33) and Jones (34), is here applied to a homogeneous, orthotropic ECT specimen without a precrack. The moment-curvature response in bending and twisting is governed by

$$\begin{bmatrix} M_x \\ M_y \\ M_{xy} \end{bmatrix} = \begin{bmatrix} D_{11} & D_{12} & 0 \\ D_{12} & D_{22} & 0 \\ 0 & 0 & D_{66} \end{bmatrix} \begin{bmatrix} \kappa_x \\ \kappa_y \\ \kappa_{xy} \end{bmatrix} \tag{3.1}$$

where M_x, M_y, and M_{xy} are the bending and twisting moments, and κ_x, κ_y, and κ_{xy} are the corresponding bending and twisting curvatures given in terms of the plate mid-plane deflection w_0 as,

$$\kappa_x = -\frac{\partial^2 w_0}{\partial x^2} \tag{3.2a}$$

$$\kappa_y = -\frac{\partial^2 w_0}{\partial y^2} \tag{3.2b}$$

$$\kappa_{xy} = -2\frac{\partial^2 w_0}{\partial x \partial y} \tag{3.2c}$$

D_{ij} are the bending and twisting stiffnesses defined in the classical laminated plate theory (34) as,

$$D_{11} = \frac{E_1 h^3}{12(1-\upsilon_{12}\upsilon_{21})} \tag{3.3a}$$

$$D_{12} = \frac{\upsilon_{12} E_2 h^3}{12(1-\upsilon_{12}\upsilon_{21})} \tag{3.3b}$$

$$D_{22} = \frac{E_2 h^3}{12(1-\upsilon_{12}\upsilon_{21})} \tag{3.3c}$$

$$D_{66} = \frac{G_{12} h^3}{12} \tag{3.3d}$$

where E_1 and E_2 are the principal Young's moduli, v_{12} and v_{21} are the major and minor in-plane Poisson ratios, and G_{12} is the in-plane shear modulus. h is the plate thickness.

3.1.1 Classical Plate Analysis of One-Point ECT Test

Consider the one-point loading of a homogeneous orthotropic plate shown in Figure 3.1.

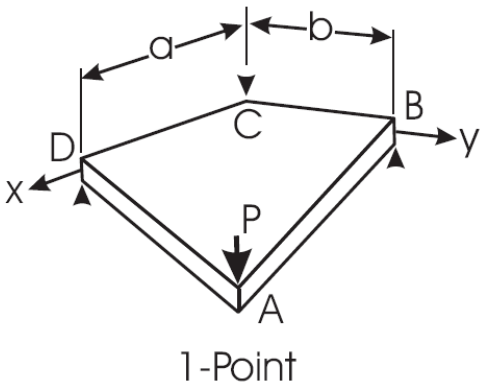

Figure 3.1: One-point loading of a homogeneous ECT specimen.

For the geometry and loading shown in Figure 3.1, $M_x = M_y = 0$, $M_{xy} = P/2$. With this Eq. (3.1) yields the twist curvature

$$\kappa_{xy} = \frac{P}{2D_{66}} \tag{3.4}$$

and zero bending curvatures; $\kappa_x = \kappa_y = 0$

Following the approach by Tsai (35), a general solution to the deflection of a panel under uniform bending and twisting moments is given by a 2nd degree polynomial in x and y,

$$w(x, y) = c_0 + c_1 x + c_2 y + c_3 x^2 + c_4 y^2 + c_5 xy \tag{3.5}$$

The parameters c_i (i=1, 2…5) are to be determined from the loading and boundary conditions. For the support point C in Figure 3.1 at $x = y = 0$, the deflection and slopes of the plate should vanish, i.e.,

$$w(0,0) = \frac{\partial w}{\partial x}(0,0) = \frac{\partial w}{\partial y}(0,0) = 0 \tag{3.6}$$

Substitution into Equation (3.5) yields, $c_0 = c_1 = c_2 = 0$. Furthermore, the curvatures are given by Eqs. (3.2). With $\kappa_x = \kappa_y = 0$, Eqs. (3.2) and (3.5) yield: $c_3=c_4=0$. The twist curvature, $\kappa_{xy,}$ is defined by Eq. (3.2c). This equation, combined with Eqs. (3.4) and (3.5) yields

$$c_5 = -\frac{\kappa_{xy}}{2} = -\frac{P}{4D_{66}} \tag{3.7}$$

Consequently, the deflection is given by,

$$w(x, y) = -\frac{Pxy}{4D_{66}} \tag{3.8}$$

The deflection, $\delta=|w|$ at the loaded corner A ($x=a$, $y=b$) is thus given by

$$\delta = \frac{Pab}{4D_{66}} \tag{3.9}$$

The compliance, $C=\delta/P$, the one-point configuration becomes

$$C = \frac{ab}{4D_{66}} \tag{3.10}$$

3.1.2 Two-Point ECT Test

Loading of the two-point ECT configuration is illustrated schematically in Figure 3.2.

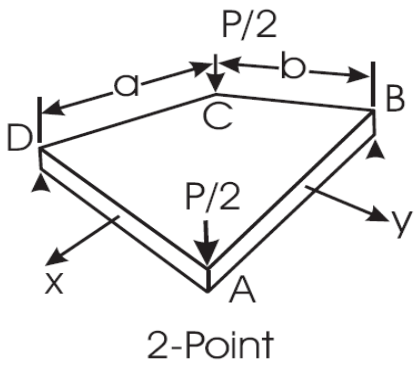

Figure 3.2: Two-point loading of homogeneous, uncracked ECT panel.

Notice here that the panel is loaded by two forces, each of magnitude *P/2*, and the origin of the coordinate system is placed at the center of the panel. The slopes $\frac{\partial w}{\partial x}$ and $\frac{\partial w}{\partial y}$ are zero at $x=y=0$ yielding $c_1 = c_2 = 0$ in Eq. (3.5). Further, the bending curvatures κ_x and κ_y vanish, yielding $c_3 = c_4 = 0$ in Eq. (3.5). Hence, only c_0 and c_5 remain in Eq. (3.5),

$$w = c_0 + c_5 xy \tag{3.11}$$

With $w\left(\frac{a}{2},-\frac{b}{2}\right) = 0$ (corner *D*), Eq. (3.11) yields,

$$c_0 = -\frac{c_5 ab}{4} \tag{3.12}$$

The twist curvature for the loading shown in Figure 3.2 is given by

$$\kappa_{xy} = \frac{P}{4D_{66}} \tag{3.13}$$

Combination of Eqs. (3.2c), (3.11), and (3.13) yields

$$c_5 = -\frac{P}{8D_{66}} \tag{3.14}$$

Substitution of Eq. (3.14) into (3.12) yields,

$$c_0 = -\frac{Pab}{32D_{66}} \tag{3.15}$$

The deflection, δ, under the corner loads is given by

$$\delta = \left| w\left(\frac{a}{2}, \frac{b}{2}\right)\right| = \frac{Pab}{16D_{66}} \tag{3.16}$$

Consequently, the specimen compliance for two-point loading is,

$$C = \frac{ab}{16D_{66}} \tag{3.17}$$

By comparison of Eqs. (3.10) and (3.17) it is noted that the ECT specimen loaded in the one-point configuration is four times more compliant than in the two-point configuration.

3.1.3 Coupling Effects

Coupling effects influence the curvatures of a plate. If coupling is strong, the deformed shape of the twist loaded specimen will deviate from the desired pure twist shape, i.e., $\varkappa_x \neq 0$, and $\varkappa_y \neq 0$. The CPT derivation of compliance presented in Section 3.1.1

assumes $D_{16}=D_{26}=0$ and hence does not consider the coupling effects. The ECT lay-up: $[0/0/\pm 45_s/\pm 45_s/0/90]$, includes off-axis ±45° plies to achieve sufficient torsional stiffness, but they also create nonzero bending/twisting coupling stiffnesses, D_{16} and D_{26}. The response of the panel is most clearly indicated by the compliance matrix $[d]=[D]^{-1}$. Specifically, the response of a laminate loaded by a twisting moment, M_{xy}, is described by,

$$\begin{bmatrix} \varkappa_x \\ \varkappa_y \\ \varkappa_{xy} \end{bmatrix} = \begin{bmatrix} d_{11} & d_{12} & d_{16} \\ d_{12} & d_{22} & d_{26} \\ d_{16} & d_{26} & d_{66} \end{bmatrix} \begin{bmatrix} 0 \\ 0 \\ M_{xy} \end{bmatrix} \tag{3.18}$$

The presence of d_{16} and d_{26} terms signifies that the panel will bend as well as twist, $(\varkappa_x \neq 0, and\ \varkappa_y \neq 0)$.

The bending and twist curvatures from X. Li (36) are

$$\varkappa_x = d_{16} M_{xy} \tag{3.19a}$$

$$\varkappa_y = d_{26} M_{xy} \tag{3.19b}$$

$$\varkappa_{xy} = d_{66} M_{xy} \tag{3.19c}$$

The ratios between bending and twisting curvatures become

$$\frac{\varkappa_x}{\varkappa_{xy}} = \frac{d_{16}}{d_{11}} \quad and \quad \frac{\varkappa_y}{\varkappa_{xy}} = \frac{d_{26}}{d_{11}} \tag{3.20a,b}$$

The ECT specimen employs a double symmetric lay-up. This means that if the full lay-up is split in half by delamination, each half remains symmetric. The symmetric half specimen lay-ups are also called sublaminates. The stiffness matrix, *[D]*, and

inverse stiffness matrix, *[d]*, for the full carbon/epoxy laminate, $[D]_I$ and $[d]_I$, with a lay-up of $[0/0/\pm 45_2/\pm 45_2/0/90]_s$ and the sublaminates, $[D]_{II}$ and $[d]_{II}$, as determined by PROMAL (37) are:

$$[D]_I = \begin{bmatrix} 338.2 & 128.5 & 5.621 \\ 128.5 & 366.3 & 5.621 \\ 5.621 & 5.621 & 139.8 \end{bmatrix} (Pa * m^3), [D]_{II} = \begin{bmatrix} 43.56 & 9.509 & 2.811 \\ 9.509 & 57.61 & 2.811 \\ 2.811 & 2.811 & 10.92 \end{bmatrix} (Pa * m^3)$$

$$[d]_I = \begin{bmatrix} 3.41E^{-3} & -1.20E^{-3} & -8.91E^{-5} \\ -1.20E^{-3} & 3.15E^{-3} & -7.86E^{-5} \\ -8.91E^{-5} & -7.86E^{-5} & 7.16E^{-3} \end{bmatrix} \left(\frac{1}{Pa} * m^3\right),$$

$$[d]_{II} = \begin{bmatrix} 2.41E^{-2} & -3.72E^{-3} & -5.25E^{-3} \\ -3.72E^{-3} & 1.82E^{-2} & -3.71E^{-3} \\ -5.25E^{-3} & -3.71E^{-3} & 9.39E^{-2} \end{bmatrix} \left(\frac{1}{Pa} * m^3\right)$$

The corresponding stiffness and compliance matrices for the glass/epoxy laminate with a lay-up of $[0/0/\pm 45_3/\pm 45_3/0/90]_s$ are:

$$[D]_I = \begin{bmatrix} 664.9 & 249.7 & 5.34 \\ 249.7 & 681.5 & 5.34 \\ 5.34 & 5.34 & 278.8 \end{bmatrix} (Pa * m^3), \ [D]_{II} = \begin{bmatrix} 86.13 & 25.07 & 2.670 \\ 25.07 & 94.44 & 2.670 \\ 2.670 & 2.670 & 28.71 \end{bmatrix} (Pa * m^3)$$

$$[d]_I = \begin{bmatrix} 1.74E^{-3} & -6.39E^{-4} & -2.12E^{-5} \\ -6.39E^{-4} & 1.70E^{-3} & -2.04E^{-5} \\ -2.12E^{-5} & -2.04E^{-5} & 3.59E^{-3} \end{bmatrix} \left(\frac{1}{Pa} * m^3\right),$$

$$[d]_{II} = \begin{bmatrix} 1.26E^{-2} & -3.32E^{-3} & -8.63E^{-3} \\ -3.32E^{-3} & 1.15E^{-2} & -7.60E^{-3} \\ -8.63E^{-3} & -7.60E^{-3} & 3.50E^{-2} \end{bmatrix} \left(\frac{1}{Pa} * m^3\right)$$

For the ECT specimens studied, the ratio bending/twisting curvature ratios for the full laminate and sublaminates are listed in Table 3.1.

Table 3.1: Bending/twisting curvature ratios for carbon/epoxy and glass/epoxy ECT specimen.

Material	κ_x/κ_{xy}	κ_y/κ_{xy}
C/E (Full)	-0.03	-0.02
C/E (sub)	-0.22	-0.15
G/E (Full)	-0.01	-0.01
G/E (sub)	-0.68	-0.60

The ratios in Table 3.1 represent the extent of the bending/twisting coupling. The full carbon/epoxy and glass/epoxy laminates have very little bending/twisting coupling. These characteristics apply to an ECT specimen with a short crack. As the crack is extended, the ECT specimen approaches two sublaminates stacked on each other. Table 3.1 dictates that the bending/twisting coupling start to influence the response of the ECT specimen as the crack length is increased for both materials. For the glass/epoxy sublaminates the magnitudes of the bending curvatures are quite large; 68% of the desired twisting curvature.

3.2 FEA Modeling of Uncracked Plates

The previous analysis of the ECT test assumes that the plate deforms to a pure twist shape by the action of the torque, M_{xy}, achieved by concentrated loads acting at the corners of the panel. The FEA study is performed to examine both homogeneous and uncracked ECT lay-ups under twist loading. Effects of overhang and indentation at the loading and support points will be considered.

Uncracked isotropic and unidirectional homogeneous carbon/epoxy panels are examined. Also a carbon/epoxy laminated panel with the same lay-up as the ECT panel was analyzed. The material properties of the modeled plates are listed below.

Isotropic: E=25GPa, ν=.3

Carbon/epoxy: E_1= 113GPa, E_2=E_3=7.3GPa, ν_{12}=ν_{13}=.36, ν_{23}=.44,

G_{12}=G_{13}=4.14GPa G_{23}=2.54GPa

Figure 3.3 illustrates the geometry of the analyzed panels. The loading area is defined by the rectangle *ABCD*. The overhang, represented by the shaded area in Figure 3.3 is the area outside of the rectangle defined by the four loading/support points. Finite element simulations were done to study the effects of overhang and material properties on square and rectangular uncracked plates. Dimensions of the plates listed in Table 3.2. Five plate configurations listed in Table 3.2 were analyzed. Four of the panels are square while one panel is rectangular. For each plate material symmetric overhangs of 0, 1, 2, and 5mm were considered.

Table 3.2: Plate geometries considered in twist analysis series.

loading/support pt. *a*x*b*(mm)	thickness, h (mm)	overhang (mm)	material prop.	D_{66} ($Pa*m^3$)
38x38	7	0,1,2,5	isotropic	274.8
38x76	7	0,1,2,5	isotropic	274.8
38x38	4.5	0,1,2,5	isotropic	73.0
38x38	4.5	0,1,2,5	unidirectional	31.4
38x38	4.5	0,1,2,5	laminate	139.8

The finite element analysis of the one-point twist test was conducted using the FE code ANSYS [7]. All models except those for the ECT lay-up utilized **SOLID 45** elements of dimensions 1x1x1(mm). For the ECT lay-up, **SHELL 99** elements were used. The **SHELL 99** element is a two-dimensional plate element with zero thickness (along the *z-axis)*.

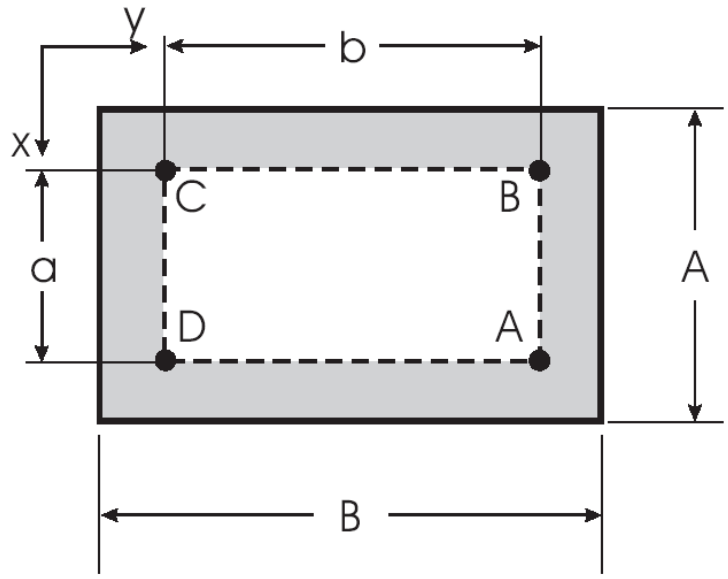

Figure 3.3: Uncracked twist specimen.

The boundary conditions and coordinate system can be explained using Figure 3.3. Corner *C* is a fixed in all directions. Corner *B* is only fixed in the *z-direction* and corner *D* is fixed in both the *z* and the *y-directions* to prevent rigid body rotations when loaded. To simulate one-point loading of the panel, corner A is given a displacement of 10mm in the negative *z-direction* (vertically downwards).

The twist curvature, $\varkappa_{xy}$, is defined from (33) in Eq. (3.22) as,

$$\varkappa_{xy} = -2\frac{\partial}{\partial y}\left(\frac{\partial w}{\partial x}\right) = -2\frac{\partial^2 w}{\partial x \partial y} \tag{3.20}$$

where *x* and *y* are the in-plane coordinates, Figure 3.4, and *w* is the out-of-plane (*z-direction*) displacement.

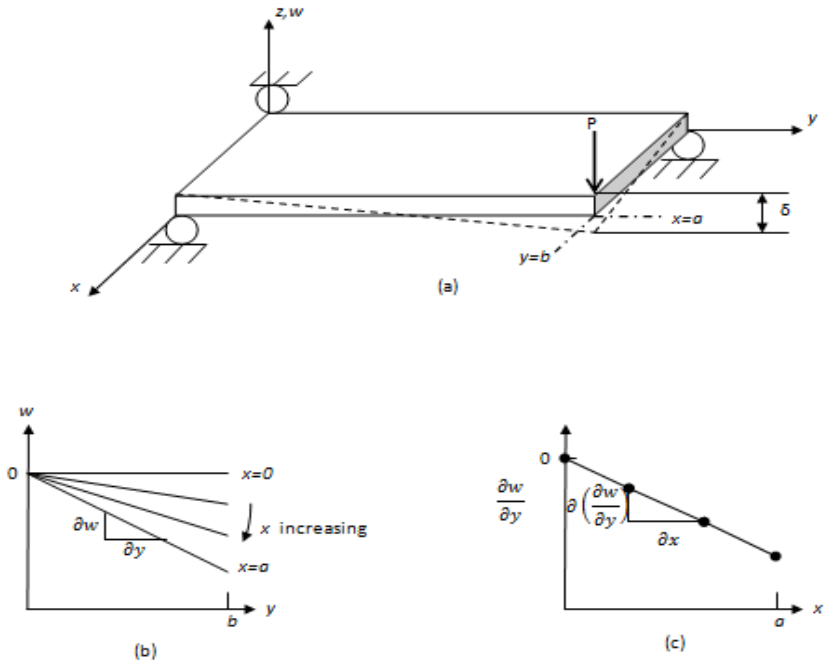

Figure 3.4: Illustration of twist curvature, $\varkappa_{xy}$, determination.

Figure 3.4a shows a panel of dimensions a x b (along the x and y axes) loaded in the one-point configuration at the corner $x=a$, $y=b$. The corner deflection, δ, is, $|w(a,b)|$. If the twist curvature, $\varkappa_{xy}$, is uniform, the panel will deform according to Eq. (3.8) as indicated in Figure 3.4b, which shows the deflection, w *vs.* x for various positions along the *x-axis*. For each position, $x=const$, the slope of the panel, $m_y = \frac{\partial w}{\partial y}$, may be determined as indicated in Figure 3.4b. Plotting the slope m_y vs. x, Figure 3.4c, enables determination of the slope, m_{yx}

$$m_{yx} = \frac{\partial}{\partial y}\left(\frac{\partial w}{\partial x}\right) \tag{3.21}$$

Comparison of Eqs. (3.22) and (3.23) reveals

$$\varkappa_{xy} = -2m_{yx} \tag{3.22}$$

Notice that it is equally valid to determine the twist curvature, by first plotting w vs. x for a set of y values and then finding the slope $\partial w/\partial x$, and plotting $\partial w/\partial x$ vs. y.

The twist curvature, $\varkappa_{xy}$, can also be calculated using plate theory (Eqs. (3.7) and (3.9)) from the deflection, δ, of the loaded corner, or the load, P, applied to the panel,

$$\varkappa_{xy} = \frac{2\delta}{ab} \tag{3.23a}$$

$$\varkappa_{xy} = \frac{P}{aD_{66}} \tag{3.23b}$$

Deviations from pure twisting may occur as a result of coupling effects (see Section 3.1.3), local indentation deformations at the support and load introduction regions, and perturbations due to overhang.

Finite element analysis was done on the panels listed in Table 3.2. In all cases a corner displacement, δ=10mm was applied (w=-10mm). Twist curvature was determined from nodal displacements (w) filtered to just include the nodes on the top surface of the panel. 10mm intervals of x are chosen and the out-of-plane displacement, w, is plotted along y. Figure 3.5 shows an example of such a plot for a 4.5mm thick isotropic square plate without overhang.

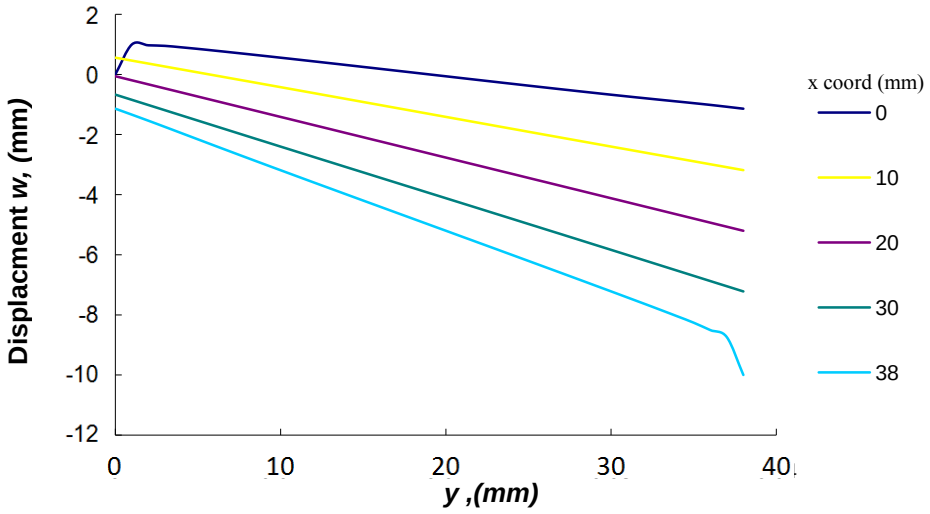

Figure 3.5: Out-of-plane displacement of the top surface at specific *x* locations for a 4.5mm thick isotropic square plate with no overhang.

The plate analysis presented in Section 3.1.1 predicts that the edges and any cross section cut perpendicular to the *x* and *y* axis of a twisted panel should remain straight, i.e. the plate edges will have no curvature. Figure 3.5 verifies such linearity of the deflection for x = 10, 20, and 30mm. For x=0 and 38mm, however, the linear trends are disturbed by the localized indentation deformation near the loading and support points, see Figure 3.5. Notice that the indentation at the support point, $x=y=0$ will allow positive displacements, w, of the top surface of the panel near the support location. At the loaded corner, $x=a$, $y=b$, the upper surface will indent causing the extra local displacement.

The slope of the linear region of each curve in Figure 3.5, $\frac{\partial w}{\partial y}$ was determined and plotted vs. x. Figure 3.6 shows that the slope is linear vs. x, in agreement with classical plate theory.

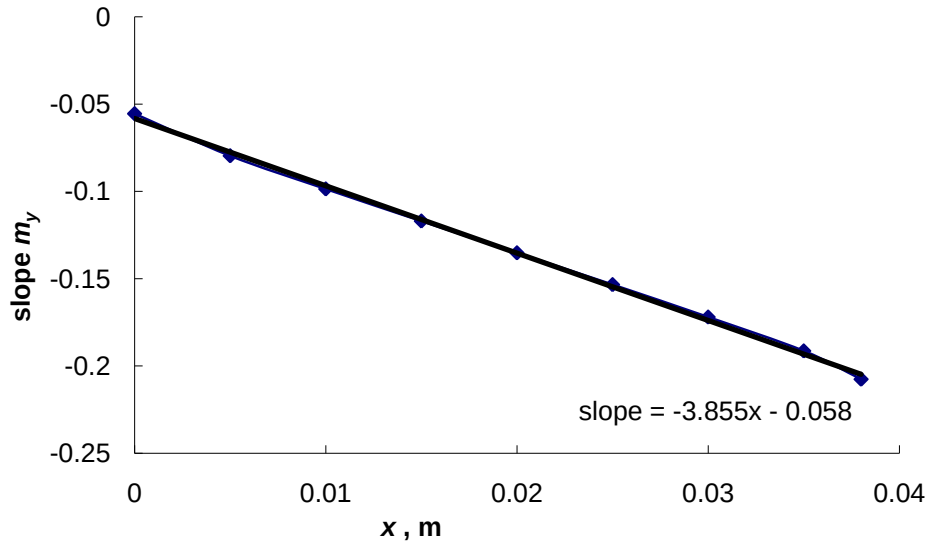

Figure 3.6: Slope m_y as a function of x for a 4.5mm thick isotropic square plate with no overhang.

The curvature, κ_{xy}, was evaluated according to Eqs. (3.22) and (3.23). Table 3.3 summarizes the twist curvature results for all analyzed panels determined using these three equations.

Table 3.3: Twist curvature results obtained from FEA and CPT.

a x *b* (mm)	h (mm)	material prop.	Method	Overhang (mm)				Displacement*
				0	1	2	5	
38x38	7	isotropic	FEA	7.7	11.5	11.6	11.0	13.9
			CPT**	6.1	10.2	11.4	14.0	
38x76	7	isotropic	FEA	4.8	6.2	6.3	6.2	6.9
			CPT**	4.1	5.7	6.2	7.5	
38x38	4.5	isotropic	FEA	11.3	13.1	13.2	12.7	13.9
			CPT**	9.8	12.7	13.9	17.4	
38x38	4.5	uni	FEA	10.9	12.9	12.9	12.4	13.9
			CPT**	9.2	12.2	13.5	16.8	
38x38	4.5	lay-up	FEA	13.7	12.8	12.9	12.4	13.9
			CPT**	9.5	10.2	11.3	14.4	

*)$\varkappa_{xy}$ calculated from Eq. (3.23a) using deflection, δ, and loading dimensions (*a and b*)
**) $\varkappa_{xy}$ calculated from Eq. (3.23b) using load, *P*, and twist curvature, D_{66}.

It is observed that the twist curvature reduced from the FEA is highly dependent on overhang, especially for the 7mm thick isotropic panels. The increasing tendency of $\varkappa_{xy}$ with increased overhang is partly due to the large indentation experienced for the panels without overhang. This will be discussed further in the next section. For panels with about 2mm overhang, all three equations produce similar curvatures indicating that the indentation is reduced due to the presence of overhang. For longer overhangs, however, the panel response becomes influenced by the overhang region, an effect not accounted for in the plate theory analysis.

3.2.1 Effects of Plate Properties on Compliance

The compliance of the plate was evaluated from the applied displacement and reaction load, $C=\delta/P$. For comparison, the compliance was also calculated from the analytical expression, Eq. (3.10). derived for a plate with no overhang. Results are listed in Table 3.4.

Table 3.4: Compliance (μm/N) of twist series determined from FEA and Eq. (3.10).

a x *b* (mm)	h (mm)	material prop.	Overhang (mm)				CPT*
			0	1	2	5	
38x38	7	isotropic	2.98	1.78	1.60	1.30	1.31
38x76	7	isotropic	4.47	3.17	2.92	2.44	2.63
38x38	4.5	isotropic	7.00	5.41	4.91	3.94	4.94
38x38	4.5	uni	17.4	13.01	11.8	9.44	11.5
38x38	4.5	lay-up	3.78	3.51	3.15	2.47	2.58

* Eq. (3.10)

The results in Table 3.4 show that the compliance calculated from FEA decreases with increasing overhang. This trend happens for two reasons. The first and initially most drastic effect of increasing the overhang is reduction of the indentation at the load

introduction and support points on the plate. The second effect of overhang is an increase of the twisting stiffness. This has less of an immediate effect but gradually reduces the plate twist compliance. Plate theory considers only the twist deformation of an ideal plate without overhang. This can explain why the analytical plate twist compliance exceeds the FEA predictions at large overhangs. For the panels considered here, the compliance values agree reasonably for overhangs between 2 and 5mm.

The compliance is displayed as a function of overhang in Figure 3.7.

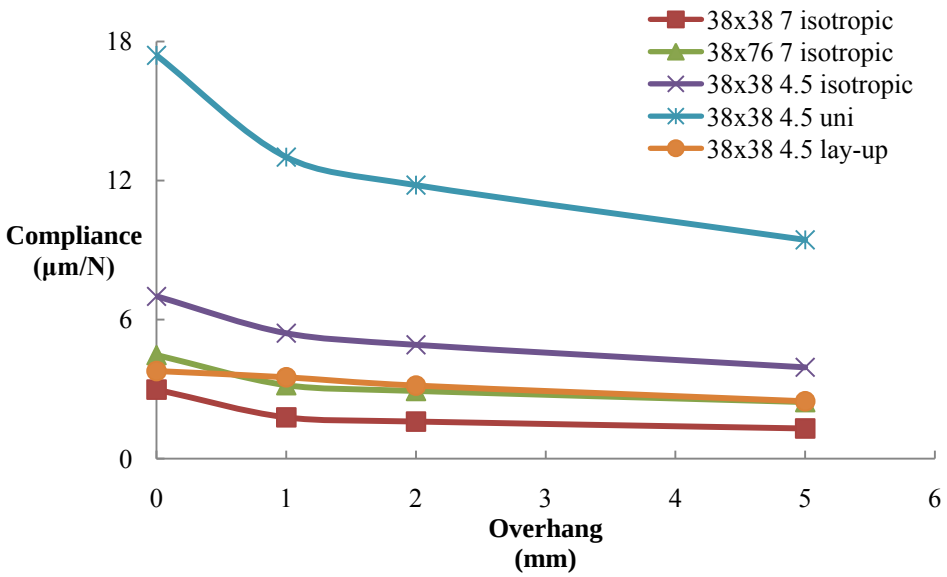

Figure 3.7: Effects of overhang on compliance. 38x38 represents the loaded dimensions (*axb*) of the ECT panel (Figure 3.3) and "7" the thickness in mm.

The compliance decreases with overhang quite rapidly at small overhang. This aspect of the response is primarily a result of the indentation. After about 2mm of overhang the compliance decreases as a result from stiffening due to the added overhang.

3.2.2 Effects of Plate Properties on Indentation

Indentation deformation at the points of load introduction and support regions, see Figure 3.8, will contribute to the recorded compliance of the test specimen, unless the deflections associated with such deformations are compensated for. In a typical ECT test, the small panel is difficult to access and the deflection is most commonly measured from the movement of the cross head of the machine. In the finite element analysis of the panels considered, load is introduced as a concentrated force acting on one node, and the support reactions, similarly, are assumed as point contacts. This is a conservative modeling method because the actual test configuration uses hemispherical loading and support pins which distribute the load over a larger area.

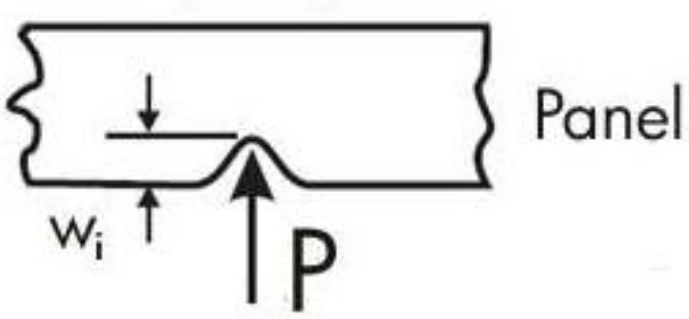

Figure 3.8: Determination of indentation.

As indicated in Figure 3.8, the indentation may be measured at the point of load introduction, w_B. To quantify indentation, the out-of-plane deflection of the panel, w is plotted along a line including the loaded point indicated in Figure 3.9.

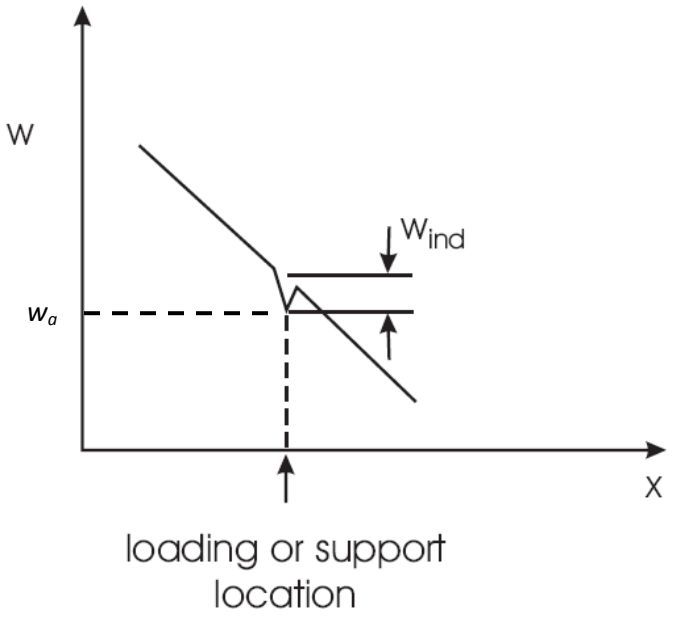

Figure 3.9: Determination of indentation from out-of-plane displacement curve.

The indentation, w_{ind}, manifests itself by a discontinuity in the smooth trend curve. To quantify the indentation, a smooth curve is assumed and w_{ind} is measured from the difference in the displacement between the interpolated trend curve, w, and the actual displacement, w_a, see Figure 3.9,

$$w_{ind} = w - w_a \tag{3.24}$$

It is recognized that the loading pin and supports in the actual ECT tests are pins with semi-spherical contacting surfaces, and as such, produce lesser indentations than the point contacts assumed in the FEA. Such loading may be simulated using more advanced analysis, but the concentrated loading/support assumption is expected to provide conservative results. In this part of the study we are considering the one-point loading

configuration, Figure 3.1. In this configuration corner *A* is subject to a concentrated load of magnitude *P*. Equilibrium of forces and moments require that all support locations (*B, C, D*) are subject to the same load (*P*), with the reaction loads at *B* and *D* acting upwards and support *C* acting downwards. The symmetry/ anti-symmetry of the loading/support configuration reveals that all contact points are subject to the same load and hence deform the same. Consequently, the indentation, w_{ind}, (Eq. (3.24)) may be determined from consideration of one corner only (here the loaded corner *A*).

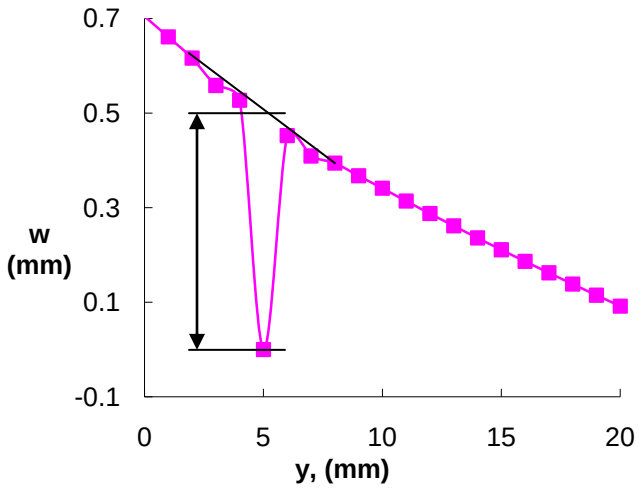

Figure 3.10: Illustration of method to determine indentation from the displacement curve for a 4.5mm thick isotropic square plate with an overhang of 5mm. Units of displacement are mm.

The indentation is determined from the displacement plots across a cross-section intersecting a loaded point, see the schematic in Figure 3.9 and an actual example in Figure 3.10. A normalized measure of deformation due to indentation is the indentation compliance, C_i, determined by dividing the indentation displacement by the load applied.

To determine the influence of the indentations at all four loading and support points we will consider the one-point and two-point ECT specimens at a time. If the one-point ECT fixture is viewed from the side at an angle where the two lower support pins align, the ECT loading configuration becomes very similar to a three-point beam bending test where the beam is loaded at the left end and supported at the center and the other end, see Figure 3.11.

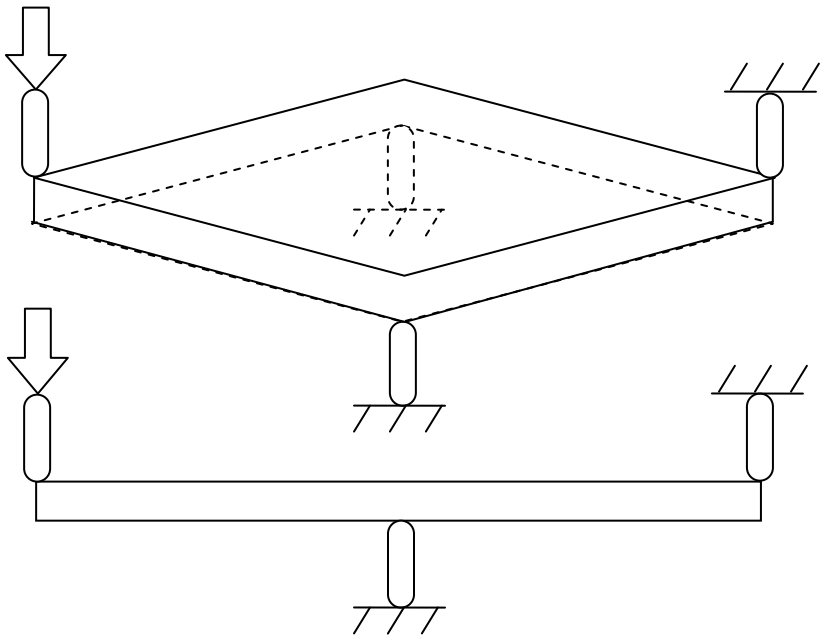

Figure 3.11: ECT one-point loading configuration viewed from side with the lower support pins aligned.

Using this reasoning identifies three indent points along the specimen. All four contact points have the same reaction load and overhang; therefore all have identical indentation. The indentation at each contact point will affect the panel compliance by a factor of three,

$$C=C^{*} - 3C_i \tag{3.25}$$

where C is the compliance after correction for indentation, C^* is the apparent plate compliance, and C_i is the indentation compliance, $C_i=w_i/P$, for each contact point. Using similar reasoning for the two-point test, leads to

$$C=C^* - 2C_i \tag{3.26}$$

Indentation compliance results are listed in Table 3.5. It is observed that the indentation compliance can be quite substantial. Comparisons with the total compliance values listed in Table 3.5 show that indentations at load introduction and support points may account for 10% of the cross head displacement for panels without overhang. For panels with overhang the influence is much less because the overhang region provides more support area directly around the loading and support points.

Table 3.5: Plate indentation compliance (μm/N).

L/S pt. *w*x*l* (mm)	h (mm)	material prop.	Overhang (mm)			
			0	1	2	5
38x38	7	isotropic	0.891	0.210	0.192	0.192
38x76	7	isotropic	0.921	0.210	0.192	0.192
38x38	4.5	isotropic	0.906	0.216	0.195	0.195
38x38	4.5	unidirectional	2.487	0.603	0.570	0.573
38x38	4.5	lay-up	0.750	0.082	0.078	0.078

For the isotropic panels, with overhang of 2mm or more, the indentation compliance reaches a value that remains fairly constant, independent of panel thickness and overhang. The indentation compliance for the unidirectional panel is much higher than for the isotropic panels which is attributed to the low out-of-plane stiffness (E_3=7.3 GPa).

3.3 Modeling of ECT Specimens with Overhang

This section presents modeling of ECT specimens tested in Section 2.4. As described in Section 2.4 this test program was done for carbon/epoxy ECT specimen of lay-up $[0/0/(\pm 45)_2/(\pm 45)_2/0/90]_s$ over a range of overhangs and crack lengths. Here, the shear stress distributions along the crack front and specimen compliance are considered. Most of the modeling was conducted on the one-point ECT specimen, although some two-point ECT configurations were considered.

3.3.1 Analysis of Crack Tip Shear Stress Distributions in ECT Specimen.

The main purpose of this study is to identify the most important geometrical factors of the ECT specimen influencing the uniformity of mode III crack loading while the mode II loading is kept at a minimum. Here, the distributions of the shear stresses τ_{yz} and τ_{xz} along the crack front provide estimates of the mode II and mode III stress intensity factors κ_{II} and κ_{III}, Figure 1.4,

$$\tau_{yz} = \frac{\kappa_{II}}{\sqrt{2\pi y}} \tag{3.27a}$$

$$\tau_{xz} = \frac{\kappa_{III}}{\sqrt{2\pi y}} \tag{3.27b}$$

where y is the distance from the crack tip, see Figure 1.12b.

$$G_{II} = \kappa_{II}^2 \frac{S_{11}}{\sqrt{2}} \left[\left(\frac{S_{22}}{S_{11}} \right)^{1/2} + \frac{2S_{12} + S_{66}}{2S_{11}} \right]^{1/2} \tag{3.28a}$$

$$G_{III} = \frac{\kappa_{III}^2}{2\sqrt{G_{23} G_{13}}} \tag{3.28b}$$

from Sih (38).

Another concern of this analysis relates to the ability of plate theory to model the compliance and energy release rate of the ECT specimen. The original plate theory analysis by Lee in 1993 (19) will thus be compared to compliance results from the FEA solution. The one and two-point ECT configurations were introduced in Section 1.5. Although the original one-point test specimen has greater overhang on one side, Figure 1.15a, the specimens analyzed here are assumed to be identical with symmetric overhang regions in the x and y directions, see Figure 3.12.

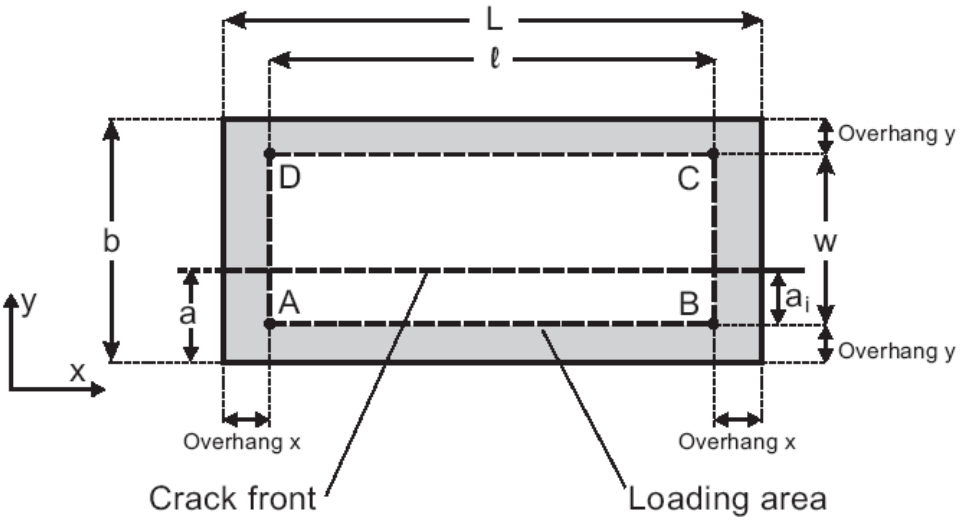

Figure 3.12: ECT specimen and definition of x and y-overhangs and loading area.

The points *A*, *B*, *C*, and *D* represent loading/support points, and the dotted rectangle represents the loading area. For reasons to be explained later, Figure 3.12 also provides two definitions of crack length, one of length *a* defined with reference to the edge (original definition), and another of length a_i defined as the distance from the loading line *AB* to the crack front. For the one-point loading configuration, the specimen

is loaded at point *A* and supported at points *B*, *C*, and *D*, while in the two-point configuration the specimen is loaded at points *A* and *C* and supported at points *B* and *D*, see Figure 3.12. The shear stresses τ_{yz} and τ_{xz} at the crack front (y=0) are calculated from finite element analysis using a reasonably refined mesh.

FEA models utilizing the FE code ANSYS (39) were developed. The flexibility of a universal model with the ability to change variables became necessary to efficiently model a series of ECT specimens. A macro based ECT model was developed to meet these criteria. The utilization of the macro code allows for a very complex model with quick adjustments of the variables (lay-up, crack length, geometry, material properties, etc.). All models utilized 3D SOLID 45 elements of the dimensions 1x1x0.1875 (mm) where the .1875mm dimension is the ply thickness. Each of the 24 layers was meshed separately using the same unidirectional carbon/epoxy material property set:

E_1= 113GPa, E_2=E_3=7.3GPa, ν_{12}=ν_{13}=.36, ν_{23}=.44,

G_{12}=G_{13}=4.14GPa, G_{23}=2.54GPa

The local coordinate system for the group of elements for each layer was then reoriented to accommodate the fiber direction. The cracked portion of the specimen is modeled with contact and target elements to allow frictionless contact of the crack faces without overlap of the elements. The boundary conditions and coordinate system for the panel can be referenced to Figure 3.12. For the 1-point test, point *A* is displaced 1mm in the negative *z* direction. Point *B* is fixed only in the *z* direction. Point *D* is fixed in all directions to prevent rigid body translation of the model, while point *C* is fixed along the

y and *z* directions. The *y* direction displacement at point *C* is fixed to prevent pivot rotations around the *z* axis through point *D*. The same *x* and *y* boundary conditions are applied to the one-point and two-point models. For loading of the two-point configuration, points *C* and *A* are displaced .5 mm in the negative *z* direction while points *B* and *D* are fixed in the *z* direction. The FE model determines the reaction loads developed at the contact and loading points. These loads are identical (within the numerical error). The applied deflection and reaction loads are used to evaluate the compliance of the ECT specimen.

The analysis agenda is presented in Table 3.6. Panels with constant dimensions of the loading rectangle were considered; *w=32mm* and *l=76mm.* This study first compares the one-point and two-point configurations at a crack length (a) of 15mm and constant *y-overhang* (*y-oh* = 3mm) for two x-overhangs (*x-oh* =3 and 5mm), cases 4-7. Subsequently, analysis is conducted over a range of crack lengths on the one-point configuration with overhang lengths in the *x* and *y-directions* of 3, 5, and 10mm.

Table 3.6: ECT modeling agenda. l=76mm, w=32mm, h=4.5mm

Case #	overhang x (mm)	overhang y (mm)	a (mm)	a_i *(mm)*	L (mm)	b *(mm)*
1	3	3	8	5	82	38
2	5	3	8	5	86	38
3	10	3	8	5	96	38
4	3	3	15	12	82	38
5	5	3	15	12	86	38
4*	3	3	15	12	82	38
5*	5	3	15	12	86	38
6	10	3	15	12	96	38
7	3	3	23	20	82	38
8	5	3	23	20	86	38
9	10	3	23	20	96	38
10	3	5	10	5	82	42
11	3	10	15	5	82	52
12	3	5	17	12	82	42
13	3	10	22	12	82	52
14	3	5	25	20	82	42
15	3	10	30	20	82	52

*) 2-point

Shear Stress Distributions

Distributions of shear stresses τ_{xz} and τ_{yz} were plotted along the crack front for each model. Because a displacement was applied to the modeled ECT specimen, not a specified load, all of the models have different reaction loads at the load/support pins. For a more reasonable comparison each set of τ_{xz} and τ_{yz} data was normalized by its corresponding reaction load. The resulting shear data is in the units of shear stress per unit applied load, τ/P. Similarly, the distance across the crack was presented as a ratio of the total distance across the crack, x/L, ($0 \le x/L \le 1$). Hence, the shear stress plots display

the normalized shear stresses, $\frac{\tau_{xz}}{P}$ and $\frac{\tau_{yz}}{P}$, vs. the normalized distance along the crack front, $\frac{x}{L}$.

The shear stresses, τ_{xz} and τ_{yz}, and strain energy release rate components, G_{III} and G_{II}, are shown in Figure 3.13, where G_{II} and G_{III} were calculated by Ratcliffe using the finite element code ABAQUS on the same carbon/epoxy ECT geometry with an identical lay-up, (40).

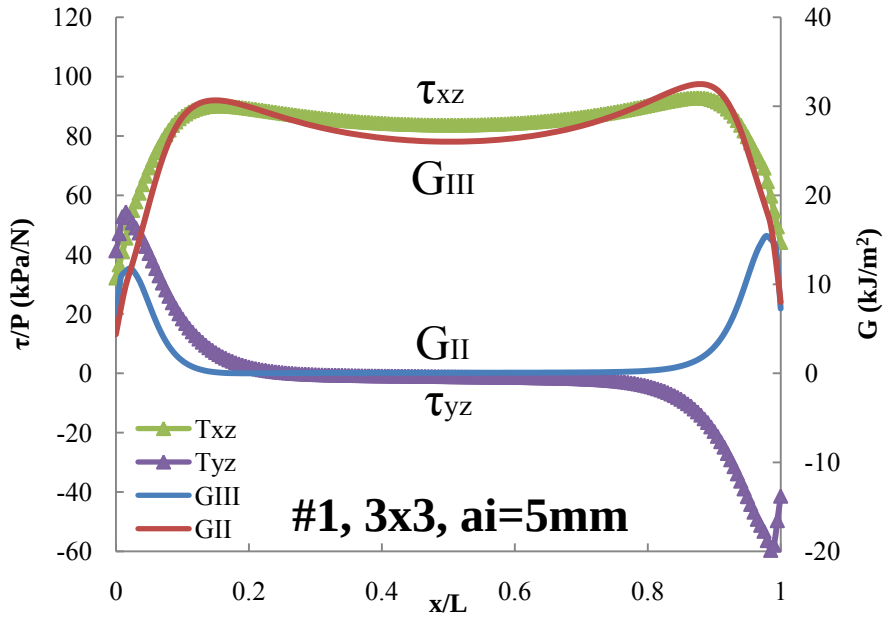

Figure 3.13: Shear stress plot of carbon/epoxy ECT specimen comparing trends to strain energy release rate.

The distributions of τ_{xz} and τ_{yz} are very similar to the G_{III} and G_{II} distributions. One exception is that G_{II} is always positive because it represents strain energy, whereas τ_{yz} assumes negative values close to the right edge.

Figure 3.14 shows shear stress distributions along the crack front for the one-point and two-point configurations for *x-oh* = 3 and 5mm, and *y-oh* =3mm (case 4, 5, 4*, and 5*). The crack length, a_i, Figure 3.12, was 12mm.

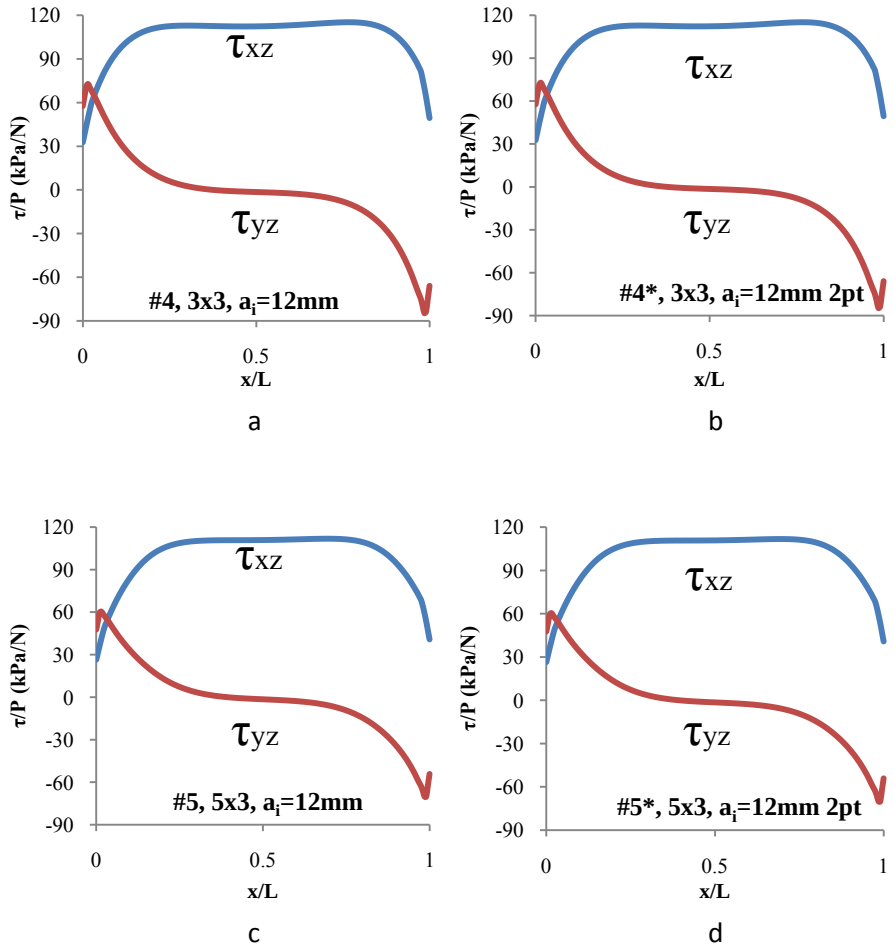

Figure 3.14: Shear stress distributions at the crack front for one-point and two-point ECT Specimens (a_i=12mm).

It is observed that the shear stress distributions for any specific panel do not depend on the loading configuration. The distributions of τ_{xz} and τ_{yz} along the crack front are similar to the G_{III} and G_{II} distribution found by Ratcliffe (25) for similar specimens. The largest magnitudes of the mode II shear stress τ_{yz} occur at points lined up with the

load introduction and support locations. The mode III shear stress, τ_{xz}, is fairly uniform within the loaded region but drops off near the free edges of the panel. The distribution of τ_{xz}, is most uniform for the smallest overhang (*x-oh* = 3mm) (Figure 3.14a and b). The peak value of the stress τ_{yz}, however, is higher for the smaller overhang length, although less than the maximum value of τ_{xz}. Hence, mode II crack propagation should not be an issue.

Figure 3.15 shows shear stress distributions for the one-point configuration at various overhangs in the *x* direction at a constant *y-overhang* (*y-oh* = 3mm) and crack length (*a*=8mm), (Cases 1, 2, and 3).

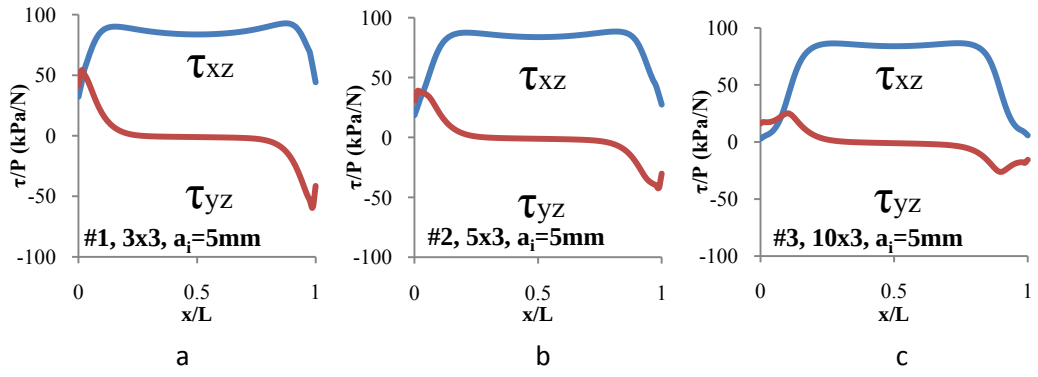

Figure 3.15: Shear stress distributions at the crack front for one-point ECT specimens for different *x-overhangs* at a_i=5mm.

These results show that the most uniform distribution of τ_{xz} occurs for the smallest *x-overhang* (*x-oh* = 3mm), Figure 3.15a. The shear stress τ_{yz} shows the largest values for the smallest overhang, but τ_{yz} is much less than that of τ_{xz}.

Figure 3.16 shows stress distributions for panels with a longer crack length (a_i=12mm) at a constant *y-overhang* (*y-oh*=3mm) and various *x-overhangs* (Cases 4, 5, and 6).

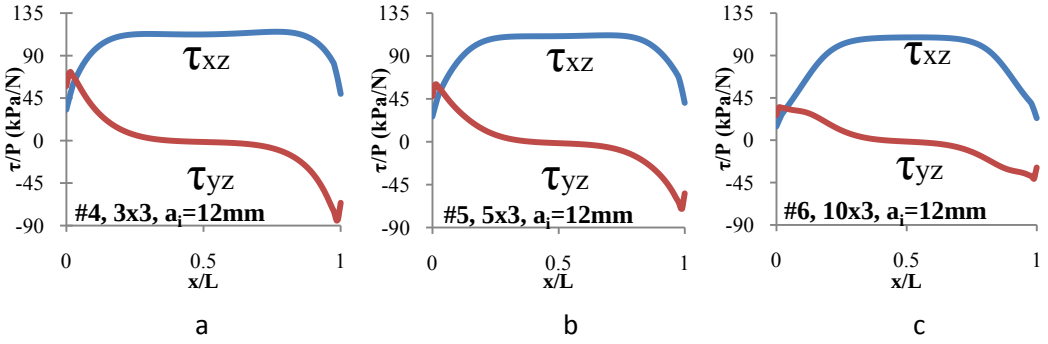

Figure 3.16: Shear stress distributions at the crack front for one-point ECT specimens for different *x-overhangs* at a_i=12mm

The shear stress, τ_{xz}, is fairly uniform for the panel with the shortest *x-overhang* (*x-oh*=3mm). For this overhang, however, the peak values of the shear stress, τ_{yz}, become comparable to the magnitude of τ_{xz}.

Shear stress distributions for ECT specimens with an even longer crack (a_i=20mm) are shown in Figure 3.17 (*y-oh* = 3mm), (Cases 7, 8, and 9).

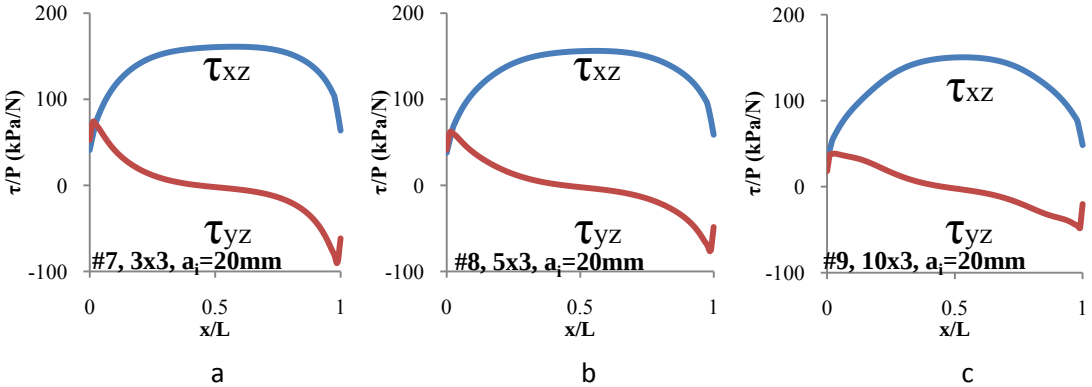

Figure 3.17: Shear stress distributions at the crack front for one-point ECT specimens for different *x-overhangs* at a_i=20mm.

The distributions of τ_{xz} shown in Figure 3.17 are highly nonuniform for all *x-overhang*s considered, suggesting an upper limit on crack length (a_i=12mm) when conducting fracture testing.

Shear stress distributions for panels with constant *x-overhang* (*x-oh*=3mm) and a range of *y-overhangs* (Table 3.6) are displayed in Figure 3.18-3.20. Figure 3.18 shows the results for *y-overhangs* of 3, 5, and 10mm at a crack length, a_i=5mm (Cases 1, 10, and 11).

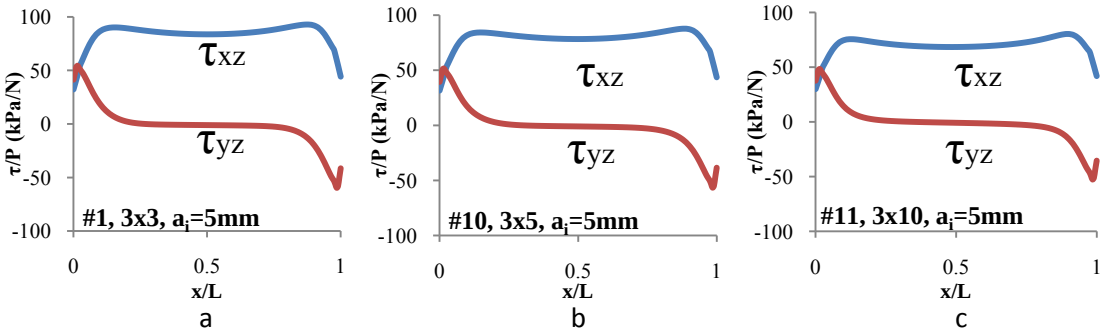

Figure 3.18: Shear stress distributions at the crack front for one-point ECT specimens for different *y-overhangs* at a_i=5mm

The distributions and magnitudes of τ_{xz} and τ_{yz} do not change much with changes in the *y-overhang*. Shear stress distributions for ECT specimens with longer crack lengths a_i=12 and 20mm, (Cases 2, 12, 13, and 3, 14, 15) are shown in Figure 3.19 – 3.20.

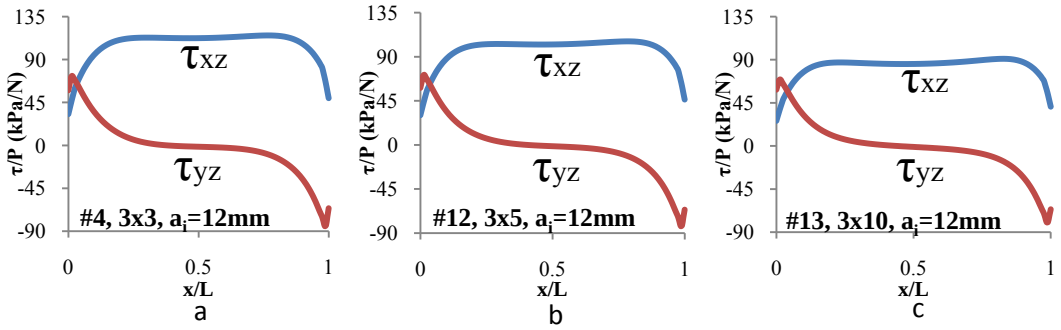

Figure 3.19: Shear stress distributions at the crack front for one-point ECT specimens for different *y-overhangs* at a_i=12mm.

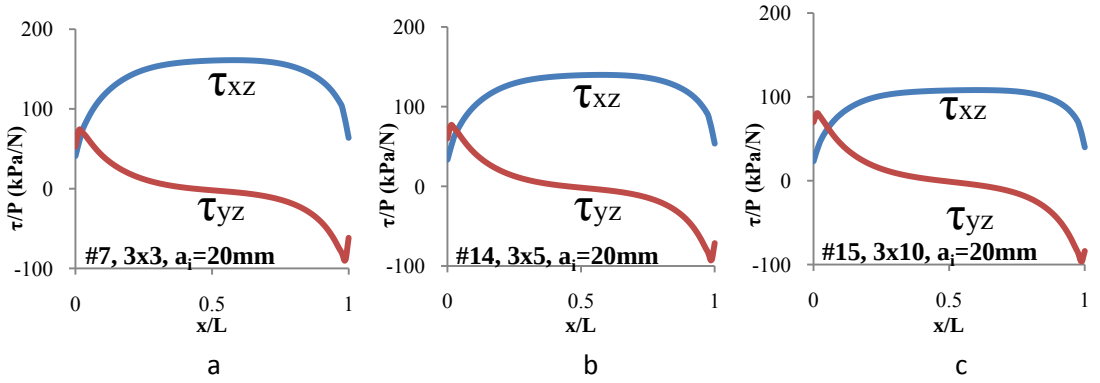

Figure 3.20: Shear stress distributions at the crack front for one-point ECT specimens for different *y-overhangs* at a_i=20mm.

The results shown in Figure 3.19 and 3.20 show that a large *y-overhang* leads to increased dominance of the mode II shear stress, τ_{yz}, regardless of the crack length, and that the shear stress, τ_{xz} is reduced.

Compliance values for the one-point ECT specimen determined from FEA and plate theory (Eq. (2.7)) are listed in Table 3.7. Plate theory is typically less compliant than FEA due to the neglection of transverse shear deformation and localized indentation deformation at the loading and support points.

Table 3.7: Compliance for one-point ECT specimen.

Case #	Oh x mm	Oh y mm	a mm	a_i mm	Load N	FEA C μm/N	CPT C μm/N
1	3	3	8	5	150	6.67	4.45
2	5	3	8	5	155	6.46	4.45
3	10	3	8	5	160	6.24	4.45
4	3	3	15	12	112	8.93	5.49
5	5	3	15	12	117	8.55	5.49
6	10	3	15	12	123	8.13	5.49
7	3	3	23	20	75	13.3	7.49
8	5	3	23	20	79	12.7	7.49
9	10	3	23	20	85	11.8	7.49
10	3	5	10	5	160	6.25	4.15
11	3	10	15	5	180	5.57	3.54
12	3	5	17	12	122	8.18	5.03
13	3	10	22	12	142	7.07	4.16
14	3	5	25	20	85	11.8	6.66
15	3	10	30	20	104	9.64	5.22

Figure 3.21 shows the compliance calculated from FEA and Eq. (2.7) vs. *x-overhang*. As overhang in the *x-direction* is not considered in the plate theory, Eq. (2.7), the CPT compliance remains constant. The FEA compliance however, decreases as a result of the stiffening by the overhang region.

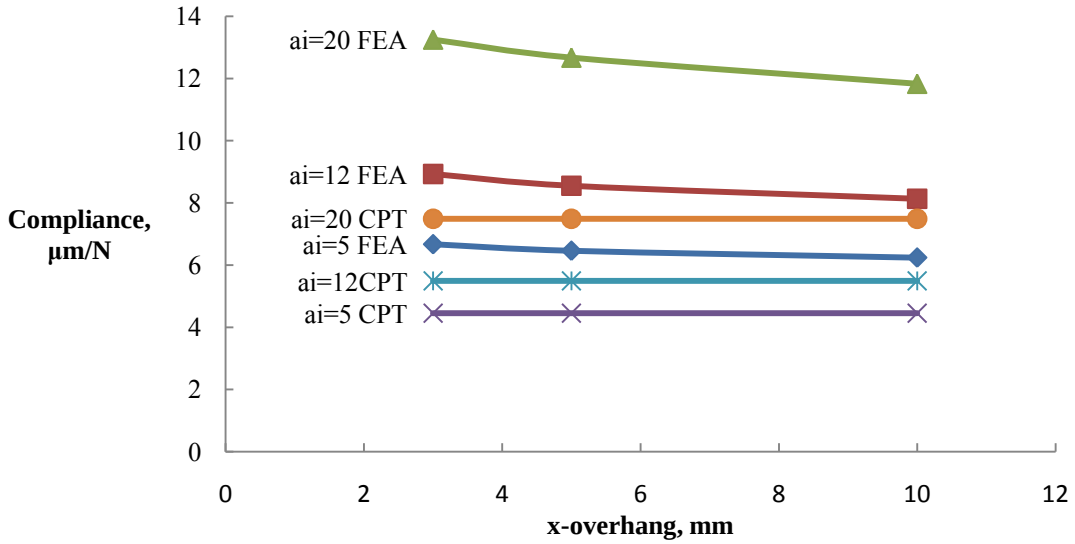

Figure 3.21: ECT specimen compliance as a function of *x-overhang*. The units for crack length, a_i, are in mm.

The influence of *y-overhang* on the compliance is shown in Figure 3.22.

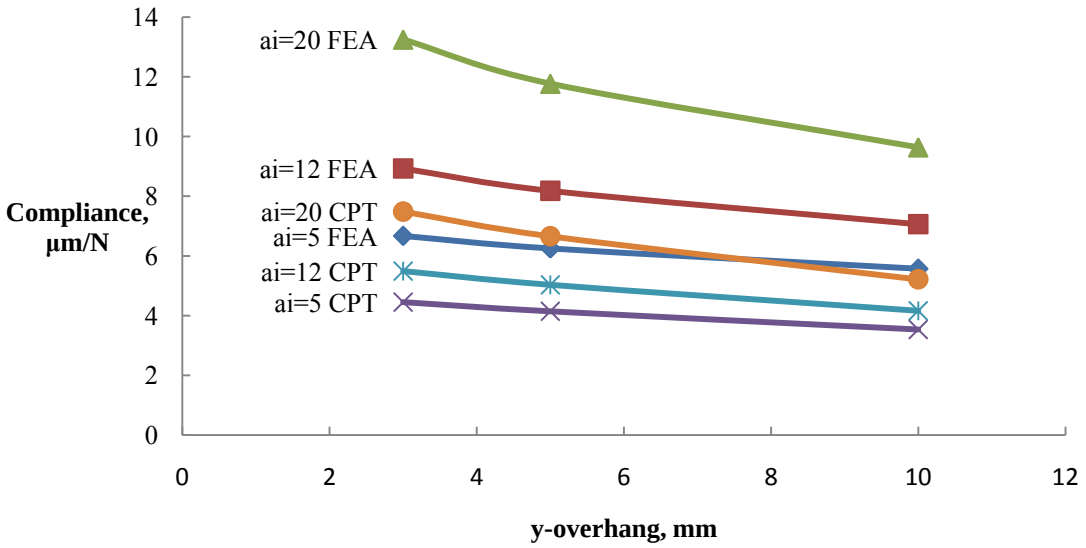

Figure 3.22: ECT specimen compliance as a function of *y-overhang*. Units of crack length, a_i, are mm.

Both the FEA and CPT compliances decrease with increasing overhang, but not in direct proportion, as is shown in Figure 3.23 where the compliance ratio, C_{FEA}/C_{CPT} is plotted vs. y-overhang.

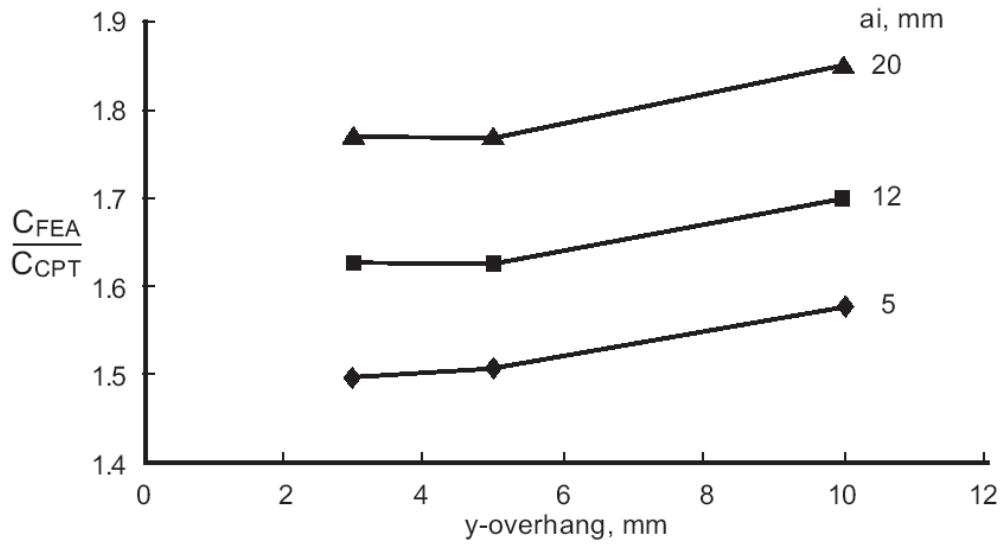

Figure 3.23: Compliance ratio, C_{FEA}/C_{CPT}, as a function of y-overhang.

Notice that increased overhang in the *y* direction results in more divergence of the FEA and CPT results, which clearly indicates the inability of the CPT formulation to properly model ECT specimens with overhang.

Assessment of crack propagation in the ECT test is based on the energy release rate, *G*. *G* is here determined by substitution of the finite element computed compliance into the plate theory expressions, Eqs. (2.14) and (2.16). In addition, *G* may be determined using compliance calibration of the finite element compliance results using the original and modified methods, i.e. Eqs. (2.16) and (2.19). For this purpose the finite

element computed compliance, *C*, is inverted and plotted versus crack length according to the original and modified crack length definitions in Eqs. (2.17) and (2.20), see Figure 3.24 and 3.25.

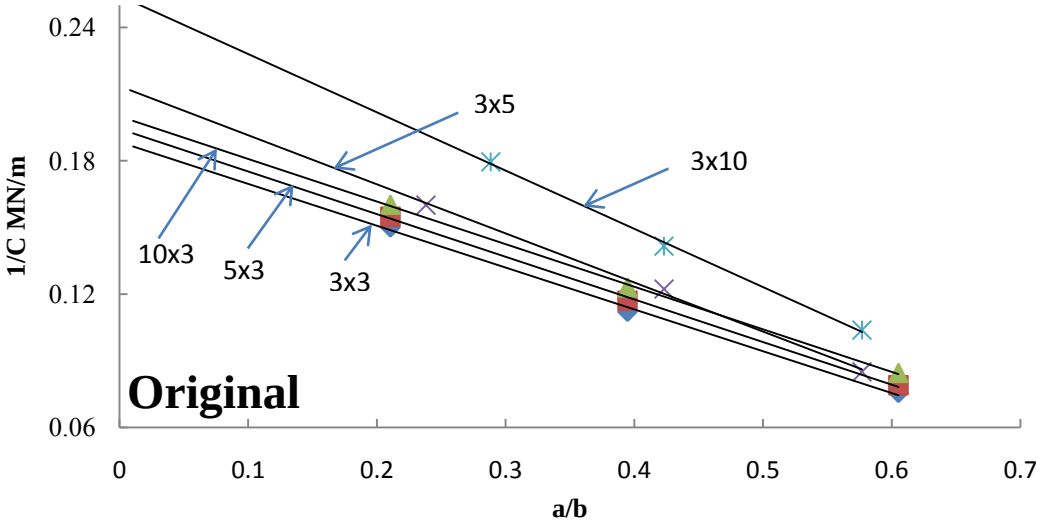

Figure 3.24: Stiffness of ECT specimen vs. crack length plotted according to the original method. Units of overhang are mm.

As pointed out earlier, increased overhang will increase the plate stiffness. Figure 3.24 shows that the compliance for a panel with a certain *y-overhang* closely follows the linear relationship between *1/C* and *a/b* as originally suggested by Lee (19). The lines for a specific *y-overhang* are parallel while an increase of the *y-overhang* is observed to increase the slope.

Figure 3.25 shows the stiffness plotted vs. crack length a_i normalized by the loading area width, *w*.

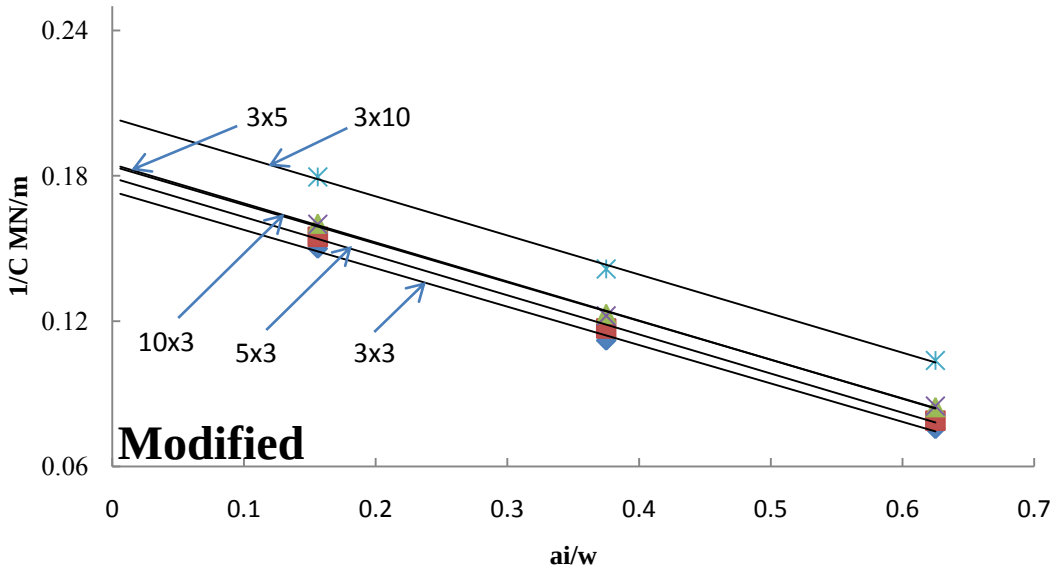

Figure 3.25: Stiffness of ECT specimen vs. crack length plotted according to the modified method. Units of overhang are mm.

The modified compliance calibration procedure, i.e., the focus on loaded dimensions, a_i and w, produces lines with almost identical slopes, in contrast to the original plots shown in Figure 3.24. This highlights the more physically based definition of crack length.

To determine the slope factor, m, defined in Eqs. (2.16) and (2.18), the slope of each line shown in Figure 3.24 and 3.25 was normalized by the stiffness at zero crack length. The results are listed in Table 3.8.

Table 3.8: Slope factor determined from FEA compliance calibration.

Oh mm	m original	m modified
3x3	0.999	0.914
5x3	0.988	0.902
10x3	0.958	0.873
3x5	1.034	0.868
3x10	1.031	0.792

Substitution of the slope factor, m, compliance, crack length, and a unit load P=1N in Eqs. (2.17) and (2.18) provides the energy release rate, G. Table 3.8 summarizes G values determined from compliance calibration of the FEA result (Eqs. (2.15) and (2.18)) and classical plate theory, Eqs. (2.10) and (2.16).

Table 3.9: Strain energy release rate results (P=1N).

Case #	Oh mm	a/b	a_i/w	G_{FEA}^{CC} orig. mJ/m^2	G_{FEA}^{CC} modified mJ/m^2	G_{CPT} orig. mJ/m^2	G_{CPT} modified mJ/m^2
1	3x3	0.211	0.156	1.462	1.461	1.185	1.333
2	5x3	0.211	0.156	1.395	1.394	1.148	1.291
3	10x3	0.211	0.156	1.297	1.297	1.109	1.247
4	3x3	0.395	0.375	2.552	2.551	1.957	2.267
5	5x3	0.395	0.375	2.396	2.395	1.874	2.171
6	10x3	0.395	0.375	2.170	2.171	1.781	2.064
7	3x3	0.605	0.625	5.804	5.800	3.958	4.866
8	5x3	0.605	0.625	5.386	5.382	3.785	4.653
9	10x3	0.605	0.625	4.675	4.677	3.534	4.344
10	3x5	0.238	0.156	1.343	1.291	1.034	1.249
11	3x10	0.288	0.156	1.035	1.035	0.786	1.113
12	3x5	0.405	0.375	2.280	2.166	1.643	2.077
13	3x10	0.423	0.375	1.636	1.636	1.173	1.794
14	3x5	0.595	0.625	4.960	4.596	3.127	4.322
15	3x10	0.577	0.625	3.107	3.107	2.006	3.540

The definition of crack length with respect to the external boundary of the panel leads to peculiar results. Consider for example the energy release rate results for cases 10 and 11 (a=10 and 15mm, a_i = 5mm). When the *y-overhang* is increased from 5 to 10mm the crack length (a) increases from 10 to 15mm while a_i remains constant. The value of G, however, decreases because of the increased *y-overhang*. A crack length definition

based on the loading area (a_i) thus makes more physical sense. G values determined using the original and modified compliance calibration methods are very similar. This has been shown mathematically by Ratcliffe (41). Hence, from a practical point of view, the compliance calibration modified method provides no improvement of data reduction analysis for G_{IIIc}.

The modified CPT procedure yields higher values of G than the original plate theory formulation Eq. (2.10), because the original plate theory uses the full specimen width, b, in the denominator while the modified CPT Eq. (2.16) uses the loaded width, w. Furthermore, the energy release rate determined using the modified CPT procedure is quite close to that determined by compliance calibration of the finite element results.

Figure 3.26 shows G plotted vs. crack length ratio according to the original and modified crack length definitions.

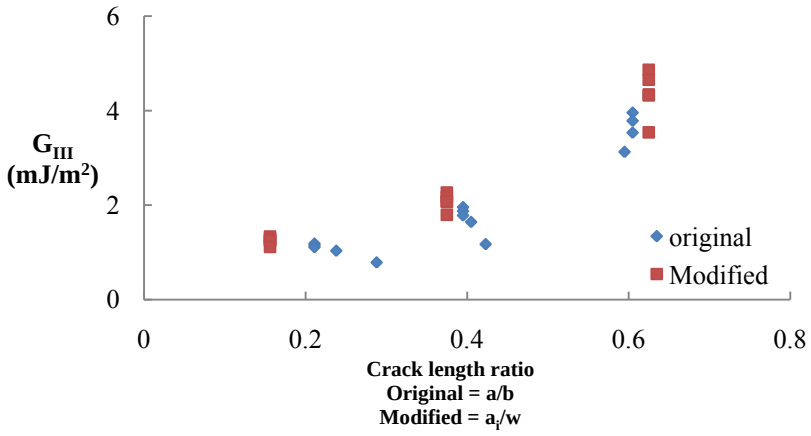

Figure 3.26: G_{III} determined according to the original and modified CPT methods.

The modified definition of crack length ratio provides a unique relation between G and crack length and a consistently increasing trend.

3.4 Specimen Modification Toward Pure Mode III Crack Loading

Analysis employing FEA modeling is here conducted on unidirectional ECT specimens devoid of bending/twisting coupling. This modeling will be followed by a modification of the ECT specimen to promote pure mode III loading of the crack front.

A concern of the current lay-up is that it includes the coupling terms (D_{16} and D_{26}). The laminated plate analysis presented in Section 3.1.3 shows that the response of uncracked orthotropic plates is governed by the D_{66} term. For the sublaminates, however, the bending/twisting coupling terms, D_{16} and D_{26}, are quite large, and may influence the response, especially at longer crack lengths. This may lead to inaccuracies of the analytical reduction methods that do not consider these terms (D_{16} and D_{26}). This influence may be the seed of the discrepancies between the experimental, FEA, and analytical compliance and fracture toughness reduction methods. To test this theory an FEA model is produced with an ECT specimen that is void of D_{16} and D_{26} bending/twisting coupling and compliance results from FEA and CPT compared for consistency. The specific lay-up of the carbon/epoxy laminate examined is $[90]_{24}$. The following carbon/epoxy ply properties were assumed in the modeling:

E_1= 113GPa, E_2=E_3=7.3GPa, ν_{12}=ν_{13}=.36, ν_{23}=.44,

G_{12}=G_{13}=4.14GPa, G_{23}=2.54GPa

The bending stiffness and compliance matrices for the carbon/epoxy laminate and sublaminates determined by PROMAL (37) are:

$$[D]_I = \begin{bmatrix} 55.9 & 20.1 & 0 \\ 20.1 & 865.3 & 0 \\ 0 & 0 & 31.4 \end{bmatrix} (Pa * m^3), \quad [D]_{II} = \begin{bmatrix} 7.0 & 2.52 & 0 \\ 2.52 & 108.2 & 0 \\ 0 & 0 & 3.93 \end{bmatrix} (Pa * m^3)$$

$$[d]_I = \begin{bmatrix} 1.8E^{-2} & -4.2E^{-4} & 0 \\ -4.2E^{-4} & 1.2E^{-3} & 0 \\ 0 & 0 & 3.2E^{-2} \end{bmatrix} \left(\frac{1}{Pa * m^3}\right),$$

$$[d]_{II} = \begin{bmatrix} 1.4E^{-1} & -3.4E^{-3} & 0 \\ -3.4E^{-3} & 9.32E^{-3} & 0 \\ 0 & 0 & 2.5E^{-1} \end{bmatrix} \left(\frac{1}{Pa * m^3}\right)$$

The bending stiffness and compliance matrices for both the full specimen and half specimen are free of bending/twisting coupling terms (D_{16} and D_{26}). This should promote agreement between the CPT and FEA calculated compliances of the ECT specimen, since the CPT method neglects bending/twisting coupling.

FEA models of the one-point ECT specimen were conducted utilizing the ANSYS code (39) using the same macro described in Section 3.3 with identical one-point boundary conditions and applied displacement. The FE model determines the reaction loads developed at the contact and loading points. The reaction loads are identical to the applied load (within the numerical error). Compliance was determined from the displacement divided by the load. The dimensions of the unidirectional ECT specimen were, according to Figure 3.12, L=82, b=38, l=76, w=32 (mm). Compliance of the ECT specimen was calculated from CPT (Eq. (2.7)) for crack lengths, a_i=-1, 0, 5, 12, 17, 22, 27, 32, and 35mm. The FEA was conducted up to a crack length of a_i= 12mm.

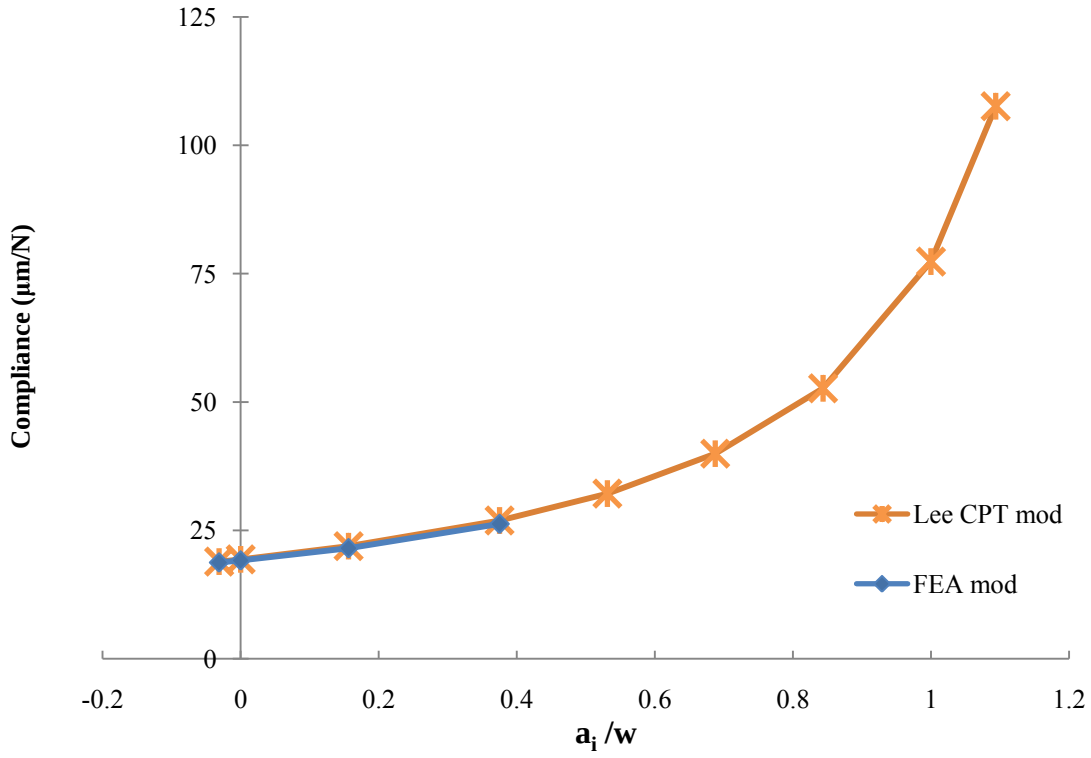

Figure 3.27: Compliance of a $[90]_{24}$ carbon/epoxy ECT specimen calculated from FEA and CPT vs. crack length ratio. Overhang is 3x3 (mm).

Compliance vs. crack length ratio results are shown in Figure 3.27. The modified FEA and CPT compliance results are in almost perfect agreement. The good agreement may be explained by the lack of D_{16} and D_{26} coupling terms in the unidirectional lay-up, and the small contribution from transverse shear deformation and indentation for this twist-flexible lay-up.

Shear stress (τ_{xz} and τ_{yz}) distributions at the crack front of the unidirectional and current lay-up ECT specimens are shown in Figure 3.28. The results for the current lay-up are from Section 3.3.1.

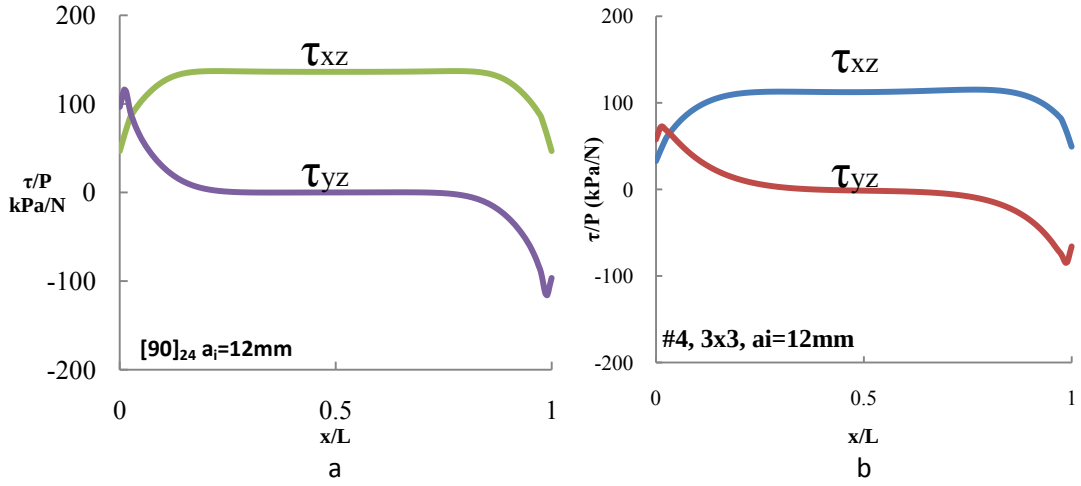

Figure 3.28: Shear stress distributions at the crack front for one-point carbon/epoxy ECT specimens with an overhang of 3x3 (mm) (a_i=12mm).
a) unidirectional, $[90]_{24}$ b) current lay-up, $[90/0/(\pm 45)_2/(\mp 45)_2/0/90]$.

The results in Figure 3.28a show that the normalized shear stress distributions in the 90° ECT specimen are very similar to those for the current lay-up ECT specimen, Figure 3.28b. The 90° lay-up ECT specimen produces a larger ratio of τ_{yz} to τ_{xz} near the edges of the crack front than does the current lay-up ECT specimen. Observations in Section 3.3 suggest that ply splitting is promoted by the shear stress τ_{yz}. Hence, an all 90° ECT specimen may be prone to ply splitting and is highly flexible in torsion. For example, the compliance of a 90° ECT specimen at a crack length of a_i=12mm is 3 times greater than that of the current lay-up at the same crack length.

3.4.1 SECT Specimen

In this section a new mode III fracture toughness specimen is proposed. As with the previous section a unidirectional lay-up, void of bending/twisting coupling, is utilized for the analysis of the proposed specimen. This proposed specimen is very similar to the ECT specimen and could closely be described as having a modified ECT specimen

geometry. It is hypothesized that the specimen is capable of producing a virtually pure mode III loading along the crack front. The proposed specimen employs a slightly more complex insert geometry that allows for a more direct control over specific shear stress distributions as a function of the geometry changes.

As shown earlier in this chapter, a persistent problem with the ECT specimen is its inability to produce a uniform distribution of the mode III shear stress, τ_{xz}, across the entire crack front. In addition, the mode II (τ_{yz}) influence is quite substantial. Increasing the *x-overhang* will reduce the magnitude of τ_{yz} but at the expense of a lesser portion of the crack front being loaded by mode III. When the *x-overhang* is minimized, the increased shear stress, τ_{yz}, may affect the determined G_{IIIc} and increase the probability of ply splitting. A solution to both of these problems is difficult to implement within the constraints of the geometry of the ECT specimen as the solution to one problem tends to elevate the other. To arrive at a solution, a new insert geometry is suggested, see Figure 3.29, here denoted "the staggered edge crack twist (SECT) specimen" SECT. The SECT specimen employs a staggered symmetric crack front as achieved by a specific insert geometry. The SECT specimen makes use of two crack fronts, i.e. a primary and a secondary, and is designed to fracture along the primary crack front only. Overhang of the SECT specimen is symmetric in the x and y directions and thus can be determined by subtracting the loading location dimensions from the overall specimen dimensions. Hence, the *x-overhang* $= (L_2 - l) / 2$ and the *y-overhang* $= (w - b) / 2$. The primary crack is located between the loading/support points, *A* and *B*, as highlighted in Figure 3.29.

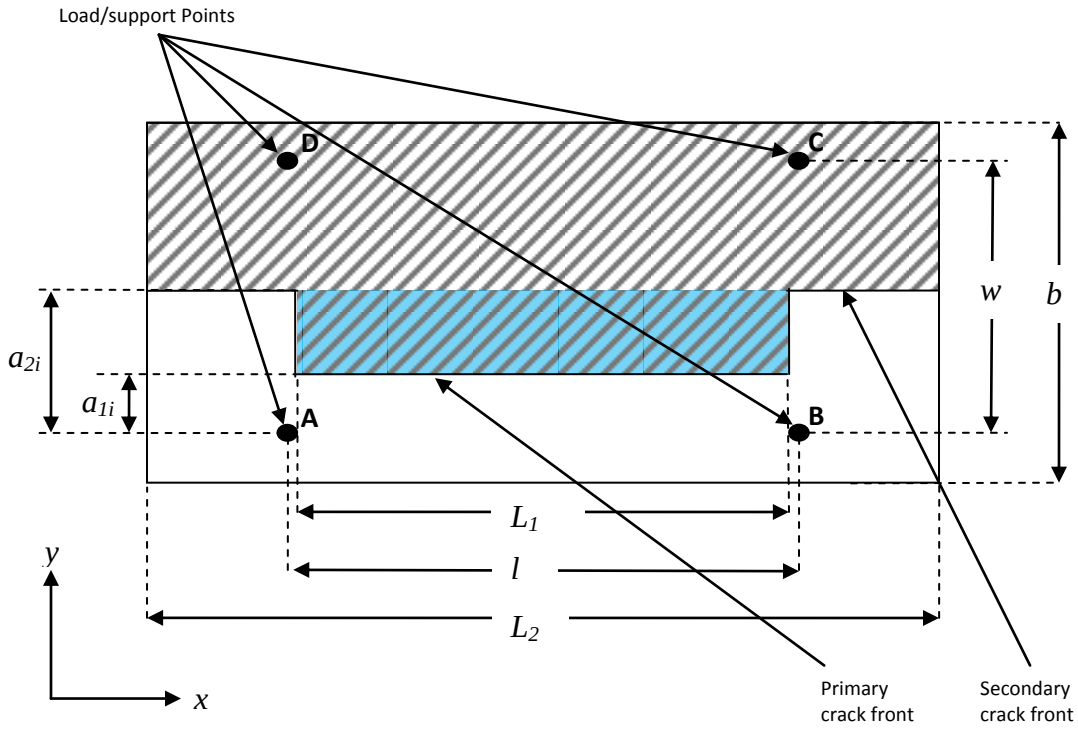

Figure 3.29: SECT specimen geometry.

The dual crack front geometry allows for a furthered degree of control over the shear stresses along each crack front. There are three main concerns when determining the desired SECT specimen geometry. First, uniformity of τ_{xz} along the primary crack front needs to be established. Second, the shear stress, τ_{yz}, along the primary crack front should be minimized. Lastly the peak magnitudes of both τ_{xz} and τ_{yz} along the secondary crack front must be kept low in order to avoid propagation along the secondary crack front.

FE calculations were conducted for a one-point carbon/epoxy $[90]_{24}$ SECT specimen of external dimensions, L_2=96 and b=38 (mm), and loading area dimensions of l=76 and w=32 (mm). The crack lengths a_{1i} and a_{2i} were 0 and 5mm. The material

properties and loading/support configuration of the SECT specimen are identical to those of the ECT specimen in Section 3.4. The lengths of the primary crack L_1 were 40 and 74 mm.

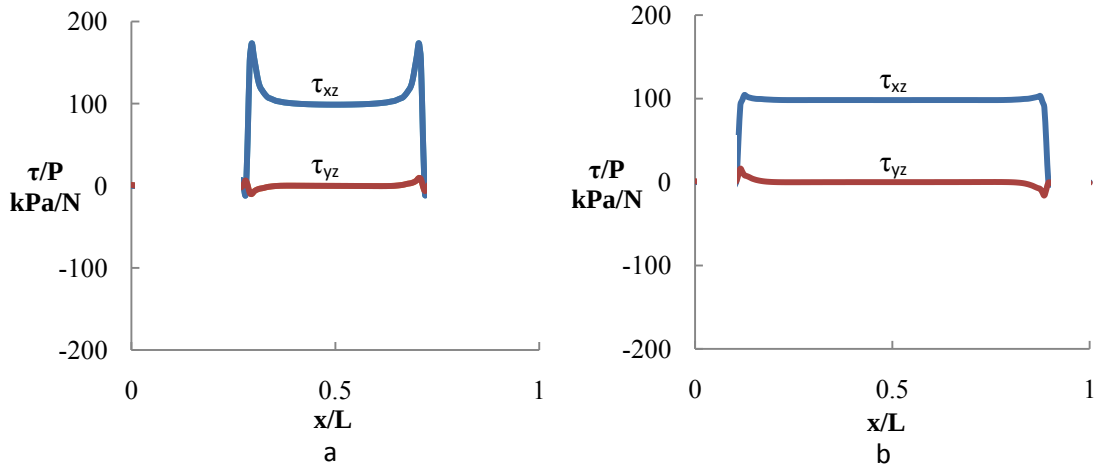

Figure 3.30: Shear stress distributions at the primary crack front for one-point an SECT specimen with the dimensions (b=38, a_{1i}=0, a_{2i}=5). a) L_1=40, L_2=96, b) L_1=74, L_2=96 (all dimensions in mm).

Figure 3.30 shows the shear stress distributions along the primary crack front for the two primary crack lengths (L_1 = 40 and 74mm). The crack length L_1 has a large effect on the mode III shear stress distribution along the primary crack front. A crack length of L_1=40mm yields high τ_{xz} stress peaks, see (Figure 3.30a). A longer primary crack, L_1=74mm, produces a quite uniform τ_{xz} (Figure 3.30b). Notice that this increase of L_1 also slightly elevates the τ_{yz} near the ends of the primary crack front, see Figure 3.30.

The length of the secondary crack (a_{2i} in Figure 3.29) must also be addressed. High shear stresses may initiate growth of the secondary crack. Furthermore, compliance calibration of the SECT specimen would demand testing specimens with fixed lengths L_1, L_2, and a_{2i} while extending the length a_{1i}. In this procedure the length of the secondary

crack length, a_{2i}, must exceed the longest primary crack tested. A problem with a long secondary crack is that the bonded area at the mid-plane in the *x-overhang* region of the material is decreased, see Figure 3.29. It is this bonded area in the *x-overhang* region that transfers shear forces between the upper and lower sublaminates, and reduction of this area elevates the mode II shear stresses present along the primary crack front.

Figure 3.31 shows the distribution of shear stresses, τ_{xz} and τ_{yz} along the secondary crack front.

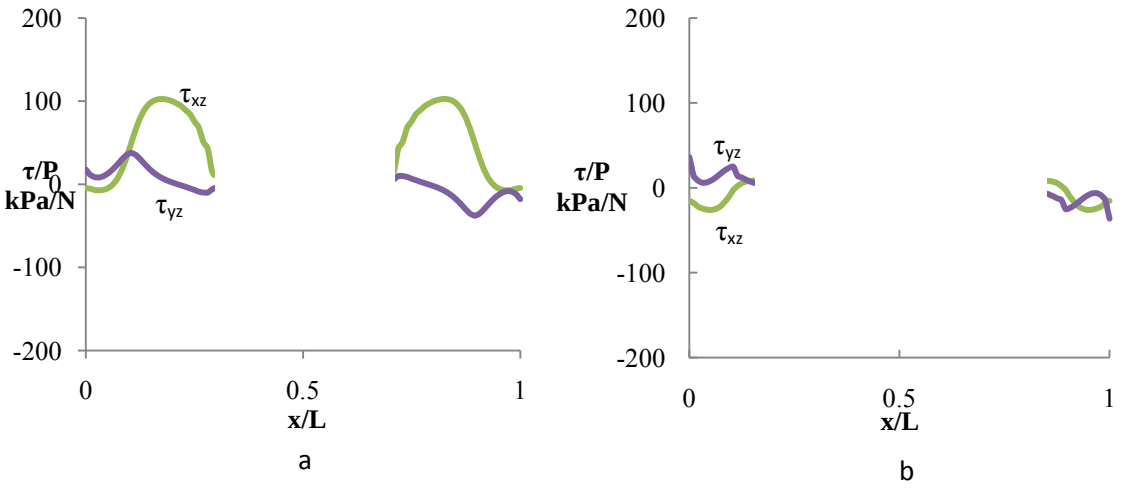

Figure 3.31: Shear stress distributions at the secondary crack front for a one-point SECT specimen with the dimensions (b=38, w=32, l=76, L_2=96, a_{1i}=0, a_{2i}=5). a) L_1=40, b) L_1=74 (all dimensions in mm).

The shear stress τ_{xz} for L_1=40mm is quite high along the secondary crack front, see Figure 3.31a, comparable to the magnitude of the shear stress, τ_{xz}, along the primary crack, Figure 3.30a. Such a high shear stress could lead to propagation of the secondary crack. The SECT specimen with an extended L_1 produces low shear stresses along the secondary crack as shown in Figure 3.31b. The increase in L_1 to 74mm significantly reduces τ_{xz}.

An SECT specimen with the proper dimensions can produce desirable shear stress distributions across both crack fronts (primary and secondary). An iteration process was used to produce the following results. Figure 3.32 represents shear stress distributions for an SECT specimen geometry of the dimensions b=38, w=32, l=76, L_1=74, L_2=108, a_{1i}= 0, and a_{2i}=5 (mm).

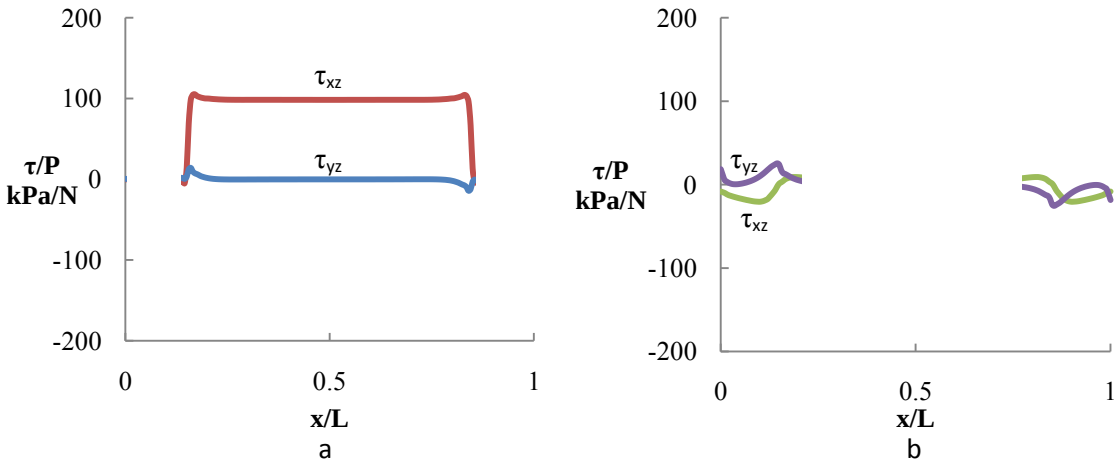

Figure 3.32: Shear stress distributions at the primary and secondary crack fronts for a one-point SECT specimen. a_{1i}=0, L_1= 74 a_{2i}=5, L_2= 108. (overhang-16x3) a) primary crack front b) secondary crack front (all dimensions in mm)

Notice that τ_{yz} is insignificant relative to τ_{xz} and that τ_{xz} is uniform across the entire primary crack front. Both the τ_{xz} and τ_{yz} shear stresses along the secondary crack front are far below, τ_{xz}, along the primary crack front.

In order to perform compliance calibration on the SECT specimen it is crucial that there is a reasonable change in compliance as the crack length is increased. This procedure demands testing of SECT specimens over a range of primary crack lengths, a_{1i}, while the other dimensions remain fixed.

FEA of SECT specimens with crack lengths a_{1i}=0, 5, and 8mm, were conducted (L_1=74, L_2=108, and a_{2i}=20 (mm)) to determine whether a compliance calibration on an SECT specimen is feasible. Figure 3.33 shows compliance plotted vs. normalized crack length.

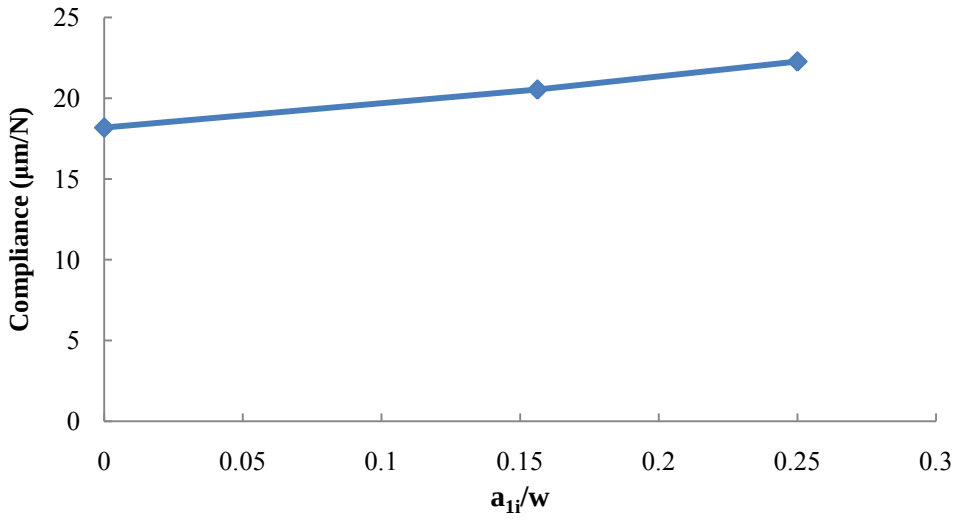

Figure 3.33: Compliance of unidirectional carbon/epoxy SECT specimen. (L_1=74, L_2=108, a_{2i}=20 (mm)

The compliance of the SECT specimen as determined through FEA does prove to increase with crack length. The slope of the line, however, is quite low, and it is questionable if the compliance calibration can be applied to the SECT specimen. A related issue is if G is large enough to drive the crack in experimental testing. This would require further analysis and testing. Notice that the $[90°]_{24}$ laminate may not be feasible for ECT fracture testing because of its low twisting stiffness, D_{66} (31.4 Nm vs. 139.8 Nm for the current lay-up).

4 Comparison of ECT Specimen Compliance and Energy Release Rate Determined from Analysis and Experiments

Predictions of ECT specimen compliance from CPT and FEA (Chapter 3) will be compared with experimentally determined values (Chapter 2) for the one-point and two-point ECT specimens. A comparison of data reduction methods for G_{IIIc} is also presented in this chapter. The CPT, CC, and CECC data reduction methods will be used to determine G_{IIIc} from an experimental data set with the original and modified methods.

4.1 Overhang Series

Experimental compliance results for the overhang series and data reduction methods for G_{IIIc} are discussed in Section 2.4. Finite element analysis of the ECT is presented in Chapter 3. The experimental test data was determined using the modified two-point ECT fixture whereas the FEA modeling was conducted on the one-point configuration. As discussed in Section 2.3, however, the ECT compliance for any given specimen determined from the one-point and two-point ECT configurations will differ by a factor of four. Hence, for purposes of comparison, the experimental compliance values are multiplied by a factor of four. This will be indicated (x4) where the adjustment is implemented.

Compliance data for carbon/epoxy ECT specimens obtained from the experimental and FEA overhang series presented in Section 2.4 and 3.3 is listed in Table 4.1. "CPT *C*" and "Mod CPT *C*" refer to compliance calculated using the original and modified plate theory expressions, Eqs. (2.7) and (2.16a).

Table 4.1: Experimental and analytical ECT compliance results.

Oh x mm	Oh y mm	a_i mm	a/b	a_i/w	Compliance μm/N			
					Exp x4	Orig. CPT	Mod. CPT	FEA
3	3	5	0.211	0.156	5.16±.11	4.45	5.01	6.67
5	3	5	0.211	0.156	4.96±.12	4.45	5.01	6.46
10	3	5	0.211	0.156	4.84±.08	4.45	5.01	6.24
3	3	12	0.395	0.375	6.28±.05	5.49	6.36	8.93
5	3	12	0.395	0.375	6.40±.17	5.49	6.36	8.55
10	3	12	0.395	0.375	6.32±.07	5.49	6.36	8.13
3	3	20	0.605	0.625	9.92±.45	7.49	9.20	13.3
5	3	20	0.605	0.625	9.40±.27	7.49	9.20	12.7
10	3	20	0.605	0.625	9.84±.14	7.49	9.20	11.8
3	5	5	0.238	0.156	5.08±.14	4.15	5.01	6.25
3	10	5	0.288	0.156	4.44±.11	3.54	5.01	5.57
3	5	12	0.405	0.375	6.16±.11	5.03	6.36	8.18
3	10	12	0.423	0.375	5.64±.14	4.16	6.36	7.07
3	5	20	0.595	0.625	9.00±.17	6.66	9.20	11.8
3	10	20	0.577	0.625	8.00±.19	5.22	9.20	9.64

The original CPT method consistently provides the smallest compliance values. This method does not consider *x-overhang*. Similarly, the modified CPT method does not consider overhang, but its emphasis on the loading geometry provides overall better agreement with experimental results and FEA predictions than the original method. The modified CPT compliance predictions exceed the experimental data, but less so than

FEA. The FEA results are the most compliant for every case, which may be attributed to excessive indentation deformation at load introduction and support locations as a result of the concentrated applied loads/reactions, see Section 3.2.2. The experimental data and FEA results show a stiffening trend with an increase in the *x-overhang*.

Figure 4.1 shows measured and calculated compliances as a function of crack length ratio a_i/w. All curves represent ECT specimens with an *x-overhang* of 3mm and *y-overhang* of 10mm.

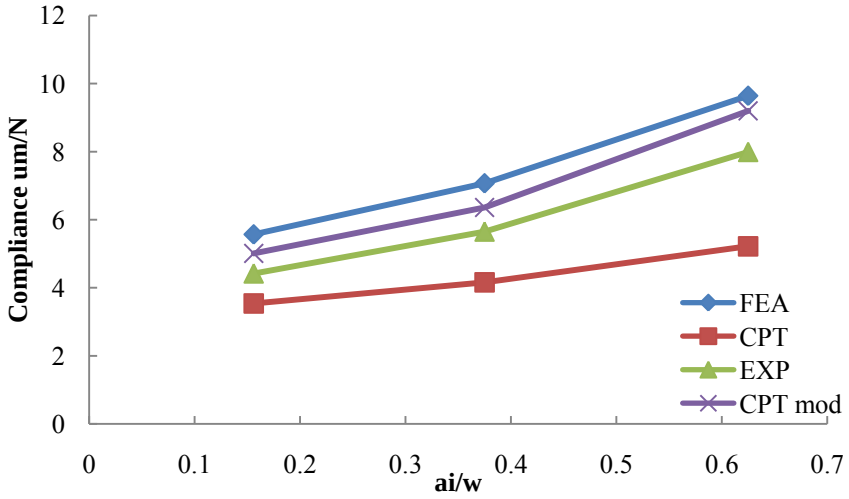

Figure 4.1: Compliance of carbon/epoxy ECT specimens with 3x10mm overhang.

The FEA compliance exceeds the experimentally measured values but the trend is similar. The CPT compliance falls below the other results. The modified CPT compliance is close to the FEA predictions and experimental compliance results.

4.2 Data Reduction Methods for G_{IIIc}

Data reduction methods for G_{IIIc} are compared in this section. Experimental data for carbon/epoxy ECT specimens with 3x3 (mm) overhang presented in Section 2.4.2, are

specifically examined. The data was collected over a range of crack lengths. Data reduction for G_{IIIc}, discussed in Section 2.3, utilizes Lee's original classical plate theory (CPT) and compliance calibration (CC) methods. Modifications made to these equations as well as the classical experimental compliance calibration (CECC) method were discussed in Section 2.3.1. The original compliance calibration method (CC) determines the slope of the stiffness (*1/C* plot vs. crack length ratio (*a/b*)). From the slope and the critical load used to fracture the ECT specimen the CC method determines G_{IIIc} using Eqs. (2.14) and (2.15). The classical plate theory method (CPT) calculates G_{IIIc} from the critical load and compliance, demensions, and the material properties of the ECT specimen, see Eqs. (2.10). The CECC method fits a polynomial (Eqs. (2.19)) to compliance data, and uses Eqs. (2.20a) or (2.20b) to determine G_{IIIc}.

Table 4.2 displays G_{IIIc} data for individual test specimens. The data set in Table 4.2 is consistent without much specimen-specimen scatter. G_{IIIc} is plotted vs. a_i/w in Figure 4.2.

Table 4.2: G_{IIIc} of carbon/epoxy determined using various experimental data reduction methods 3x3(mm) overhang.

ai/w	GIII CC orig. kJ/m^2	GIII CC mod kJ/m^2	GIII CECC kJ/m^2	GIII CC CPT kJ/m^2	GIII CC CPT mod kJ/m^2
0.16	1.00	1.00	1.25	0.87	0.98
0.16	1.08	1.09	1.40	0.94	1.06
0.16	1.06	1.06	1.37	0.92	1.04
0.38	1.05	1.05	1.97	0.88	1.02
0.39	1.07	1.08	2.04	0.89	1.05
0.39	1.10	1.10	2.06	0.92	1.07
0.63	1.35	1.36	1.85	1.05	1.30
0.64	1.33	1.34	1.79	1.03	1.28

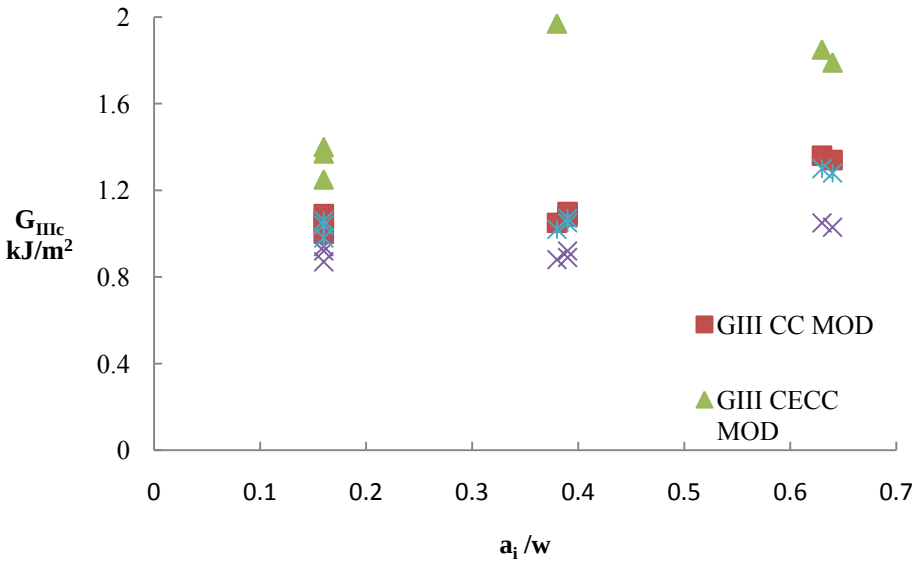

Figure 4.2: G_{IIIc} for carbon/epoxy determined using CC, CECC, and CPT data reduction methods for specimens with a 3x3(mm) overhang.

The CECC method result in much higher G_{IIIc} than the other methods. The CC methods and CPT methods produce similar G_{IIIc} values that are reasonably uniform over a series of crack lengths. The original CPT method is slightly lower for all crack lengths. The modified CPT method produces G_{IIIc} data very similar to the CC G_{IIIc} data for this case.

Based on the results shown in Figure 4.2 the CC method is recommended for data reduction.

4.3 Comparison of G_{IIc} and G_{IIIc}

The delamination toughness values determined here are compared to G_{IIc} and G_{IIIc} values reported in previous studies. Results are displayed in Table 4.3. Our G_{IIc} data refer to those determined using the beam theory method on precracked specimens, see Section 2.2 where our G_{IIIc} values were in all cases determined using the one-point ECT test data reduced by the compliance calibration method. These G_{IIIc} values are an average of all the data over the entire range of crack lengths a_i=5, 12, and 20mm.

Table 4.3: Delamination fracture toughness (kJ/m^2).

Carbon/Epoxy		**Glass/Epoxy**	
G_{IIc}	**G_{IIIc}**	**G_{IIc}**	**G_{IIIc}**
1.06±.10 (21)	1.43±.12 (21)	1.79±.21 (29)	1.23±.09 (29)
1.33±.30 (30)	1.35±.30 (25)	1.76±.03 (30)	3.25±.40 (25)
.612±.06 (*)	1.40 ±.24 (*)	1.15±.22(*)	2.72 ±.29 (*)

* Current study

The mode II fracture toughness of carbon/epoxy determined in the current study is quite a bit lower than the values recorded by others. This could be accounted for by a weak fiber/matrix interface in the panel that the specimens where cut from. Mode III toughness values are comparable to previous data and the standard deviations are reasonable. For our carbon/epoxy and glass/epoxy, G_{IIIc} is greater than G_{IIc}, in agreement with most published data listed in Table 3.4.

5 Conclusions

The objectives of this study were to examine the one and two-point ECT tests, provide improved geometry of the test specimen, and improved data reduction methodology to more accurately determine the mode III delamination fracture toughness of composite materials. Results from a comprehensive testing and analysis program on carbon/epoxy and glass/epoxy ECT mode III delamination specimen have been presented. Basic ply properties of the composites were determined using strain gage instrumented tensile test specimens. Mode II delamination tests were conducted using ENF specimens. It was found that compliance calibration and direct application of beam theory yield similar G_{IIc} values. Non-precracked specimens produced, on the average, 17% higher mode II toughness (G_{IIc}) values for carbon/epoxy and 14% higher G_{IIc} values for glass/epoxy. G_{IIc} for the glass/epoxy composite (1.07kJ/m^2) was substantially higher than that for carbon/epoxy (G_{IIc}=.582kJ/m^2), which is attributed to a weak fiber/matrix interface for the carbon/epoxy ENF specimens.

A comprehensive analysis program of the ECT specimen was conducted. To examine uniformity of crack loading in the ECT specimen, shear stress distributions at the crack front were determined from finite element analysis. The shear stress distributions in the one-point and two-point tests are virtually identical, indicating that either of the two tests could be used interchangeably. The finite element analysis results presented herein point to geometry changes of the ECT test specimen that may improve the test. The analysis suggests, based on uniformity of the mode III shear stress, τ_{xz}, distribution, that the overhang length in the *x-direction* (along the crack front) should be

kept at a minimum, dictated by the need to keep the mode II shear stress, τ_{yz}, below some critical value and reduce indentation. The *y-overhang* (perpendicular to the crack front) does not have a substantial influence on the uniformity of the shear stress, τ_{xz}, but adds stiffness to the specimen which is not accounted for properly in the plate analysis and also slightly raises mode II shear stress, τ_{yz}. Hence, the *y-overhang* should be minimized. Based on this analysis a symmetric overhang of 2-3mm in both directions appears reasonable. The analysis shows also that the distribution of τ_{xz} becomes highly nonuniform at large cracks. It is therefore proposed to test specimens with longer crack lengths (a_i/w>.38) for compliance calibration only.

A modified compliance formula based on the loaded area dimensions of the ECT specimen was proposed. The experimental compliance data on carbon/epoxy ECT specimen, suggests that the modified compliance calculations produce much more agreeable results with the analytically produced compliance predictions. Delamination fracture testing of carbon/epoxy and glass/epoxy ECT specimens using the one-point and two-point methods revealed that one-point ECT testing provides more uniform G_{IIIc} data. It was found that G_{IIIc} increased with crack length. Nonuniform crack growth is a result of nonuniform distribution of G_{III} which most likely is responsible for the elevation in G_{IIIc} of long crack lengths. G_{IIIc} for glass/epoxy was higher than that for carbon/epoxy, consistent with the mode II test results for these two composites. The experimental overhang series verified that the minimized overhangs produced the most uniform delamination fracture toughness over a range of crack lengths.

A modified ECT specimen called “SECT” with a staggered crack front is here suggested to produce uniform mode III crack loading. Finite element analysis of the

SECT specimen shows that proper dimensioning of the crack fronts result in a nearly uniform mode III shear stress distribution along the crack front with minor mode II influence. Compliance data for the SECT specimen, however, were quite insensitive to crack length, making application of the compliance calibration methods for data reduction uncertain.

References

1. Daniel, I. M., Ishai O. Engineering Mechanics of Composite Materials, Second Edition. New York: Oxford University Press, 2006.

2. Pipes, R. B., Blake Jr. R.A., Gillespie Jr., J.W., Carlsson L.A.,. TEST METHODS, Delaware Composites Design Encyclopedia. Vol. 6. Lancaster: Technomic, 1990. 113-119, 146-158.

3. Raju I.S., O'Brien T.K. "Fracture mechanics concepts, stress fields, strain energy release rates, delamination initiation and growth criteria". *Delamination behaviour of composites*. Boca Raton: CRC Press.

4. Freitas G., Fusco T., Campbell T., Harris J., Rosenberg S. "Z-fiber technology and products for enhancing composite design." 83rd AGARD Conference Proceedings of Structures and Materials Panel, 1996.

5. Irwin G.R. "Fracture" Handbook of Physics. Vol. 6. Berlin, Germany: Springer, 1958. 551.

6. Chandrupatla T.R., Belegundu A.D. Introduction to Finite Elements in Engineering. Third Edition. Upper Saddle River: Prentice-Hall, 2002.

7. D5528-94a, ASTM Standard. "Test Method for Mode I Interlaminar Fracture Toughness of Unidirectional Fiber-Reinforced Polymer Matrix Composites." West Conshohocken: American Society for Testing and Materials, 2001.

8. Adams D.F., Carlsson L.A., Pipes R.B. "Experimental Characterization of Advanced Composite Materials", Third Edition. Boca Raton: CRC Press, 2003.

9. Barret, J.D., Foschi R.O. Mode II stress intensity factors for cracked wood beams. "*Engineering Fracture Mechanics*" Vol. 9. 1997. 371-379.

10. Russell A.J., Street K.N. "Factors affecting the interlaminar fracture energy of graphite/epoxy laminates." ICCM-IV, ASM International. Tokyo: s.n., 1982. 279-286.

11. Davidson B.D. "Towards ASTM standardized test for determining of unidirectional laminate polymeric matrix composites." American Society for Composites annual meeting, Detroit, September 2006.

12. Wang S.S. "Fracture Mechanics for Delamination Problems in Composite Materials" *Journal of Composite Materials,* Vol. 17, 1983: 210

13. Krueger R., Minguet, P.J. "Skin-Stiffener Debond Prediction Based on Computational Fracture Analysis", NASA/CR-2005-213915, NASA Langley Research Center, VA, 2005.

14. Donalson, S. L. "Mode III Interlaminar Fracture Characterization of Composite Materials". *Composite Science and Technology*. Vol. 32, 1988. 225-249.

15. Martin R.H. "Evaluation of the Split Cantilever Beam for Mode III Delamination Testing." *Composite Materials, Fatigue and Fracture*, Vol. 3, American Society for Testing and Materials, Philadelphia, 1991: 243-266. .

16. Becht, G. J. "An Investigation of Interlaminare Fracture Under Mode III Loading." *Master's Thesis*, University of Delaware, 1988.

17. Becht, G. J., Gillespie Jr. J.W. "Numerical and Experimental Evaluation of the Mode III Interlaminar Fracture Toughness of Composite Materials". *Polymer Composites*, Vol. 10, 1989.

18. ASTM. "Standards and Literature References for Composite Materials." First Edition. Philadelphia: 1987.

19. Lee, S. M. "An Edge crack torsion method for mode III delamination fracture testing". Journal of Composites Technology and Research, Vol. 15, 1993: 193-201.

20. Li , J., Lee S.M., Lee E.W., O'Brien T.K. "Evaluation of the edge crack torsion (ECT) test for mode III interlaminar fracture toughness of laminated composites". *Journal of Composites Technology and Research*, Vol. 19, 1997: 174-183.

21. Li J., Wang Y. "Analysis of mode III delamination fracture testing using a mid-plane edge crack torsion specimen", ASTM STP 1274, 1996. 166-181.

22. Farshad M., Flueler P. "Investigation of mode III fracture toughness using an anticlastic plate bending method"'. *Engineering Fracture Mechanics*, Vpl. 60, 1998: 597-603

23. Minutes of ASTM sub-committee D30.06 on interlaminar properties., *"1st round-robin on the edge-crack torsion test"*, May, 1997.

24. Minutes of ASTM sub-committee D30.06 on interlaminar properties., *"1st round-robin on the edge-crack torsion test"*, May, 1999.

25. Ratcliffe J.G., "Characterization of the edge crack torsion (ECT) test for mode III fracture toughness measurement of laminated composite", Presented at ASTM/ASC conference, Atlanta, Oct., 2005.

26. Pennas, D., Cantwell W. J., "The Influence of Strain Rate on the Mode III Interlaminar Fracture of Composite Materials", *Journal of Composite Materials*, Vol. 41, No. 21, 2007.

27. LabVIEW., National Instruments, 2006.

28. Davidson, B.D., Perez, C.L., "Evaluation of precracking methods for the end-notched flexure test", Structures, Structural Dynamics, and Materials Conference, Newport, Rhode Island, May, 2006.

29. Baizeau, R., Davies P., Choqueuse, D., Le Bras J., "Evaluation of the integrity of the composite tubes", *Progress in Durability analysis of Composite systems* (DURACOSYS 95) Rotterdam, 1996: 231-255.

30. Hansen P., Martin R., "DCB., 4ENF, and MMB Delamination Characterization of S2/8552 and IM7/8552", *Technical Report*, N68171-98-M-5177, Materials Engineering Research Laboratory Ltd. (MERL), Hertfordshire, U.K., 1999.

31. ASTM International Subcommittee D30. Working Item: "A Protocol for Edge Crack Torsion Mode III Interlaminar Fracture Test Method", 1999: Revision C.

32. Aviles F., Carlsson L.A., Browning G.A., Millay K.R., "Investigation of the Sandwich Twist Test", *To Appear in Experimental Mechanics*, 2008.

33. Timoshenko S., Woinowksy-Krieger S., "Theory of plates and shells", McGraw-Hill, New York,1959.

34. Jones R.M., "Mechanics of Composite Materials". 2nd Edition. Taylor & Francis, Philadelphia, 1999: 208-237.

35. Tsai S.W., "Experimental Determination of the Elastic Behavior of Orthotropic Plates", *Engineering for Industry*, Aug, 1965: 315-318.

36. Li X., L.A. Carlsson, P. Davies., "Influence of fiber volume fraction on mode III interlaminar fracture toughness of glass/epoxy composites", *Composites Science and Technology*, Vol. 64, 2004: 1279-1286.

37.. Kaw, A. K., "*PROMAL" Software aid with text "Mechanics of Composite Materials"*.1997. Boca Raton: CRC Press:

38. Sih, G. C. , Liebowitz, H., "Mathematical Theories of Brittle Fracture", *Fracture. Vol. 2,* Academic Press, New York, 1968: 67 - 190.

39. ANSYS 11. Swanson Analysis Systems. Houston: 2008.

40. ABAQUS 6.5. Analysis User's Manual. 2005.

41. Ratcliffe, James. Personal correspondence. 2008.

42. Hutchinson J.W., Suo Z. Mixed Mode Cracking in Layered Materials. Academic Press, 1992.